Diss. ETH No. 20291

Impacts of large volcanic eruptions on the stratosphere and climate

A dissertation submitted to
ETH ZURICH

for the degree of
DOCTOR OF SCIENCE

presented by
FLORIAN ARFEUILLE

Dr. sc. ETH Zurich
born 16 August 1984
citizen of France

accepted on the recommendation of
Prof. Dr. Thomas Peter, examiner
Prof. Dr. Stefan Brönnimann, Dr. Eugene Rozanov, Dr. Kirstin Krüger,
co-examiners

2012

Abstract

Large volcanic eruptions may influence the Earth's climate for several years. The strong stratospheric perturbation produced by aerosols from large eruptions leads to important tropospheric anomalies. A number of observational and modeling studies have shown that large tropical eruptions produce a global cooling effect as a consequence of the volcanic aerosols which scatter a part of the incoming solar radiation back to space. However, major uncertainties remain in the representations of the magnitude and spatial distributions of the stratospheric and tropospheric perturbations in climate models. The radiative, chemical and dynamical impacts of volcanic aerosols in the stratosphere need to be closely examined in order to decrease the uncertainties on the climatic impacts of large eruptions.

This dissertation makes use of a sequence of models ranging from a 1-D model for the initial eruption plume, via a 2-D model for the detailed global stratospheric aerosol microphysics, to a 3-D coupled global chemistry-climate model (CCM). The dissertation follows 3 detailed goals: Firstly, it aims at identifying the uncertainties in the volcanic aerosol forcings used for climate model simulations, and by a systematic investigation of the Pinatubo eruption proposes new approaches to provide improved aerosol boundary conditions of this eruption for climate models. Secondly, it applies the eruption plume and global microphysics models individually to 26 volcanic eruptions between 1600 and 2011, using the latest available ice cores aerosol mass estimates and historical data on the latitude and date of eruptions, and deriving climate forcing data for these eruptions. Thirdly, the chemistry-climate model (CCM) SOCOL was used to assess the stratospheric response to the eruption of Tambora in 1816, which likely triggered the year without summer of 1816, in order to test the model and our understanding of the important impacts caused by this extreme event.

We first analyzed the uncertainties present in volcanic aerosol forcings by investigating the contribution of the aerosol external boundary conditions to the common model overestimation of the stratospheric warming following the Pinatubo 1991 eruption. This large tropical eruption is the best characterized eruption on record and is of high interest for the modelling of volcanic eruptions in general. We applied different aerosol size distributions derived from satellite observations and from a microphysical model (AER-2D). We analyzed their validity by comparing their optical properties with observations of visible and infrared extinctions. The different datasets were further tested through their impact on stratospheric temperature perturbations, as calculated with the CCM SOCOL. From our calculations, it can be concluded that using an aerosol forcing in agreement with observed post-Pinatubo extinctions in the visible and infrared leads to an overestimation of the tropical stratospheric warming in the CCM SOCOL with temperatures above 70 hPa being even higher than the already too high values found by

many models in recent general circulation model (GCM) and CCM intercomparisons. Conversely, at lower altitudes close to the tropical tropopause the temperature response could be better described by these models if they used our dataset. The present work also shows that some of the good agreements in stratospheric warming calculated in previous GCM/CCM assessments was due to a fortuitous error cancellation by using an outdated SAGE II dataset with 1 μm extinctions too low by factors 2-3. Furthermore, the use of surface area density information together with an assumption on the aerosol size distribution widths to derive extinctions in the whole wavelength spectrum, as done in previous work, does not lead to satisfactory results and should be avoided. The use of AER-2D results in too large extinctions in the equatorial region but good agreement in the extra-tropics and can provide valuable information for studies focusing on observationally inaccessible applications, such as geoengineering or eruptions before the satellite era.

In pursuing the second goal, we followed a model-based approach to develop a volcanic forcing covering the 1600-2011 period for use in climate models. The method makes use of information from state-of-the-art ice core data and involves a set of numerical models to simulate the initial volcanic plume and the subsequent chemical and aerosol microphysical processes and spreading of the plume into both hemispheres. The use of the AER-2D sulfate aerosol model to generate the forcing allows a physically consistent representation of the volcanic aerosol size and spatial distributions after the eruptions. Twenty-six eruptions were analyzed and simulated in this way, taking into account their locations, date of eruptions, and estimating the initial altitude distribution of SO_2. Comparing our results to previous reconstructions shows good agreement in the global mean 0.5 μm optical depths but large differences in the latitudinal distributions. Comparisons with observations from the Agung 1963 eruption (which exhibited a strong asymmetry in its hemispheric partitioning) and from the Pinatubo eruption give satisfactory results despite a tendency to overestimate equatorial 0.5 μm extinctions right after the eruptions. Overall, this forcing provides a credible alternative approach to reconstructions, which base the latitudinal distribution of the aerosols solely on separate estimates of northern and southern hemisphere loadings as derived from Greenland and Antarctica ice core calibrations, and which supplement this information by parametrized aerosol transport and assumptions on the size and altitude distributions of the aerosols. The use of the volcanic aerosol dataset presented here for climate simulations covering the last four centuries will help to assess the full uncertainty range in the volcanic forcing.

Third, we focused on the characteristics of the aerosol forcing and stratospheric impacts of the largest eruption in the 400 year dataset: The Tambora 1815 eruption. This eruption was likely the trigger of the "year without summer" of 1816. It constitutes an interesting case study of an extreme event which had large climatic impacts. We performed sensitivity simulations with the CCM SOCOL to assess the uncertainties in the aerosol input and in sea surface temperatures. In our model, the transport of the Tambora aerosols is predominantly made to the southern hemisphere as a consequence of the season of eruption. As a consequence, the radiative perturbation does not reach high values in the northern hemisphere extra-tropics. The aerosol size distribution exhibits large radii due to intense coagulation right after the large 60 Mt SO_2 release from the eruption. This leads to a more limited and shorter radiative impact than expected, and indeed shorter than that of a less extreme eruption such as that of Mt. Pinatubo.

The ozone is found to increase due to the slowing of the natural NO_x-induced ozone destruction cycle after the eruption compares well with studies of the Agung eruption which also erupted in a period of relatively low stratospheric chlorine concentrations. Finally, the simulations suggest a strengthening of the northern hemisphere polar vortex in the first winter after the eruption, similar to that observed for recent eruptions. The nonlinearities in the radiative, chemical and dynamical perturbations scaled by eruption sizes are further highlighted by idealized volcanic eruptions simulations, releasing between 5 and 200 Mt of sulfur dioxide.

Résumé

Les grandes éruptions volcaniques influencent le climat durant plusieurs années. La forte perturbation stratosphèrique produite pas les aérosols formés après une éruption provoque d'importantes anomalies dans la troposphère. Plusieurs études basées sur des observations ou des simulations ont montré que les importantes éruptions tropicales produisent un refroidissement global comme conséquence de la réflexion du rayonnement solaire par les aérosols volcaniques. Cependant, des incertitudes demeurent sur la représentation de la magnitude et de la distribution spatiale des perturbations stratosphèriques et troposphèriques dans les modèles. Les impacts radiatifs, chimiques, et dynamiques des aérosols volcaniques dans la stratosphère doivent être affinés pour réduire les incertitudes dans la modèlisation des impacts climatiques des grandes éruptions. Cette thèse a en premier lieu pour but d'identifier les incertitudes sur le forçage par les aérosols volcaniques utilisé dans les modèles climatiques, et de proposer de nouvelles approches pour apporter des conditions aux limites pour les modèles plus précises. Le modèle de chimie-climat (CCM) SOCOL a ensuite été utilisé pour évaluer la réponse stratosphèrique à l'importante éruption du Tambora pour tester le modèle et notre compréhension des impact importants causés par cet évènement extrême.

Nous avons dans un premier temps analysé les incertitudes présentes dans le forçage volcaniques en étudiant la contribution du forçage externe des aérosols dans la fréquente surestimation par les modèles climatiques du réchauffement stratosphèrique suivant l'éruption du Pinatubo en 1991. Cette importante éruption tropicale fut la mieux observée et est d'un grand intérêt pour la modélisation des éruptions volcaniques en général. Nous avons utilisé différentes calculations pour la distribution des tailles des àerosols, dérivées d'observations satellitaires et d'un modèle de microphysique des aérosols (AER-2D). Nous avons analysé la validité des différentes approches en comparant leurs propriétés optiques avec des observations dans le visible et l'infrarouge. Les différentes approches ont ensuite été testé à travers leurs impacts sur les températures dans la stratosphère, comme modelisé dans le modèle SOCOL. A partir de nos résultats, il a pu être conclu qu'utiliser un forçage pour le Pinatubo en accord avec les observations d'extinctions dans l'infrarouge amène à une surestimation du réchauffement de la stratosphère dans les tropiques avec le CCM SOCOL et amènerait à une augmentation du réchauffement au dessus de 70 hPa dans les CCMs utilisant des données satellitaires dépassées qui présentent des extinctions plus faibles. A l'inverse, la tropopause tropicale pourrait être mieux décrite par ces modèles s'ils utilisaient ces nouvelles données. L'utilisation des informations de densités surfaciques conjointes à un choix fixe de la largeur de la distribution en tailles des aérosols pour dériver des extinctions sur tout le spectre n'apporte pas de résultats satisfaisants et doit être évité. Le modèle AER-2D simule de trop importantes extinctions dans la région équatoriale mais a des résultats satisfaisants dans les régions extra-tropicales et peut proposer des informations de valeur pour des études mettant l'accent sur la géo-ingénierie ou

analysant des éruptions volcaniques ayant eu lieu avant la période satellitaire.

Dans un second temp, nous avons effectué une approche basée sur la modélisation pour développer un forçage volcanique sur la période 1600-2011, utilisant des informations récentes issues de forages polaires et un ensemble de modèles numériques pour simuler le nuage volcanique initial et les processus microphysiques des aérosols. L'utilisation du modèle d'aérosol AER-2D permet une représentation physiquement cohérente de la distribution spatiale et en tailles des aérosols après chaque éruption. Vingt-six eruptions ont été simulé, en prenant en compte les lieux et dates des éruptions, et l'altitude initial des émissions de SO_2. La comparaison de nos résultats avec des reconstructions précédentes montre un bon accord pour les extinctions globales à 0.5 μm mais d'importantes différences dans les distributions latitudinales. La comparaison avec des observations de l'éruption du volcan Agung en 1963 (éruption ayant montré une très grande disymmetrie dans la répartition des ses aérosols entre les deux hémisphères) ainsi que du mont Pinatubo ont montré un bon accord malgré la tendance à la surestimation des extinctions au niveau de l'équateur immédiatement après les éruptions. De manière générale, ce forçage propose une alternative crédible aux reconstructions basées sur les informations des forages polaires pour estimer la répartiton des aérosols dans chaque hémsiphère séparèment. Ces reconstructions utilisent aussi un transport paramètrisé et des hypothèses sur les distribution spatiales et en tailles des aérosols. L'utilisation de ces nouvelles données d'aérosols volcaniques dans des simulations climatiques couvrant les quatre derniers siècles pourrait aider à mieux évaluer les incertitudes sur le forçage volcanique.

Finalement, nous avons étudié les propriétés optiques et les impacts stratosphèriques de la plus importante éruption présente dans la reconstruction 1600-present: L'éruption du Tambora en 1815. Cette éruption a probablement provoqué "l'année sans été" de 1816 et constitue un cas intéressant pour l'étude des impacts des éruptions volcaniques. Nous avons effectué différentes simulations pour juger du rôle des incertitudes dans les données sur les aérosols et dans les températures de surface des océans. Dans notre modèle, le transport des aérosols du Tambora se fait en majorité dans l'hémisphère sud du fait de la saison de l'éruption. Les perturbations radiatives restent ainsi relativement faibles dans les moyennes latitudes de l'hémisphère nord. Les aérosols ont de larges diamètres du fait de l'importante coagulation juste après l'émission des 60 Mt de SO_2. Cela cause un impact radiatif plus limité et plus court qu'attendu. L'augmentation de l'ozone simulé après l'éruption est similaire aux résultats d'études pour l'éruption du volcan Agung qui a aussi eu lieu lors d'une période de faible concentration stratosphèriques de chlorine. Finalement, une intensification du vortex polaire dans l'hémisphère nord durant le premier hiver après l'éruption est simulée dans notre modèle, comme observé pour des éruptions plus récentes. Les non-linéarités des perturbations radiative, chimique, et dynamique relativement à différentes tailles d'éruption sont soulignées plus en détails par l'analyse de simulations d'éruptions idéalisées, rejettant entre 5 et 200 Mt de dioxide de soufre.

Contents

Chapter 1

Introduction

1.1 Background

The influence of volcanic eruptions on climate has been known for more than two centuries. In 1784, Benjamin Franklin was one of the first to mention the link between volcanic eruptions and unusual weather by noticing the shading effect of the Laki eruption 'fog' on sunrays (*Franklin*, 1784). But this mainly tropospheric (*Highwood and Stevenson*, 2003) Icelandic eruption was certainly easier to connect to abnormal weather than was the Mt.Tambora (Indonesia) eruption of April 1815. To our knowledge no contemporary documents linked the eruption to the extreme cold which notably hit Europe and North America in the summer 1816 (*Oppenheimer*, 2003), even though the cataclysmic eruption which killed around 10,000 people was known from direct reports from Java by Sir Thomas Raffles. It is only from the early 20^{th} century that meteorological reports linking the Tambora eruption to the uncommon following weather were published (*Milham*, 1924). The scientific research carried out to understand the detailed connections between volcanic eruptions and climate developed in the 1970s and 1980s with studies on the climatic effects of nuclear weapons and global impacts of volcanic eruptions (*Lamb*, 1970; *Turco et al.*, 1982). That period, marked by two large eruptions (Agung 1963, El Chichón 1982) and concerns about the consequences of a nuclear winter, favored the research on the radiative effects of stratospheric aerosols. Today, in a context of a warming climate, the study of volcanic eruption impacts on climate is again a matter of concern. Understanding how and by how much past eruptions influenced climate helps to separate and evaluate the different natural and anthropogenic forcings in observations as well as in climate models. Increasing the comprehension of theses changes is crucial in the attempt of making accurate climatic previsions. Moreover, large stratospheric volcanic eruptions are natural experiments and are the inspiration for the solar radiation management (SRM) geoengineering possibility to offset current global warming (*Crutzen*, 2006). Other current motivations include a need to be prepared for the next large eruption and the study of climatic impacts of a regional nuclear war (*Toon et al.*, 2007; *Robock*, 2010). With these new challenges, many new techniques are used to explore the climate impacts of volcanic eruptions. However, important uncertainties remain in both observations and models and need to be identified and reduced.

1.2 Volcanic stratospheric aerosols

Large volcanic eruptions release various compounds in the troposphere and stratosphere. Volcanic ash, consisting in pulverised or finely fragmented magmatic material, is particularly relevant for aviation hazard studies but the time residence in the atmosphere of these particles, with diameters in the range of 10 μm to a few millimeters, is short and their climatic effects can in general be neglected. Volatiles constitute the greatest volume of material erupted by volcanoes, with water vapor, CO_2 and sulfur being the main gases expelled from volcanic eruptions. The sulfur is found in the S_2, SO, SO_2, SO_3, H_2S, H_2SO_4, COS, and CS_2 forms in volcanic plumes (*Heald et al.*, 1963), SO_2 being by far the most common. After strong Plinian volcanic eruptions, large amounts of SO_2 reach the stratosphere and react with OH to build HSO_3:

$$SO_2 + OH + M \overset{k_{SO_2+OH}}{\longrightarrow} HSO_3 + M. \tag{1.1}$$

Further on, HSO_3 reacts with O_2 (*Calvert and Stockwell*, 1983):

$$HSO_3 + O_2 \overset{k_{HSO_3+O_2}}{\longrightarrow} SO_3 + HO_2. \tag{1.2}$$

Then sulfuric acid forms as SO_3 reacts with water vapor:

$$SO_3 + 2H_2O \overset{k_{SO_3+H_2O}}{\longrightarrow} H_2SO_4 + H_2O. \tag{1.3}$$

In the following, we briefly outline the processes following a major volcanic eruption (adapted from the PhD work of Patricia Heckendorn (*Kenzelmann*, 2009)). After the production of large amounts of volcanic H_2SO_4 in the lower stratosphere, preexisting sulfate aerosols have a lower H_2SO_4 vapor pressure than the H_2SO_4 partial pressure, hence H_2SO_4 tends to condensate onto pre-existing aerosols, preferring the largest aerosol droplets (because of the Kelvin effect). However, under conditions of extreme H_2SO_4 concentrations in a fresh volcanic plume, besides condensation homogeneous and heterogeneous nucleation leading to new aerosol formation can occur (*Turco et al.*, 1982). Furtermore, temperature and pressure influence the water vapor pressure of the aqueous H_2SO_4 droplets and hence their equilibrium concentration. When the ambient temperature drops the water vapor pressure decreases and more water is taken up from the aerosol and the H_2SO_4 weight percent (wt%) decreases. Therefore the cold regions of the stratosphere, namely the winter poles and the tropical tropopause, show low sulfate weight fraction (40-50 %) in contrast to the rest of the stratosphere which shows values between 70 and 80 % (e.g. *Hoffman and Rosen*, 1983; *Steele and Hamill*, 1983). During volcanically quiescent background conditions the aerosol distribution can be described as approximately lognormal with a mode radius between 0.05–0.07 μm (*Steele and Hamill*, 1983). After volcanic eruptions additionally to the small mode of $\sim$0.07 μm one or two larger modes are observed (*Deshler et al.*, 1992; *Thomason*, 1992) (Figure 1.1).

To correctly depict the aerosol radiative, chemical and dynamical influences their microphysical behavior have to be described with sufficient accuracy. This concerns predominantly their size distribution, which is required to calculate the radiative influence of volcanic aerosols. Essential microphysical processes are nucleation, condensation, coagulation and sedimentation. The nucleation of sulfate aerosols is thought to be mostly a binary homogeneous process (*SPARC*, 2006), although there is evidence for the presence of heterogeneous nucleation of stratospheric particles in the polar regions,

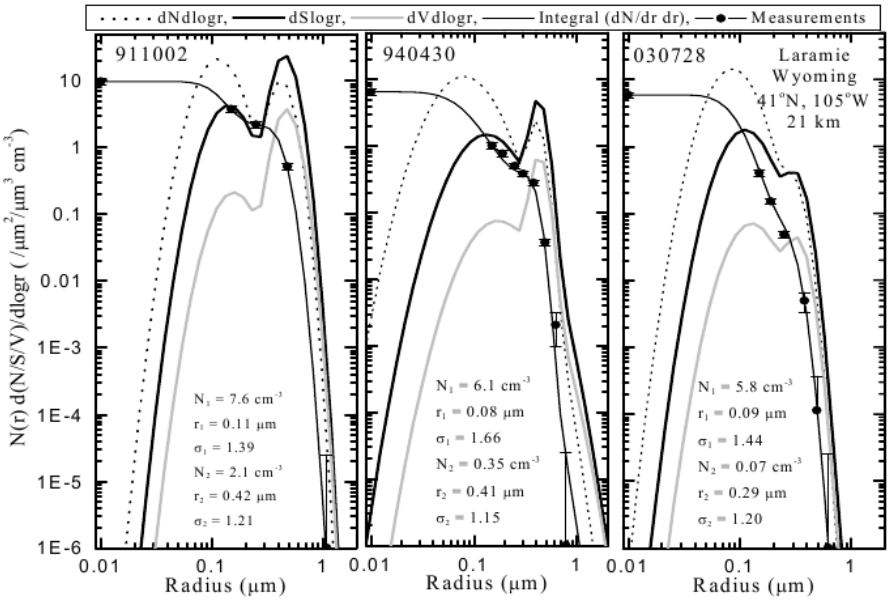

Fig. 1.1: Differential number (cm^{-3}), surface area (μm^2 cm^{-3}), and volume ((μm^3 cm^{-3}) distributions, as a function of dlog10(r) derived from fitting bimodal lognormal size distributions to in situ optical particle counter measurements above Laramie, Wyoming. The measurements are shown as data points with Poisson error bars. The solid lines passing near the data points are the cumulative number distributions obtained from integrating the size distributions fit to the data. The measurements are all 1.0 km averages centered on 21 km, and are representative of mid stratospheric aerosol for cases of large volcanic loading (5 October 1991 - 911005), moderate loading (30 April 1994 - 940430) and background (28 July 2003 - 030728). From SPARC's stratospheric aerosol assessment ASAP (SPARC, 2006).

most likely on meteoritic material (*Curtius et al.*, 2005). After a volcanic eruption, tiny H_2SO_4/H_2O particles nucleate in the injection plume which will then coagulate to form the bimodal aerosol size distribution, see Figure 1.1. The radius of volcanic aerosols in the nucleation mode is almost two orders of magnitude smaller than the radius of background aerosols. Another important process is the coagulation, where the brownian motion of the aerosols leads to collision and subsequently aggregation of the particles.

The transport of the stratospheric aerosols depends on their sedimentation speed and on the stratospheric circulation. The so-called Brewer-Dobson circulation comprises an ascending air motion in the tropics and subsidence over the extratropical regions. The overturning time of the Brewer Dobson circulation is approximately five years (*Rosenlof*, 1995). The Brewer-Dobson circulation is controlled by wave-driven forces in the mid-latitudes, which in turn are generated through the differential heating of the earth's surface, the topography and the synoptic weather patterns. These waves then propagate into the stratosphere and subsequently break and dissipate, producing a poleward transport which then generates upwelling in the tropics and downwelling at the poles. The poleward transport is preferentially generated in the winter hemisphere (*Charney and Drazin*, 1961). Along the transport to high latitudes, aerosols in the higher branch can evaporate. H_2SO_4 in the gas phase is totally negligible below 30 km but close to 100 % around 40 km. In the lower branch large particles will be removed

through tropopause folds and only a small part (ca. 25 %) of the aerosols reaches the polar region. The part of the sulfate deposited in Greenland and Antarctica can then provide useful information on past volcanic eruptions through ice cores studies. The main microphysical processes and transport patterns of the stratospheric aerosols are summarized in Figure 1.2 (*Hamill et al.*, 1997). Large volcanic eruptions diretly release SO_2 in the stratosphere, usually around 20-25 km.

Stratospheric aerosol particles from volcanic eruptions produce large perturbations in the radiative budget as they absorb infrared radiation and scatter UV and visible irradiance. The scattering and absorption strongly depend on the size of the particle and the wavelength of the incoming radiation. According to the Mie theory (*Mie*, 1908) the physical relationship between both can be expressed by α a dimensionless size parameter:

$$\alpha = \frac{2\pi r}{\lambda}. \tag{1.4}$$

The extinction is defined as the sum of scattering and absorption. It is often characterised by the extinction coefficient:

$$k(\lambda) = \int_0^{r_{max}} \frac{2\pi r^2}{4} Q_E(R, \alpha) N(r) dr, \tag{1.5}$$

where r_{max} is the upper limit of the radius of the particle population with the number size distribution $N(r)$ as a function of radius r. The extinction efficiency $Q_E(R, \alpha)$ is a function of the refractive index R and the size parameter α. The refractive index $R(\lambda)$ can be described by a wavelength dependent complex function:

$$R(\lambda) = n(\lambda) + \mathrm{i}a(\lambda), \tag{1.6}$$

where $n(\lambda)$ defines the refraction and the scattering of light passing through a medium and $a(\lambda)$ defines the absorption. The refractive index of the aerosol depends on the weight fraction of condensed H_2SO_4 in the aerosol and on temperature (*Biermann et al.*, 2000). A direct chemical perturbation generated by stratospheric aerosols is through the occurence of heterogeneous reactions on their surfaces. Moreover, stratospheric aerosols act as precursors for polar stratospheric cloud (PCS) formation. The direct radiative and chemical influences of the aerosols modify subsequently the stratospheric dynamics, one example being the strengthening of the polar vortex observed in the first winter after large eruptions (*Stenchikov et al.*, 2006).

1.3 Outstanding issues

A number of issues remain in the representation of the volcanic eruption aerosol forcing and its atmopheric response in climate models:

- Limitations in the observational data of the Pinatubo eruption lead to substantial uncertainties in the aerosol properties. One major issue is the region of missing data due to optical saturation of satellite measurements after the eruption (black regions in Figure 1.3).

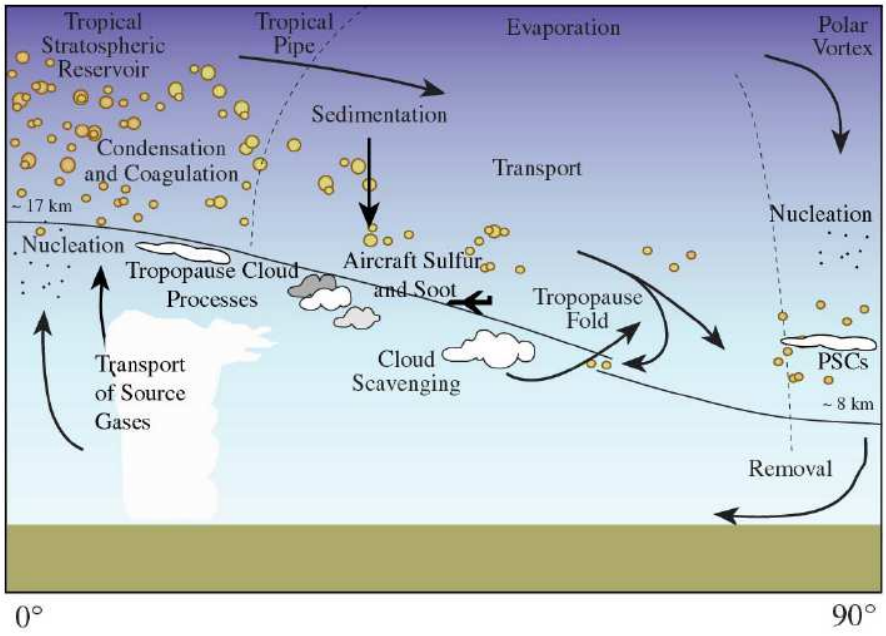

Fig. 1.2: Schematic of the stratospheric aerosol life cycle [from *Hamill et al.* (1997)].

- The representation of the response to the Pinatubo eruption in chemistry-climate models (CCM) and general circulation models (GCM) shows large uncertainties, especially in the stratospheric warming perturbation, and models commonly overestimate the temperature increase after the eruption (*Eyring et al.*, 2010; *Gettelman et al.*, 2010; *Lanzante and Free*, 2007). Figure 1.4 shows for instance that CCMs which take into account the absorption effect of the aerosols tend to overestimate the warming in the lower stratosphere. Is the overestimation of the stratospheric warming following the Pinatubo eruption linked to model deficiencies or uncertainties in the aerosol boundary conditions?

- Even larger uncertainties exist in the volcanic forcing before the satellite period (*Forster et al.*, 2007). This limits the ability to simulate historical eruptions and consequently increases the uncertainties in climate simulations covering the last centuries. One source of uncertainty is the lack of knowledge on the size and spatial distributions of the aerosol from historical eruptions before the satellite era.

- There are strong nonlinearities in both aerosol optical properties and stratospheric responses with respect to eruption sizes which need to be better understood and accounted for when modelling large eruptions. What radiative, dynamical and chemical stratospheric perturbations can we expect from eruptions larger than Pinatubo?

1.4 Methods

To address the important issue of the excessive stratospheric heating following volcanic eruptions in climate models, we used the state-of-the-art SAGE II gap-filled dataset for the Pinatubo eruption as compiled in *SPARC* (2006). SAGE

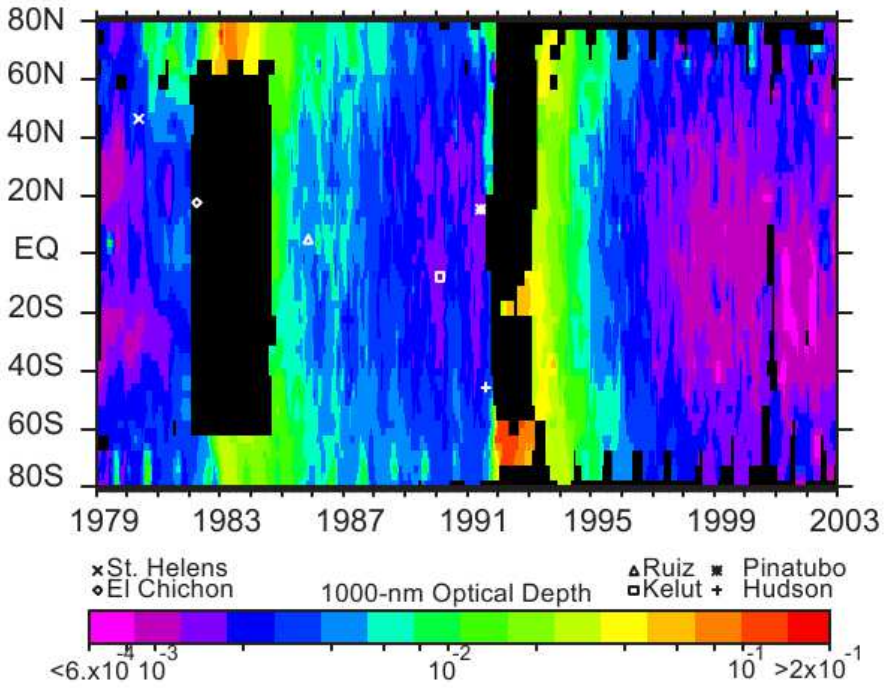

Fig. 1.3: SAM II, SAGE, and SAGE II stratospheric aerosol optical depth at 1000 nm from 1979 through 2002. Profiles that do not extend to the tropopause are excluded from the analysis leading to a significant region of missing data following the eruption of Mt. Pinatubo in 1991. The earlier gap (1982-1984) was the period between SAGE and SAGE II. From SPARC's stratospheric aerosol assessment ASAP (SPARC, 2006).

II provides extinction measurements at the 385, 453, 525 and 1020 nm wavelengths for the Pinatubo eruption. From this, we derived aerosol size distributions in order to calculate extinctions in the full spectral range, as the infrared extinction measurements available are too sparse to directly produce a comprehensive dataset for the eruption. The goal is to generate aerosol size distributions exhibiting extinctions, in both visible and infrared wavelengths, close to available measurements and identify where the uncertainties remain at each step of the calculation from extinction observations to climate modeling. These aerosol data are then used to generate extinctions, asymmetry factors and single scattering albedos required to simulate the eruption with the CCM SOCOLv2 (*Schraner et al.*, 2008) in order to assess the stratospheric responses to the generated forcings and make comparisons to observations and previous modelling studies (see Section 4.3.2 for a description of the SOCOL model).

As alternative second method to generate the required size distributions, we used the two-dimensional aerosol model AER-2D (*Weisenstein et al.*, 1997). We then test the accuracy of the 2-D aerosol model in describing the different optical features of the Pinatubo aerosols (see Section 4.3.1 for a description of the AER model). The use of this model allows to simulate volcanic eruptions during periods with insufficient observations. It allows to build a consistent dataset, which is subsequently applied to simulate the largest volcanic eruptions of the last 400 years.

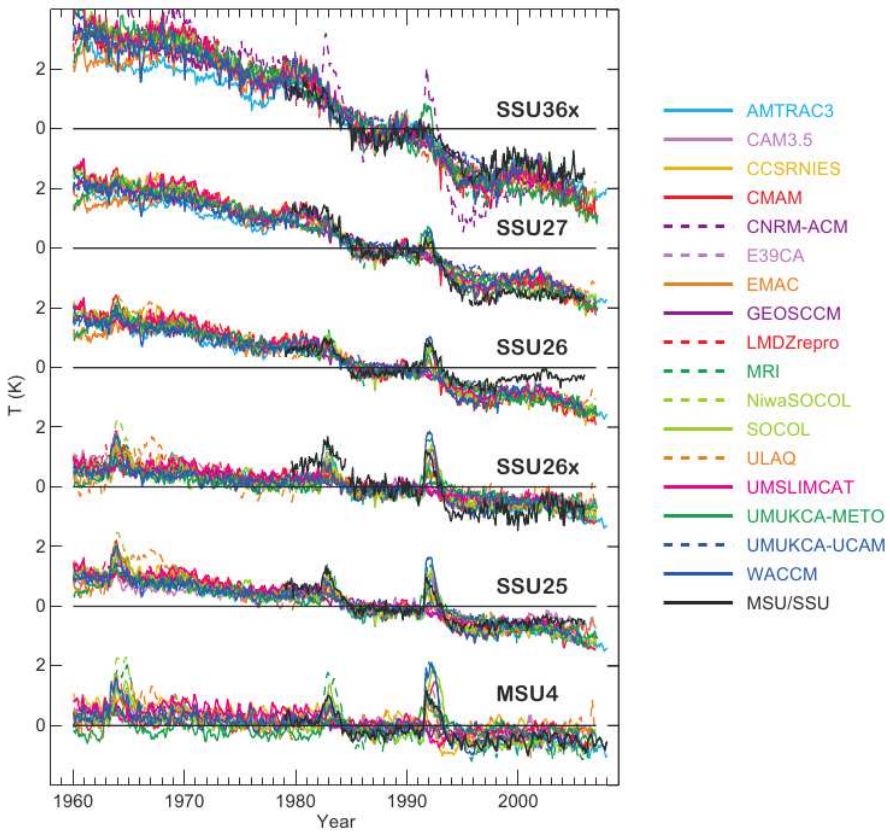

Fig. 1.4: Near global mean time series (70°S-70°N) of MSU/SSU satellite observations and REF-B1 model temperature data weighted by MSU/SSU weighting functions. MSU/SSU channels include: MSU-4 (at 70 hPa), SSU25 (15 hPa), SSU26 (5 hPa), SSU27 (2 hPa), SSU26x (15 hPa) and SSU36x (1 hPa), where the specified pressure levels represent the approximate weighted mean heights derived from the MSU/SSU vertical weighting functions for each channel (see Randel et al., 2009), negative portions of the weighting functions excluded.For each model only the first ensemble member from the REF-B1 simulations is shown. The anomalies are calculated with respect to the period 1980-1994, as in the provided SSU anomalies. Note that UMETRAC is not included in this figure. CNRM-ACM is only shown in the highest SSU36x level due to its too strong sensitivity to volcanoes. UMUKCA-UCAM in not shown after year 2000. Low top models CAM3.5 and E39CA (the lids are at 3 hPa and 10 hPa respectively) are shown only in the MSU4, SSU25 and SSU26x panels. From the SPARC CCMval report (SPARC, 2010).

The dataset is compared to existing reconstructions and observations for the more recent period. One main advantage of this method is the full description of size and spatial distributions of the volcanic aerosols following each eruption. Additionally to information on date and location of eruptions which allow AER-2D to compute hemispheric asymmetries in the global distribution of the volcanic material, we used the one-dimensional volcanic plume model Plumeria (*Mastin*, 2007) to infer the initial altitude distribution of the SO_2 cloud when sufficient information is available. The neutral buoyancy height, where ultimately the volcanic SO_2 settles, is taken as the altitude where the plume density, taking account of moisture and ash, equals the atmospheric density in the model. The Plumeria model performs reasonably well when compared with most plume height measurements although

uncertainties are present, arising from errors in the estimations of injection rates and plume dynamics under actual meteorological conditions (*Mastin et al.*, 2009).

Finally, the generated volcanic forcing is used to simulate with the CCM SOCOL the largest volcanic eruption in the 1600-2011 period: The Tambora eruption of April 1815. The strong stratospheric perturbation caused by the Tambora aerosols provides an interesting test of our approach, and the analysis of the main radiative, chemical and dynamical impacts for this size of eruption helps identifying relevant mechanisms, such as the rate of coagulation of the H2SO4/H2O droplets generated in the high particle number density clouds and the resulting stratospheric lifetime of the volcanic material.

1.5 Thesis outline

In **Chapter 2**, the CCM SOCOL is used in combination with satellite data or in combination with the AER-2D aerosol model to analyze the eruption of Mt. Pinatubo in June 1991. This large tropical eruption is the best observed eruption with strong climate impact on record, allowing to examine the accuracy of the calculated aerosol datasets. To analyze the uncertainties of the CCM SOCOL in simulating the response to the Pinatubo eruption, we computed an external volcanic forcing based on satellite data, matching the optical characteristics of the Pinatubo aerosols as closely as possible. Alternatively, we performed Pinatubo climate simulations with stratospheric aerosol distributions derived from AER-2D in order to analyze the uncertainties involved in the AER-2D model computations. The CCM SOCOL was then used to analyze the Pinatubo stratospheric warming produced by these volcanic datasets.

The AER-2D model can be used to perform simulations of geoengineering scenarios or to model historical volcanic eruptions, when no data on the size-resolved space-time distribution of aerosols are available. Indeed, reliable satellite data to gain information on volcanic aerosols are only available since 1979. Before that, information on aerosols are available from limited solar extinction data for the 1883-1978 period. Before 1883, no direct precise extinction data is available and sources of information are then taken from ice cores for aerosol total loading, from historical reports for the identification of the volcanoes, and from petrological data. Knowledge on the size, altitude and latitude distribution of the aerosols with time cannot be precisely infered from these limited information without making assumptions on their scaling compared to the few recent observed eruptions. The use of an aerosols microphysical model is then of interest to test the validity of these assumptions and propose an alternative way to reconstruct historical eruptions. In that respect, simulations of past eruptions in the 1600-2011 period were made with the AER-2D model and results are shown in **Chapter 3** and compared to previous reconstructions (*Sato et al.*, 1993; *Ammann et al.*, 2003; *Crowley et al.*, 2008). The dependance of the resulting climate forcing on the seasonality, location and size of the eruptions is also examined.

The aerosol size distribution is a crucial information in order to determine

aerosol climatic impacts. One important question is the influence of the different amounts of SO_2 mass released on the sizes of the aerosols and finally on the resulting climate forcing. In **Chapter 4**, the AER-2D model results for the Tambora 1815 eruption are presented. We simulated the Tambora stratospheric response with the CCM SOCOL accounting for the specific characteristics of this eruption, with SO_2 injections in the 60-80 Mt range (3-5 times the Pinatubo release) in April 1815, low sea surface temperatures and pre-industrial levels of greenhouse gases and ozone depleting substances. To better apprehend how the changes in aerosol loadings impact the characteristics of the aerosols and the stratospheric perturbations, idealized volcanic simulations were also made injecting 5, 10, 20, 60 and 200 Mt of SO_2.

Finally in **Chapter 5** I summarize the main results and present suggestions on relevant future work.

Chapter 2

Uncertainties in modelling the stratospheric warming following Mt. Pinatubo eruption

F. Arfeuille[1], P. Heckendorn[1], D. Weisenstein[2], B.P. Luo[1], J. Sheng[1], E. Rozanov[1,3], M. Schraner[4], S. Brönnimann[5], L.W. Thomason[6], and T. Peter[1]

[1] Institute for Atmospheric and Climate Science ETH Zurich, Zurich, Switzerland
[2] AER, Lexington, Massachusetts, USA. (Now at Harvard University, Cambridge, MA, USA)
[3] Physical-Meteorological Observatory/World Radiation Center, Davos, Switzerland
[4] Federal office of Meteorology and Climatology Meteoswiss , Zurich, Switzerland
[5] Oeschger Center for Climate Change research and Institute of Geography, University of Bern, Bern, Switzerland
[6] NASA Langley Research Center, Hampton, Virginia, USA

In preparation for publication in Geophys. Res. Lett.

Abstract
In terms of atmospheric impact, the volcanic eruption of Mt. Pinatubo (1991) is the best characterized large eruption on record. It serves for testing and improving the modeling of the climate response to volcanic eruptions. However, the lack of measurements in the tropics during the first months after this eruption due to opacity saturation of satellite occultation measurements complicates the reconstruction of stratospheric aerosol size distributions as a prerequisite for global climate modeling. We investigate here the stratospheric warming following the Pinatubo eruption derived from SAGE II extinction data available from SPARC [2006], including most recent improvements in the processing algorithm and a data filling procedure in the opacity-induced "gap" regions. From these data, which cover wavelengths of 1 μm and shorter, we derived aerosol size distributions, which properly reproduce extinctions at much larger wavelengths, e.g. at 12 μm as measured by ISAMS, providing a good basis for calculating the absorption of terrestrial infrared (IR) radiation and the resulting stratospheric heating. However, we also show that the use of this dataset in the global chemistry-climate model (CCM) SOCOL leads to exaggerated aerosol-induced stratospheric heating, even larger than the already too high values found by many models in recent general circulation model (GCM) and CCM intercomparisons. This suggests that the overestimation of the stratospheric warming after the Pinatubo eruption arise from model deficiencies rather than an insufficient observational data basis. Conversely, our approach reduces the IR absorption in the tropical tropopause region, in better agreement with the post-volcanic temperature record at these altitudes.

2.1 Introduction

The most recent large tropical volcanic eruption was that of Mt. Pinatubo in June 1991 in the Philippines (15°N). Unlike earlier major volcanic eruptions of the 20^{th} century, Mt. Pinatubo has been relatively well characterised by observations. Several satellite, balloon-borne and ground-based measurements are available during this period (*Bluth et al.*, 1992; *Labitzke and McCormick*, 1992; *McCormick*, 1992; *Stowe et al.*, 1992; *Thomason*, 1992; *Minnis et al.*, 1993; *Antuña et al.*, 2002). However, the peak of the stratospheric aerosol cloud is not well characterized as the observational network was best established in the northern hemisphere and less dense in the tropics and southern hemisphere, where a large part of the emitted SO_2 and resulting sulfate aerosols was transported. An additional problem was that for some instruments measuring in the shortwave, the lower stratosphere became opaque. For instance during the first year after the Pinatubo eruption SAGE II measured only above about 23 km altitude at wavelengths of 1 μm and shorter. To cope with the regions of missing data, *SPARC* (2006) provides a "gap-filled" data set spanning the period 1979-2004 using SAGE data amended by measurements from lidar ground stations. This SAGE II gap-filled dataset provides the most complete and accurate global optical characterization of the eruption, even if the quality of this dataset in the most perturbed periods is limited, in particular in the tropics with uncertainties in the order of 50 % in the extinctions.

There are several earlier attempts to create a consistent global stratospheric aerosol

dataset of the Pinatubo eruption (eg. (*Sato et al.*, 1993; *Stenchikov et al.*, 1998)) for climate models. The *Stenchikov et al.* (1998) dataset provides spectral extinctions and directly calculated heating rates for modeling studies, while the *Sato et al.* (1993) "GISS" dataset consists of optical depth data for 0.5 μm wavelength and effective radii in four different altitude ranges and 24 latitude bands derived from SAGE II data. However, these two datasets use outdated versions of the SAGE retrieval algorithm and gap-filling and no systematic comparison with ISAMS 12.1 μm measurements was performed to verify the applicability for extinctions in the terrestrial IR, which is a requirement for climate simulations. These are indeed important points to investigate because major stratospheric volcanic eruptions in the tropics represent an important external forcing to the climate system and many uncertainties remain in their modeling by CCMs/GCMs. Simulations exhibit a large range of responses due to model deficiencies and/or uncertainties in the volcanic forcing. Many GCMs/CCMs overestimate the stratospheric warming after volcanic eruptions and an attribution of this artifact remains difficult because of the large range of optical forcings obtained with different approaches and datasets (*Eyring et al.*, 2010; *Gettelman et al.*, 2010; *Lanzante and Free*, 2007)).

2.2 Methods

The most elaborated gap-filled SAGE II 1020 nm extinction record is described by *SPARC* (2006) (hereafter called SAGE_ASAP). The gaps in the SAGE II measurements, mainly caused by complete opaqueness directly after the Pinatubo eruption, were filled by means of lidar measurements at Mauna Loa in Hawaii, at Camagüey in Cuba, at Hampton, Virginia (USA) and with backscatter sonde measurements from Lauder, New Zealand. The lidar measurements have been converted to 1020 nm (SAGE II wavelength) (*Antuna et al.*, 2003). Mauna Loa (19.54°N) and Camagüey (21.4°N) were frequently below the main aerosol cloud and these values are taken for the tropical region. However, due to the fact that the main aerosol cloud was not always located above the two lidar stations, an erroneous seasonality of the aerosol amount might be present in the compiled dataset (*SPARC*, 2006).

To retrieve extinctions in the whole spectral range and subsequently model the stratospheric warming response, the particle size distribution has to be known. During quiescent times the size distribution of stratospheric aerosol is well captured by a simple unimodal lognormal distribution (*Wurl et al.*, 2010). However, after volcanic eruptions a second and third mode are observed, consequently a bimodal (or trimodal) lognormal distribution fits the data better (*Deshler et al.*, 1992). For simplicity and because of patchiness of the data many studies nevertheless use unimodal lognormal distributions (e.g. *Kinnison et al.*, 1994; *Russell et al.*, 1996; *Stenchikov et al.*, 1998; *SPARC*, 2006).

In this study we compare four methods to retrieve spectrally resolved optical properties: first, a method with varying effective radii and distribution widths (called SAGE_4λ hereafter) to find the best fit to the four wavelengths of SAGE_ASAP extinction measurements; second, the method by *Stenchikov et al.* (1998) (called ST98 hereafter) using an older version of the SAGE II data set; third, a method using an aerosol model (AER-2D, *Weisenstein et al.* (1997)), where the aerosol size

distributions depend directly on microphysical processes and boundary conditions such as SO_2 injection mass and location of injection (7 MT of sulfur injected at 23-25 km in a simulation called AER_7 hereafter); and fourth, the approach described by *Schraner et al.* (2008), using SAGE_ASAP and deriving the surface area densities and effective radii based on a principal component analysis using four wavelengths of SAGE II (*Thomason et al.*, 1997b) and assuming a fixed distribution width (σ). *Schraner et al.* (2008) prescribed σ to 1.8 (named SAGE_1.8 below), which is a mean value for the last few decades. However, after volcanic eruptions σ can differ substantially from this value. In this study we repeated the calculation for σ equal to 1.2 (SAGE_1.2), which is close to the value for the large particle mode after volcanic eruptions and close to the assumption made by ST98.

Measurements for the sulfur amount injected into the stratosphere are subject to uncertainties. Total uncertainty in the amounts range from 7 to up to 13 Mt S (*Lambert et al.*, 1993; *Guo et al.*, 2004; *SPARC*, 2006), hence a sensitivity run was performed with AER-2D injecting 9 MT of SO_2 (AER_9). The simulation made for the SPARC ASAP report with 10 MT of SO_2 injected in a broader altitude range (16-29 km), absence of tropospheric washout of aerosols above 10 km (instead of 16 km), and climatological wind fields is also shown (AER_10_ASAP).
The different methods are further described in the supplementary material.

Finally, the results from SAGE_4λ and AER_7 are used as input for the CCM SOCOL.v2 (*Schraner et al.*, 2008) to test the radiative response to these optical forcings.

2.3 Results

The extinction, single scattering albedo and asymmetry factor at wavelengths covering the whole spectral range are the key parameters to model the radiative impact of stratospheric aerosols. These quantities are calculated by means of Mie theory (*Mie*, 1908) for spherical dielectric aerosol particles, using refractive indices measured by *Biermann et al.* (2000) and satellite temperature data to infer the aerosol H_2SO_4 concentration applied to the retrieved size distributions.

Size distributions. Figure 2.1 shows size distributions derived from SAGE_4λ and from the AER-2D model runs for a 7 MT eruption (AER_7) and volcanically quiescent conditions (Background), in comparison with optical particle counter (OPC) measurements from Laramie, Wyoming (*Rosen*, 1964; *Deshler et al.*, 1992). The AER-derived size distributions at the equator in August 1991 (Figure 2.1a) show the development of the volcanic mode and a shift of the background mode to larger radii. SAGE_4λ suggests a wide unimodal distribution (width of 1.80). This is because the SAGE_4λ minimizes the differences to the four wavelenghts of SAGE_ASAP which exhibits a high 0.5 μm to 1 μm extinction ratio in the lower stratosphere right after the eruption. This results in high particle number densities as a consequence of slow coagulation due to a limited diffusion coefficient of aerosol particles (high pressure, low temperature). See Figure 2.5 of supplementary material.

Figure 2.1b shows a comparison with OPC measurements from Laramie (41°N) at 64 hPa for January 1992. The SAGE_4λ approach covers the two modes of the observed

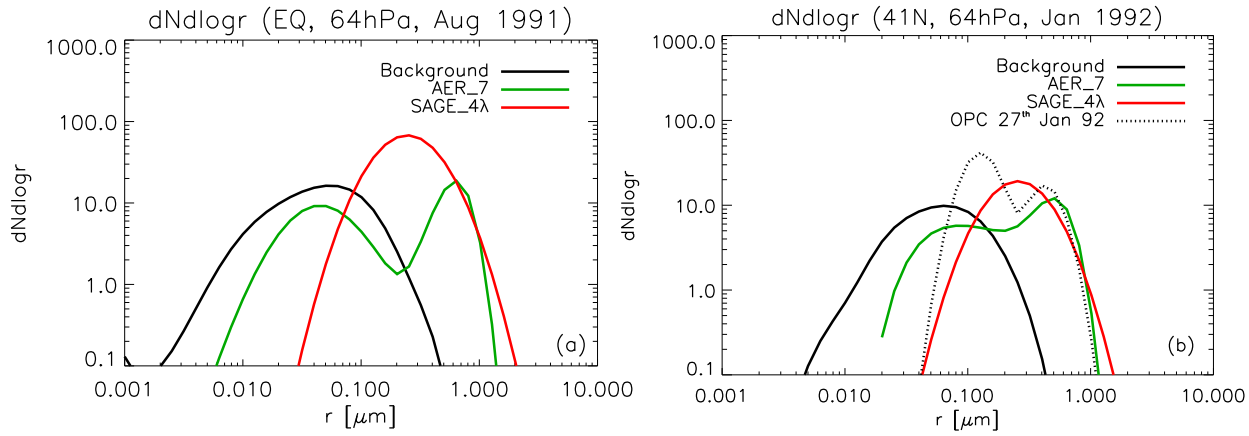

Fig. 2.1: Differential number density $dN/d\log r$ as a function of aerosol radius at 64 hPa for (a) the equator (5°S–5°N) in August 1991, and (b) northern mid-latitudes (40°N) in Jan 1992. Dashed black line in (b) shows the OPC measurements at Laramie, Wyoming (41°N).

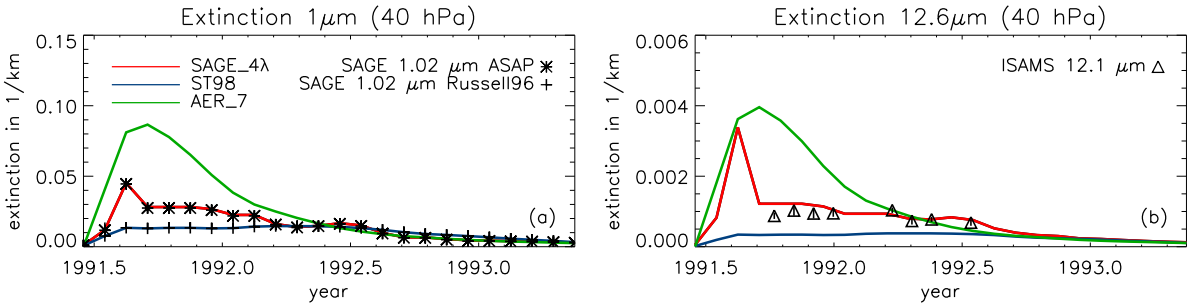

Fig. 2.2: Zonally averaged extinction from June 1991 to June 1993 for 1 μm and 12.6 μm at the equator (5°S–5°N) at 40 hPa. Vertical lines show the standard deviations of the measurements when available. SAGE_ASAP standard deviations are inferior to the symbol size

distribution, but exhibits fewer aerosols below 0.35 μm. The AER_7 simulation captures well the high end of the distribution but underestimates the radius of the aerosols in the background mode, possibly due to a too rapid latitudinal distribution in the 2D model.

From these size distributions, extinctions are computed for short and long wavelengths and compared to measurements from SAGE II at 1 μm and ISAMS at 12.1 μm, see Figures 2.2 and 2.3.

Shortwave extinctions. SAGE_4λ shows perfect agreement with SAGE_ASAP at 1020 nm as shown in Figure 2.3a and 2.2a at the equator. This illustrates the accuracy of SAGE_4λ in matching the various wavelengths of SAGE_ASAP by adjusting the number density and distribution width of the aerosols. ST98, with retrieval based on old data (*Russell et al.*, 1996), is less than half of SAGE_ASAP 1 μm measurements at 40hPa in 1991. Above 27 km and below 20 km at the equator, ST98 overestimates SAGE_ASAP data. Accordingly, heating rates calculations in GCMs and CCMs based on ST98 use a data set that significantly underestimates the 1 μm extinction in the tropical stratosphere in the 20-23 km range and overestimates it below.

The AER simulations significantly overestimate the extinction at the equator when

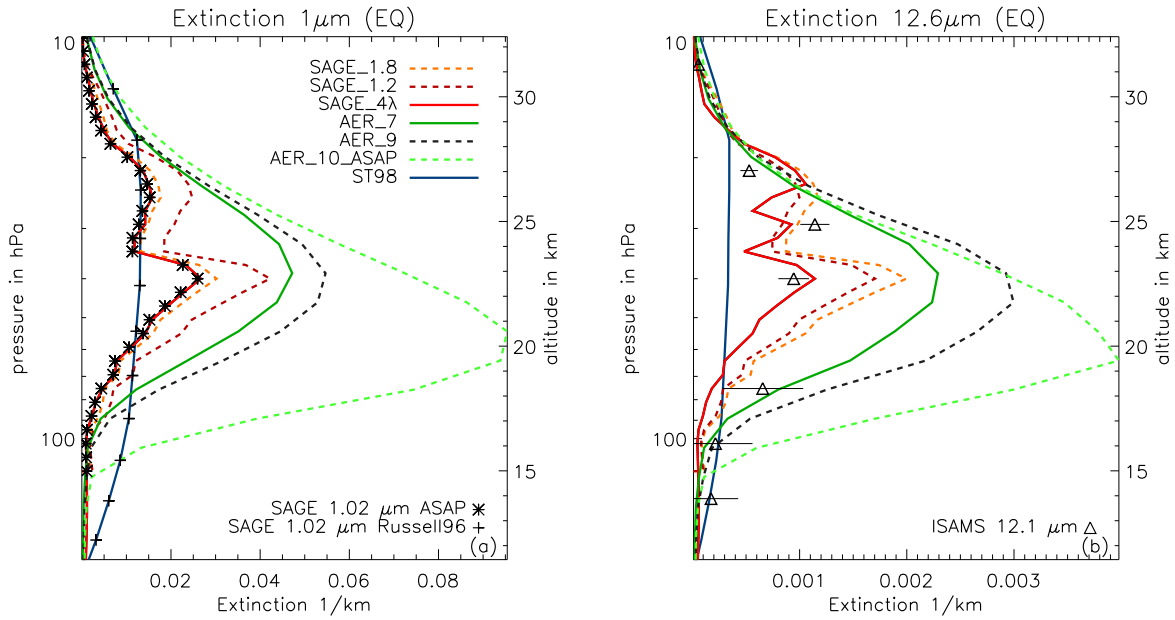

Fig. 2.3: Zonally averaged extinction profiles in December 1991 at 1 μm and 12.6 μm at the equator (5°S-5°N). Horizontal lines show the standard deviations of the measurements when available. SAGE_ASAP standard deviations are inferior to the symbol size.

compared to SAGE_ASAP. However, in the extra-tropics, AER_7 results are generally in very good agreement with the observations (see Figure 2.6 of supplementary material).

The profiles of Figure 2.3a show that SAGE_1.8 and especially SAGE_1.2 overestimate the 1 μm extinctions at all altitudes.

Longwave extinctions. The 12.1 μm extinction provides information on the aerosol absorption in the terrestrial IR which is mostly responsible for the stratospheric warming after an eruption. At 40 hPa (Figure 2.2b) SAGE_4λ is in good agreement with available measurements at the equator, while ST98 exhibits too low values and AER_7 overestimates the extinction until spring 1992. However, at mid-latitudes results from AER_7 at 12.1 μm are in good agreement with observations, similarly to the 1 μm extinctions (Figure 2 of supplementary material). In December 1991 at 40 hPa (Figure 2.3b), where the largest extinctions are seen, SAGE_1.8 and SAGE_1.2 significantly overestimate the extinction compared to ISAMS measurements. The SAGE_4λ calculation shows a reasonable agreement with the data, especially in the level of high extinction above 40 hPa, while ST98 results again are less than half the measurements, approaching the measurements only below 70 hPa. The low 12.1 μm extinctions from the ST98 arise both from its use of an outdated version of the SAGE retrieval algorithm and gap-filling and from a too high 1 μm to IR extinction ratio compared with observation (see Figure 2.5 of supplementary material).

The sensitivity simulations performed with the AER model show the influence of the injection mass on the extinction values. Clearly, the AER_9 and AER_10_ASAP simulations yield too high extinctions. Figure 2.3 shows that 6 months after the eruption, AER simulations generally show too large values for 1 μm and 12.6 μm extinctions at the equator. Below 70 hPa, the 12.6 μm extinction profiles of AER_7

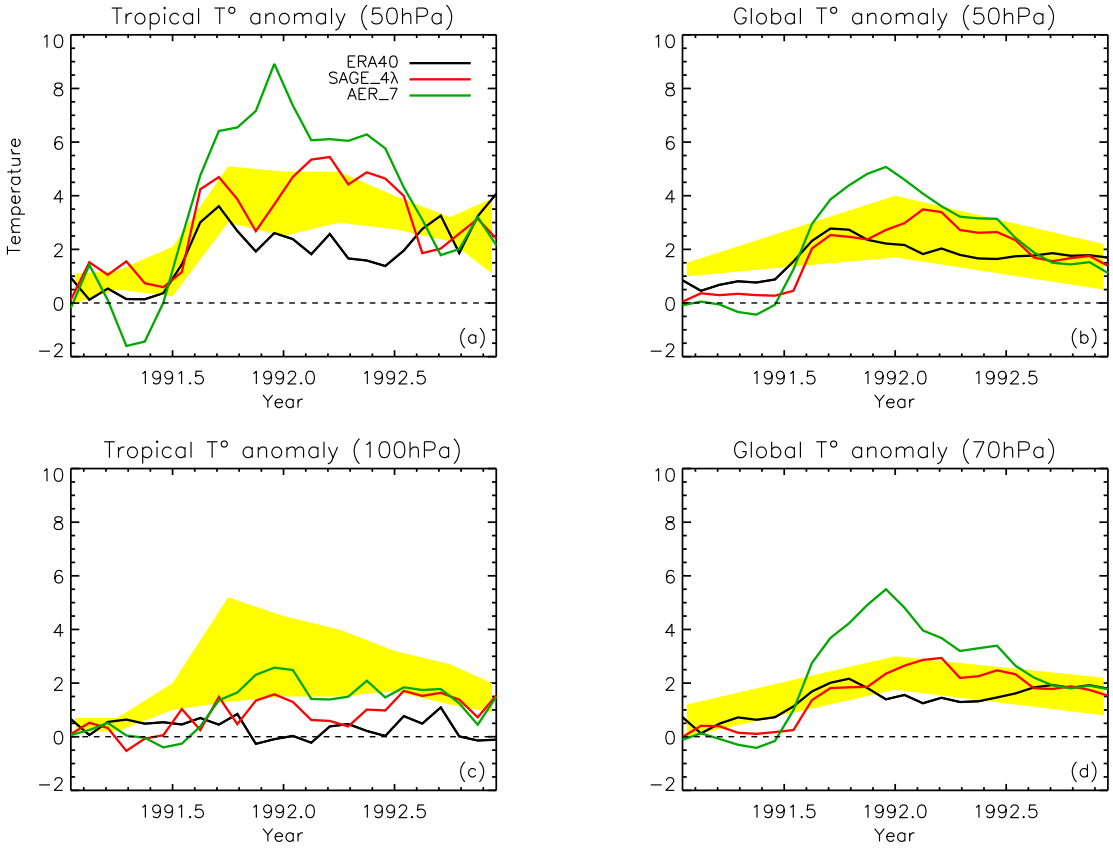

Fig. 2.4: Zonal mean temperature anomalies for tropics (20°S–20°N) at 50 hPa (a) and 100hPa (c) as well as global mean anomaly at 50 hPa (b) and (d). Scenarios anomalies (SAGE_4λ and AER_7) are computed with respect to a control simulation. Black line represents ERA-40 temperature anomalies with respect to 1995-1999. Shadings display approximate anomaly ranges calculated by general circulation models as examined in *Lanzante and Free* (2007) for (a),(c) and by chemistry climate models as examined in *Eyring et al.* (2006) in (b) and *Eyring et al.* (2010) in (d).

and AER_9 are largely consistent with observations, while the climatological winds used for AER_10_ASAP leads to a significant exaggeration at low altitudes due mainly to the absence of washout above 10 km. At mid-latitudes, AER_7 and AER_9 values are close to observations, AER_10_ASAP still being an outlier (Figure 2.7 of supplementary material).

Stratospheric temperatures. Simulations with the CCM SOCOL.v2 (*Schraner et al.*, 2008) were carried out to test the stratospheric response to the SAGE_4λ and AER_7 scenarios. The GCM part of SOCOL is based on ECHAM-4 using the ECHAM-4 radiation code. For the radiative transfer calculations spectral extinctions, single scattering albedos, asymmetry factors (as well as the surface area densities for heterogeneous chemistry calculations) directly derived from the described methods were provided as boundary conditions to SOCOL. In Figure 2.4, results are compared to the ERA-40 reanalysis and to values from different general circulation models (GCM) as shown in *Lanzante and Free* (2007) and from chemistry climate models (CCM) as shown in *Eyring et al.* (2006, 2010).

The stratospheric warming after the eruption is in general overestimated. SAGE_4λ

shows a bias between 1 K in fall 1991 to 3 K in spring 1992 in the tropics at 50 hPa compared to ERA40 data (Figure 2.4a). Compared to GCM studies using the *Sato et al.* (1993) or *Ammann et al.* (2003) datasets (*Lanzante and Free*, 2007) the SAGE_4λ is in the high range of the tropical warming overestimation, while AER_7 exhibits even larger values. In the same way, the global average temperature increase at 50 hPa from the SAGE_4λ experiment is too high by 1.5 K in spring 1992 (Figure 2.4b). The AER results are higher than the SAGE_4λ calculations for the end of 1991. The global average temperature increase at 70 hPa shows similar characteristics (Figure 2.4d). Compared to CCM studies using heating rates from *Stenchikov et al.* (1998) or derived from *SPARC* (2006) surface area density data or *Sato et al.* (1993) extinction, SAGE_4λ lies in the high range of their estimations at 50 hPa and 70 hPa. In the tropical tropopause region (100 hPa), SAGE_4λ diverges from ERA40 anomalies in late 1991 (Figure 2.4c). At 100 hPa, the SAGE_4λ approach leads to a clear improvement compared to the GCM studies, while AER_7 is inside the range of their results.

2.4 Conclusions

The volcanic eruption of Mt. Pinatubo in June 1991 is the best documented large eruption on record, however lack of measurements in the tropics in the first months after the eruption due to optical saturation limits the quality of the data. GCMs and CCMs show important variations in lower stratospheric temperatures following the Pinatubo eruption with a tendency to overestimate the warming (*Eyring et al.*, 2010; *Gettelman et al.*, 2010; *Lanzante and Free*, 2007). CCMs which implement the aerosol heating using *Stenchikov et al.* (1998) precalculated heating rates overestimate the stratospheric warming only slightly, but this apparent agreement is fortuitous, because the ST98 dataset relies on an outdated version of the SAGE retrieval algorithm and gap-filling and also shows a too high 1 μm to IR extinction ratio. GCMs, which in the past have used the *Sato et al.* (1993) GISS dataset (also based on an outdated version of SAGE II) and a fixed distribution width tend to overestimate the warming, as do CCMs using heating rates derived from *SPARC* (2006) surface area density data (*Morgenstern et al.*, 2010; *Lanzante and Free*, 2007). An erroneous prescription of the volcanic aerosol forcing can lead to a false error attribution to the radiation scheme of a specific model or hide a bias by compensating errors in the external forcing and the radiation scheme. We investigated in this study the influence of the improvement of the general satellite extinction processing algorithm and of the gap filling (*SPARC*, 2006) on the stratospheric warming after the Pinatubo eruption. Using the state-of-the-art SAGE II retrieval algorithm, we derived aerosol size distributions with different methods to calculate spectrally resolved optical properties for the Pinatubo eruption and tested the accuracy of the infrared extinctions compared to ISAMS measurements. The dataset produced using a fit to the four wavelength of SAGE II (SAGE_4λ) shows a good agreement with extinctions profiles and evolutions of both SAGE II at 1 μm and ISAMS at 12.1 μm while the dataset from Stenchikov et al., 1998 (ST98) displays too low extinctions above 20 km. The use of *SPARC* (2006) surface area density data and a fixed distribution width (SAGE_1.8, SAGE_1.2) to infer the optical parameters leads to somewhat too large extinctions at 12.1 μm compared to measurements. Re-

sults using the microphysical aerosol model AER (AER, Lexington) to generate the aerosol size distributions reveal a clear overestimation of the extinctions at the equator (even though the AER model was found to be one of the most successful aerosol models in *SPARC* (2006)) but a general good agreement in the extra-tropics.

Using the SAGE_4λ data to simulate the Pinatubo eruption in the Chemistry-Climate Model (CCM) SOCOL leads to a significant overestimation of the tropical stratospheric temperatures, by up to 3 K at 50 hPa, but a generally good agreement at 100 hPa.

For GCM and CCM simulations using volcanic forcings with longwave extinctions for the Pinatubo eruption lower than found in this study for the aerosol peak around 40-50 hPa, we argue that the stratospheric temperature increase overestimation often present in these models is unlikely due to an error in the volcanic aerosol forcing data, and could even be amplified by using a dataset closer to the SAGE_ASAP and ISAMS observations. Rather, the cause of this problem is likely due to constraints in the radiation codes of the respective models. Conversely, the warming at the tropical tropopause could be reduced by using the new SAGE_ASAP data and an appropriate size distribution retrieval. Finally our study shows that the use of the surface area density information from a principal component analysis combined with a fixed distribution width of either 1.8 or 1.2 leads to an overestimation of the infrared extinctions and therefore should be avoided.

Acknowledgments. *We would like to acknowledge funding from the Cogito foundation and from the Department of Environmental Science of ETH Zurich. Discussions with S. Fueglistaler in the early phase of this work are gratefully acknowledged.*

SUPPLEMENTARY MATERIAL

In the following, three SAGE based approaches, assuming unimodal lognormal aerosol size distributions, to calculate optical properties (extinction, single scattering albedo and asymmetry factor) are described.

1^{st} method: SAGE_4λ

In this approach, the four wavelengths of the SAGE II data are used when available. In a first step, the mode radius, distribution width σ and the number density are left practically unconstrained for each latitude/altitude point in time ($\sigma \epsilon$ [1.2, 2.6], $r_m \epsilon$ [0.015μm, 0.5μm] . The extinctions are then calculated for the available wavelengths of SAGE for all the different sets of these parameters. The different parameters are then used to calculate extinctions using Mie theory (*Mie*, 1908). The best set of parameters, minimizing the difference with the SAGE observations at all available wavelengths, is then kept. Each SAGE wavelength is weighted by its standard deviation when available from the SAGE-SPARC dataset, giving more weight to more precise measurements. To avoid unphysical abrupt changes in the mode radius in space and time, the median values of the scattered r_m calculated by the fitting method are taken for each extinction value. In the second step, these mode radii are fixed and the σ and number density are then fitted again to minimize the difference to the SAGE observations. In the gap filled region, where only the 1μm extinction is available, σ is fixed to 1.2. One modification of this method was done to describe the tropical lower stratosphere in the first month after the eruption in order to allow a fit using smaller mode radii even though this region exhibits large extinctions values. Indeed in the lower stratosphere the coagulation rate is low due to a small diffusion coefficient of aerosol particles (high pressure, low temperature). Hence, in the volcanic aerosol nucleation region, the new volcanic aerosols formed after the eruption do not coagulate quickly and the relationship between extinctions and mode radii globally verified during volcanic periods isn't validated. A similar approach as SAGE_4λ was used in Bingen et al. (2003) showing good results.

2^{nd} method: ST98

ST98 used effective radii retrieved from CLAES and ISAMS extinction measurements proposed by *Grainger et al.* (1995) and *Lambert et al.* (1997). In general there is a good corespondence to effective radii retrieved from SAGE II. They assumed a fixed distribution width of σ=1.25 (which matched best with CLAES optical depth at 2.6 μm). In a first step ST98 calculated the extinction for a number density of one particle per cm^3 and in a second step scaled the number density to fit the extinction at 1.02 μm with SAGE II measurements. ST98 use an old SAGE II data set (*Russell et al.*, 1996) with an older satellite retrieval procedure and a very simplified gap-filling approach (the last measured SAGE II value in the vicinity is taken to fill the gap). The optical properties are then calculated with Mie theory (*Mie*, 1908) assuming H_2SO_4 solution droplets of 70 %.

3^{rd} method: SAGE_1.8 - SAGE_1.2

Based on a principal component analysis using four wavelength of SAGE II, *Thomason et al.* (1997b) found the following relationship between 1000 nm extinction and the surface area density. SAD:

$$SAD = \begin{cases} 425 \times k^{0.68} & \text{for } k < 4 \times 10^{-3} \\ 1223 \times k^{0.875} & \text{for } 4 \times 10^{-3} < k < 2 \times 10^{-2} \\ 2000 \times k & \text{for } 2 \times 10^{-2} < k \end{cases} \tag{2.1}$$

where k is the extinction coefficient at 1000 nm in km^{-1} and SAD is in $\mu m^2/cm^{-3}$. This relationship is based on the assumption that the wavelength dependence of the extinction is stable for different aerosol extinctions. This assumption is justified for most cases. For SAD around 0.1 $\mu m^2 cm^{-3}$ the uncertainty ranges within $\pm 30\%$, for SAD greater than 10 $\mu m^2 cm^{-3}$ within $\pm 15\%$ (*Thomason et al.*, 1997a). However, after the Mt. Pinatubo eruption this relationship differs significantly in the tropical lower stratosphere from the real SAD. This deviation is caused by conjunction of small aerosol size and large extinction after the injection of large amounts SO_2 by the eruption (*SPARC*, 2006, Chapter 4, pp. 138 ff). Unfortunately there are no aerosol size distribution measurements in the tropics during that time, for example using the OPC, but it is conceivable that due to changes in the size distribution in post-volcanic times this relationship can lead to significant errors.

Similarly to the SAD the effective radius r_{eff} can be retrieved from the extinction at 1000 nm as following:

$$r_{eff} = \begin{cases} 0.0303 \times [\ln(k) + 11.515] + 0.16 & \text{for } 1 \times 10^{-5} < k < 3.0 \times 10^{-4} \\ 0.15 \times \exp(0.04916 \times [\ln(k) + 11.513]^2) & \text{for } 3.0 \times 10^{-4} < k < 1.8 \times 10^{-3} \\ 0.55 & \text{for } 1.8 \times 10^{-3} < k \end{cases} \tag{2.2}$$

Schraner et al. (2008) assumed σ to 1.8 (SAGE_1.8), which is a mean value for the last few decades. However, after volcanic eruptions σ can differ substantially from this value. Following Stenchikov et al., 1998 we repeated the calculation for σ=1.2 (SAGE_1.2), which is close to the value for the large mode after large volcanic eruptions. The extinction is very sensitive to σ. For the same aerosol mass, if σ is large, there are fewer but bigger particles. This affects the radiative properties of the aerosol layer: For the same total mass, smaller particles scatter shortwave radiation more efficiently, but absorb longwave radiation almost to the same degree as larger particles. The number density N_0 is finally calculated out of the SAD, σ and r_{eff}

The main difference between SAGE_1.8 - SAGE_1.2 ,SAGE_4λ and ST98 approaches is the estimation of the number density N_0. SAGE_1.8 - SAGE_1.2 follow the approach of SAD conservation from a Principal Component Analysis study (Thomason et al., 1997a), whereas SAGE_4λ/ST98 define the number density such that the extinctions in the shortwave match best the observations.

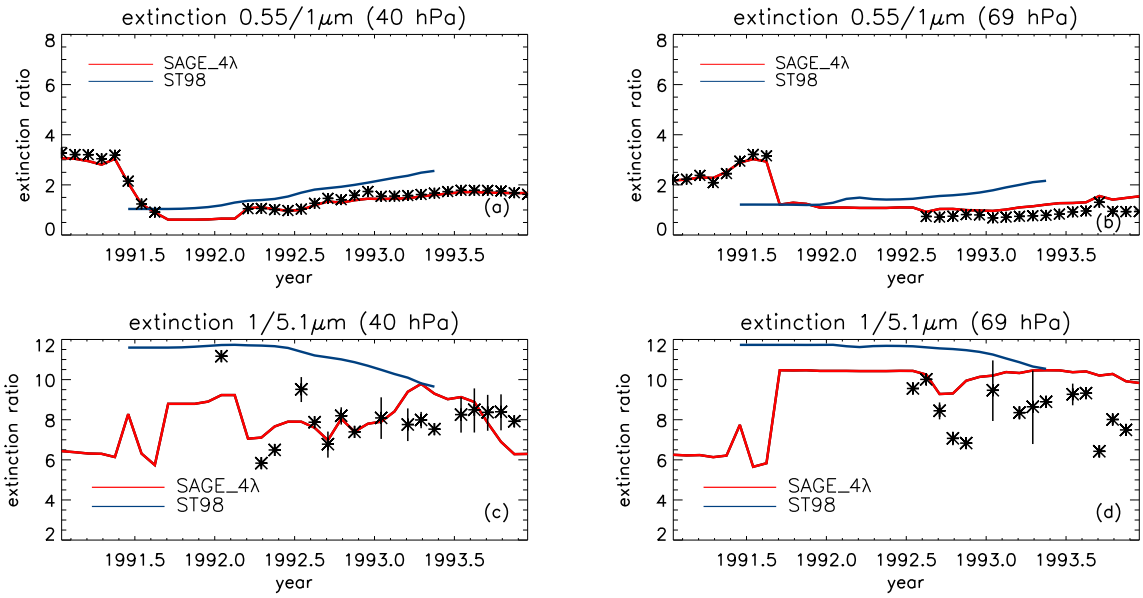

Fig. 2.5: Extinction ratio of 0.55 μm/1 μm (a,b) and 1 μm/5.1 μm (c,d). At the equator at 40 hPa altitude (a,c) and at 69 hPa altitude (b,d). Asteriks in (a,b) show ratio of SAGE II 0.55 μm/1 μm (*SPARC*, 2006) and asteriks in (c,d) show ratio of SAGE II 1 μm and HALOE 5.1 μm.

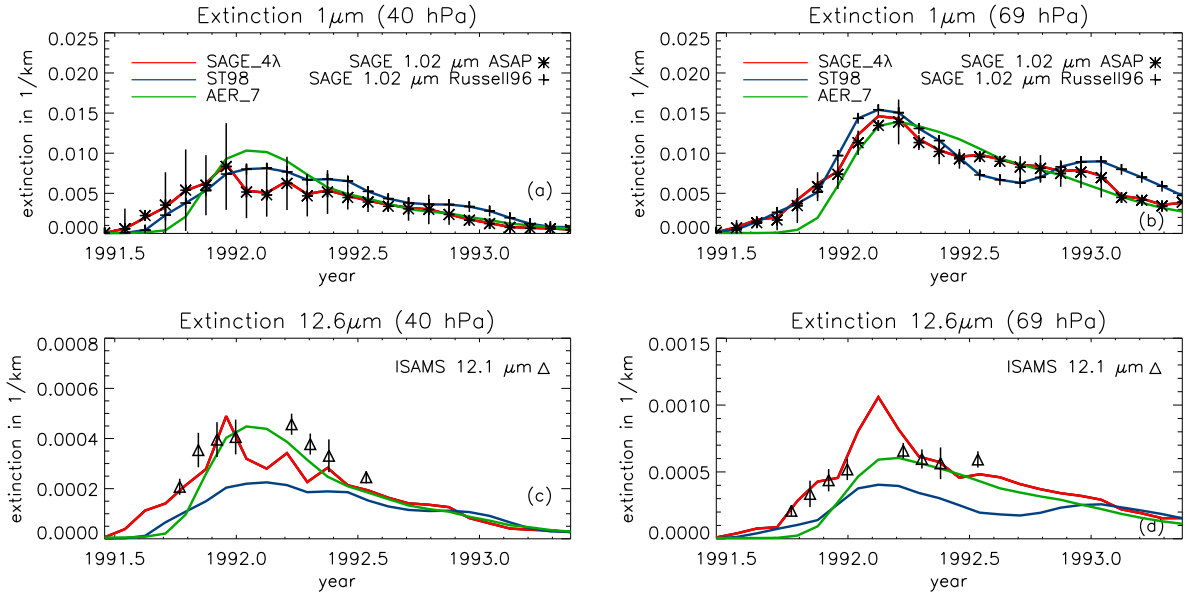

Fig. 2.6: Zonal mean extinction from June 1991 to June 1993 for 1 μm and 12.6 μm at 30°–40°N. Left column at 40 hPa, right column at 69 hPa. Vertical lines show standard deviations of measurements when available.

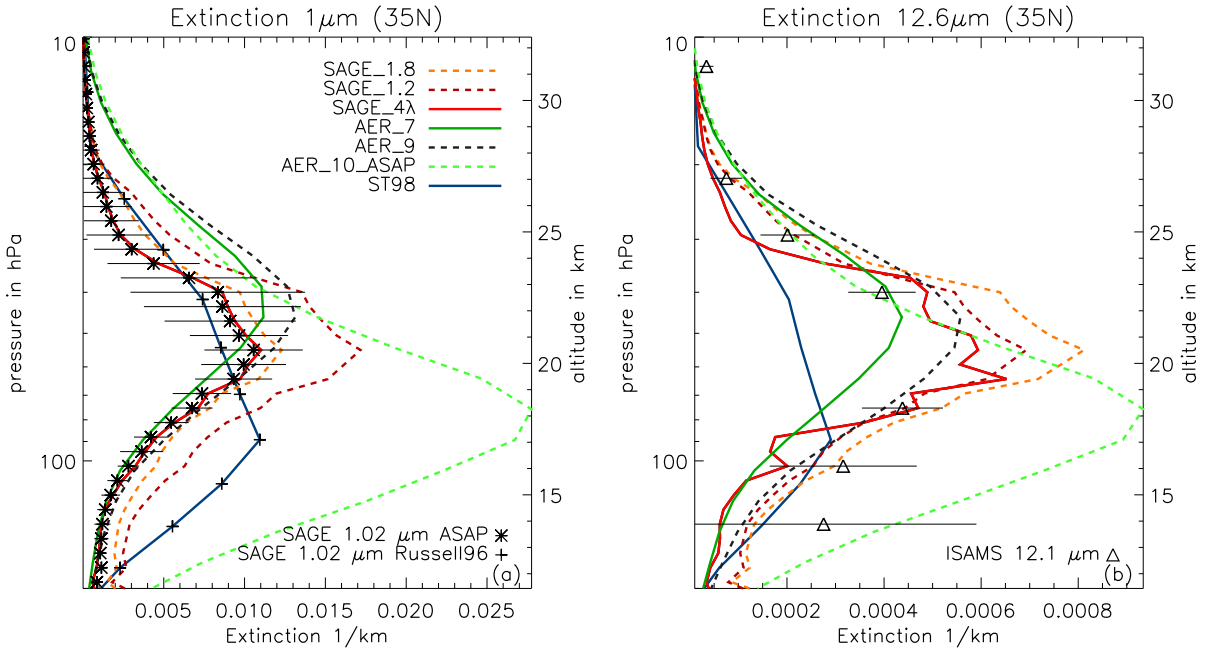

Fig. 2.7: Zonal mean extinction in December 1991 at 1 μm and 12.6 μm at 30-40°N. Horizontal lines show standard deviations of measurements.

Chapter 3

Volcanic forcing for climate modelling (1600-2011)

F. Arfeuille[1], D. Weisenstein[2], H. Mack[1], E. Rozanov[1,3], T. Peter[1], and S. Brönnimann[4]

[1] Institute for Atmospheric and Climate Science ETH Zurich, Zurich, Switzerland
[2] AER, Lexington, Massachusetts, USA. (Now at Harvard University, Cambridge, MA, USA)
[3] Physical-Meteorological Observatory/World Radiation Center, Davos, Switzerland
[4] Oeschger Center for Climate Change research and Institute of Geography, University of Bern, Bern, Switzerland

In preparation for publication in Clim. Past.

Abstract
As the understanding and representation of the volcanic eruption impacts on climate improved in the last decades, uncertainties in the stratospheric aerosol forcing from large eruptions are now not only linked to visible optical depth estimates on a global scale but also to details on the size, latitude and altitude distributions of the stratospheric aerosols. Based on our understanding of these uncertainties, we propose a new model-based approach to generate a volcanic forcing for General-Circulation-models (GCM) and Chemistry-Climate-models (CCM) simulations. This new volcanic forcing covering the 1600-2011 period uses an aerosol microphysical model to provide a realistic, physically consistent, treatment of the stratospheric sulfate aerosols. Twenty-six eruptions were modeled individually using the latest available ice cores aerosol mass estimates and historical data on the latitude and date of eruptions. Aerosols spatial and size distribution evolutions after the sulfur dioxide discharge are hence characterized for each volcanic eruption. Large variations are seen in hemispheric partitioning and size distributions in relation to location/date of eruptions and injected SO_2 masses, and results for recent eruptions are in good agreement with observations. By providing accurate amplitude and spatial distributions of shortwave and longwave radiative perturbations by volcanic sulfate aerosols, we argue that this volcanic forcing may help refine the climate model responses to the large volcanic eruptions since 1600. The final dataset consists in 3D values of aerosol concentrations and sizes which can in turn be used to calculate extinctions, single scattering albedos and asymmetry factors for different wavelength bands. Surface area densities for heterogeneous chemistry are also made available.

3.1 Introduction

For climate simulations covering the last centuries the volcanic forcing is a crucial external influence and needs to be included as precisely as possible. It is now commonly accepted that explosive volcanism is, together with the solar variability, one of the most important pre-industrial forcing explaining a large part of the decadal variance in the past centuries (*Hegerl et al.*, 2003). Moreover, on the centennial timescale its strong effect on oceanic heat content has been recently stressed (*Gleckler et al.*, 2006; *Stenchikov et al.*, 2009; *Gregory*, 2010). However, as stated in the latest IPCC report (*Forster et al.*, 2007), the level of scientific understanding of the volcanic influence is still low, one reason being the large uncertainties in the volcanic aerosol data before 1980.

Volcanic stratospheric aerosols impact climate through several mechanisms related to the increased scattering of the solar radiation and increased absorption of solar and terrestrial infrared radiations. These changes modify the radiative budgets in the stratosphere and troposphere and leads to important temperature changes which then impact ozone and potentially stratospheric water vapor. Dynamical responses to the final net radiative forcings further modify the climate response and can lead to regional anomalies of temperature (ie.Winter warming, (*Robock and Mao*, 1992; *Stenchikov et al.*, 2006)) and precipitation (*Robock and Liu*, 1994; *Joseph and Zeng*, 2011).

To describe the diverse mechanisms involved as accurately as possible, General Circulation Models (GCMs) and Chemistry-Climate Models (CCMs) need information about the mass and size distribution of the aerosols for every latitude and altitude. Through Mie theory (*Mie*, 1908), relevant optical parameters can then be calculated: Extinction, single scattering albedo and asymmetry factor. In addition, the surface area density (SAD) of the aerosols can be used to calculate heterogeneous reactions with ozone.

If these informations can be satisfactorily derived from satellite data for the most recent period and especially the Pinatubo 1991 eruption, despite saturation issues (*Stenchikov et al.* (1998), Chapter 2 of this thesis); lack of extensive extinction measurements before 1979 prevent a direct inference of the volcanic aerosols optical parameters. For the 1883-1978 period volcanic aerosols datasets are based on isolated solar extinction data (*Sato et al.*, 1993) and before 1883 ice core aerosol mass estimates are used (*Sato et al.*, 1993; *Ammann et al.*, 2003; *Crowley et al.*, 2008; *Gao et al.*, 2008). However, this limited information is not sufficient to derive the necessary optical parameters by themselves and has to be supplemented by parametrisations and assumptions on the evolution of the size and spatial distribution of the aerosols with time. The most common approaches used in volcanic aerosols datasets and GCM modeling studies to create and implement the volcanic forcing are summarized in section 3.2.

In this study we present a new volcanic stratospheric aerosol dataset using the latest ice core data from *Gao et al.* (2008) and covering the 1600-2011 period. The approach is based on simulations made with the state-of-the-art two dimensional aerosol model AER (*Weisenstein et al.* (2007), Atmospheric and Environmental Research Incorporation, Lexington, USA). It allows the size distributions to be directly derived from the microphysical processes described in the model for each individual eruption, while the spatial distribution is mainly dependent on the boundary conditions (latitude and altitude of SO_2 injection, date of eruption), climatological winds and sedimentation speed. This dataset differs in its conception from previous volcanic forcing reconstructions in several ways which are described in section 3.3. Technical details on the boundary conditions used for each of the 26 eruptions present in the dataset as well as a short description of the AER model is presented in section 3.4. Main results of the reconstruction are then shown and compared to previous studies in section 3.5. Finally section 3.6 gives information on the format of the datasets released.

3.2 Previous datasets and approaches

As summarized in the IPCC AR4 report, recent climate simulations implement the volcanic forcing in different ways, from the direct use of a global or latitudinally dependent radiative forcing (*Crowley et al.*, 2003; *Goosse et al.*, 2005; *Stendel et al.*, 2006), to prescribed aerosol optical depth (AOD) changes with interactive calculations of the longwave and shortwave radiation budgets (*Tett et al.*, 2007).

For climate simulations covering a period prior to 1850, start of the *Sato et al.* (1993) GISS dataset, direct parametrisations are often used to convert aerosol loadings to optical depths (for instance by dividing the aerosol mass by 150 Tg as proposed by *Stothers* (1984)) or to convert optical depth to radiative forcing by multiplying it by -20, as in *Wigley et al.* (2005). An additional factor can then be used for the conversion in order to take into account the non-linearity of the shortwave forcing/aerosol mass relationship due to the decreasing scattering efficiency as particles grow through enhanced coagulation (*Hegerl et al.*, 2011).

The *Crowley et al.* (2008) volcanic aerosol dataset provides effective radii in addition to optical depth data. For the modeling studies using this dataset, the approach consists in distributing the AOD at chosen vertical levels. The extinction, single scattering albedo and asymetry factor are then calculated using the effective radii from the dataset and a constant distribution width. This methodology was for instance used in *Jungclaus et al.* (2010), with an assumed distribution width of 1.8 and the AOD distributed over the 20-86 hPa pressure levels. The calculated spectral extinctions are very sensitive to the choice of

distribution width, which can vary from a value of 1.8 in background quiescent conditions to 1.2 for the volcanic large mode after a strong eruption, and should be chosen with care. For instance, a distribution width of 1.8 associated with the use of the surface area density data and effective radius data calculated from SAGE II (*Thomason et al.*, 1997b; *SPARC*, 2006) in order to derive the aerosol size distribution leads to too large extinctions in the infrared (Chapter 2).

Until every GCM/CCM include coupled stratospheric aerosol microphysical modules, there is a need for an external dataset providing 3D spatial information, from aerosol concentrations to spectrally resolved optical properties. The currently most used forcing datasets applied in recent modeling studies are now described in subsections 3.2.1- 3.2.4.

3.2.1 Sato et al., (1993)

The *Sato et al.* (1993) optical depth dataset (and updates) cover the 1850-present period. It provides optical depth at 0.5 μm with varying latitude resolution over time. It is based on several sources. In the earlier time period (1850-1882), optical depths are derived from Mitchell's index (*Mitchell*, 1970) based on volume of ejectas. The AOD is then spread along every latitude, except for the Askja 1875 eruption (30°N-90°N). In 1883-1959 measurements of atmospheric extinctions are used. Most of the stations then are in the mid-northern latitudes. Southern hemisphere optical depth are estimated based on the latitudes of large known eruptions. Hence for a tropical eruption the Southern hemisphere AOD is taken to be the same as measured in the Northern hemisphere. It can be noted that the Krakatau 1883 eruption was originally described using a single measurement station in Montpellier (44°N), but is since a 2002 update derived from the latitudinal distribution of the Pinatubo aerosol cloud. For 1960-1978, southern hemisphere stations could also be used as well as lunar eclipses data. From 1979 on, satellite measurements are used. It can be noted that a new version of the SAGE II satellite data is now available (*SPARC*, 2006) and differ substantially from previous ones (see Chapter 2).

3.2.2 Ammann et al., (2003)

The *Ammann et al.* (2003) volcanic dataset (1890-1999) provides individual evolutions of volcanic aerosols for each eruption. Latitudinal transport is parametrised. Transport from the tropics to the mid-latitudes is assumed to take place in the lower stratosphere in the winter hemisphere only. The temporal evolution is constrained by specific e-folding decays (eg. 12 months in the tropics) and a linear buildup. This simple model of the evolution of the aerosols cannot describe the details of the transport and sedimentation of the aerosols but compared to *Sato et al.* (1993) an advantage is the absence of changes in data sources which can introduce a factitious decadal variability (*Ammann et al.*, 2003). The peak optical depths are scaled from the peak aerosol loadings (from Stothers et al.,1996, Hofman and Rosen 1983, and Stenchikov et al., 1998) assuming a fixed 75 wt% aerosol composition and a fixed aerosol size distribution (with an effective radius of 0.42 μm).

3.2.3 Crowley et al., (2008)

Crowley et al. (2008) provides monthly aerosol optical depth at 0.55 μm and effective radius for four latitudinal bandsfor the 850-2000 period. Optical depths are derived using a calibration from Antarctic sulfate records of Pinatubo and Hudson 1991 eruptions against satellite based optical depth from *Sato et al.* (1993). In total 22 ice cores are used. The

obtained time serie was validated for Krakatau, Santa Maria and Katmai against *Stothers* (1996). Effective radiuses growth and decay are derived from Pinatubo 1991 satellite observations and scaled using microphysical calculations from *Pinto et al.* (1989) for eruptions larger than Pinatubo.

3.2.4 Gao et al., (2008)

The *Gao et al.* (2008) study which analyzed 54 polar ice cores led to the release of two distinct datasets: First an aerosol injection forcing which describes the mass of aerosols released for each volcanic eruptions for both hemispheres (for the 500-2000 period). This is directly derived from the ice cores after calibration.

The hemispheric calibration factors for Greenland and Antarctica cores, linking the sulfate depositions measured in the ice for each polar region (in kg/km^2) and the total mass of stratospheric aerosol formed after the eruption (in kg), cannot be calculated from the same method due to limitations in the measurements in the recent period. In *Gao et al.* (2008), northern hemisphere (NH) calibration factors for tropical eruptions are derived from nuclear bomb tests, while southern hemisphere (SH) factors are calculated using Mt.Pinatubo eruption data. In the final *Gao et al.* (2008) dataset, the calibration factor from sulfate deposition (in kg/km^2) in NH and SH to global stratospheric loading is set to the mean value of $1\times10^9 km^2$ for all tropical eruptions regardless of the NH/SH partitioning which however modifies the hemispheric calibration parameters (*Gao*, 2008). Hence, ice cores hemispheric estimates can be challenged and one example of the uncertainty arising from the differences in partitioning is the discrepancy for the Agung eruption. For this eruption, the ice core calibration leads to an even hemispheric partitioning of the aerosols after calibration while observations indicate a much larger loading in the SH (*Stothers*, 2001). This discrepancy could also be attributed potentially to a concomiting high latitude eruption (Surtsey, Iceland) (*Gao et al.*, 2007). As noted in *Gao* (2008), uncertainties in hemispheric values due to variations in hemispheric partitioning of tropical eruptions partly compensate in the calculation of the global injection mass as an underestimation of SH loading would correspond to an overestimation of the NH loading.

The total mass injected (but not the partitioning into hemispheres) is used in our study to infer the SO_2 emission inputs for the AER-2D model and will be described in subsection 3.4.1.

The second dataset provided is a full latitude/altitude distribution of the aerosol concentration, varying monthly. The altitude-latitude evolution is derived from a parametrisation of the transport between tropics, extratropics and poles (for instance transport from tropics to extratropics is set to a 50% mass ratio per month). No inter-hemispheric transport is allowed and separate injections are made in the two hemisphere in order to match the ice cores mass estimates. A linear build-up of the total aerosol mass during the first four months after the eruption is prescribed while an exponential decrease of the stratospheric aerosol mass is assumed, with a global e-folding time of 12 months. The e-folding time in the tropics is 36 months (little sedimentation), 12 months in the extra-tropics (tropopause folding), three months for the winter polar region (stronger subsidence) and six months for the summer polar region. *Gao et al.* (2008) uses vertical distribution from Mt.Pinatubo based on the observation that the vertical distributions of volcanic aerosols have a similar shape (Pinatubo, Agung, El Chichón and Fuego eruptions observations) and peak only at slightly different heights depending on altitudes of initial injections. The variations in altitude distribution from an eruption to another does not strongly affect the global surface radiative forcing, but may affect the transport of the aerosols in the stratosphere (see subsection 3.5.2).

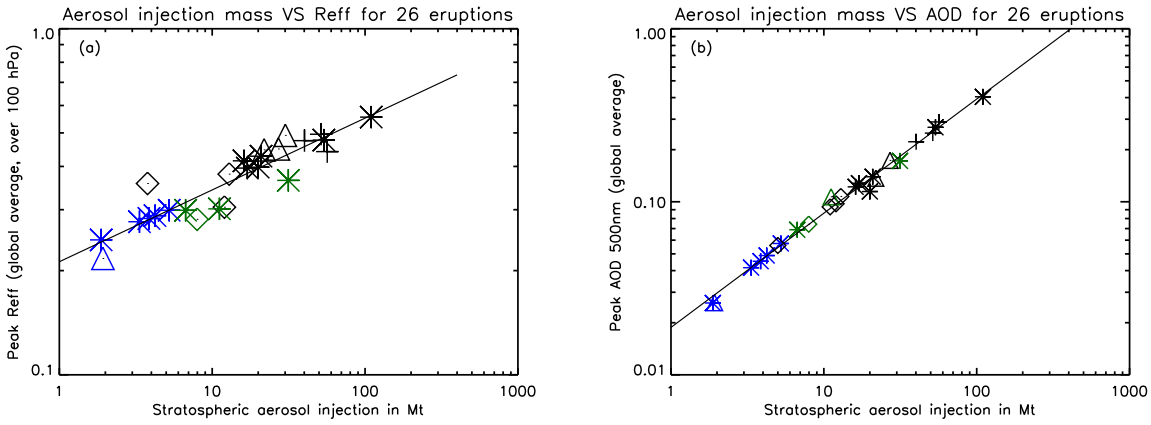

Fig. 3.1: Total mass of aerosol (H_2SO_4+H_2O) in Mt versus (a) calculated peak of effective radius by the AER model for each of the 26 modeled eruptions over the 1600-2000 period (effective radius values are global mean average above 100 hPa, and (b) peak AOD at 500 nm. Black line shows the logarithmic fit for the tropical eruptions. Stars indicate spring eruptions, triangles summer eruptions, diamonds fall eruptions and crosses winter eruptions. Black color indicates tropical eruptions, while blue and green colors indicate extratropical eruptions in the southern and northern hemispheres respectively.

3.3 Specificities of our dataset

In regards of the latest studies on the influence of volcanic eruptions on the stratosphere and climate and the current ability of GCMs and CCMs in modeling these eruptions, volcanic forcing datasets should describe as precisely as possible :

1. The global average AOD peaks in the shortwave: In our study this is mostly dependent on the estimated global SO_2 mass release, derived from the state-of-the-art ice core reconstruction of *Gao et al.* (2008). As seen in Figure 3.1 (b), the relationship between aerosol mass and AOD peak is stable, as the maximum AOD does not depend on a large extent to spatial and temporal variations in individual volcanic eruptions. It should be noted that important differences in the magnitude of many eruptions are present in existing datasets. For instance, the Krakatau eruption of 1883, previously thought to have released more SO_2 than Pinatubo, is now downgraded to a 2/3 Pinatubo release by *Gao et al.* (2008) and the Cosiguina 1835 eruption while being present in most ice core reconstructions (*Zielinski*, 1995; *Gao et al.*, 2008) is absent of the *Stothers* (2007) dataset based on lunar eclipses. An aerosol optical depth background value is also present in our dataset in conformity to observations during volcanically quiescent periods.
2. The latitude-altitude distribution: In this study the spatial distribution is modeled through the AER-2D microphysical scheme and depends on nucleation, condensation, coagulation, sedimentation and climatological transport. Initial distribution and subsequent transport depends on specific latitudinal position of the volcanoes and dates of eruption. Spatial distribution evolutions with time and initial formation of the aerosols are directly derived from microphysical processes described in AER-2D. Differences in the initial altitude distribution of the volcanic SO_2 is also accounted for in this study, using information from the one dimensional Plumeria volcanic plume model (*Mastin et al.*, 2009) when data is available.
3. The size distribution: It is important to characterize the mass scattering efficiency and longwave forcing of the aerosols as well as their sedimentation speed. Using an

aerosol microphysical model allows to describe the size distributions at each location and time for every specific eruption. The absorption/scattering ratio and its dependence to the eruption size (*Timmreck et al.*, 2009) is hence taken into account, preventing an overestimation of the shortwave decrease and underestimation of the longwave absorption following large eruptions. The AER-2D model has a 40 size bins resolution. Figure 3.1 (a) shows the variations in effective radii for each of the 26 eruptions as simulated by the AER model.

Year (A.D.)	NH (Tg)	SH (Tg)	Confirmed or tentative attribution (time,latitude)
1600	46.0	10.5	Huaynaputina (February 19^{th}, 16.6°S)
1619	0.0	5.2	Unknown SH (No large eruption recorded)
1641	33.8	17.8	Parker (January 4^{th}, 6°N)
1673	6.3	9.8	Gamkonora (May 20^{th}, 1.4°N)
1693	0.0	27.0	Serua (June 4^{th}, 6.3°S)
1711	0.0	3.9	Unknown SH (No large eruption recorded)
1719	31.5	0.0	Unkown NH (No large eruption recorded)
1729	12.0	0.0	Unkown NH (No large eruption recorded)
1738	0.0	3.3	Unknown SH (No large eruption recorded)
1755	8.0	0.0	Katla (October 17^{th}, 63.4°N)
1761	8.4	4.5	Makian (September 22^{nd} 1760, 0.20°N)
1783	93.0	0.0	Laki. (Mainly tropospheric)
1794	0.0	1.9	Unknown SH (No large eruption recorded)
1796	6.7	0.0	Unknown NH (No large eruption recorded)
1809	27.6	26.2	Unknown Trop. Feb eruption (*Cole-Dai et al.*, 2009)
1815	58.7	51.0	Tambora (April 10^{th}, 8°S)
1831	17.0	0.0	Babuyan Claro (19.5°N, date Unknown)
1835	26.4	13.8	Cosiguina (January 20^{th}, 13°N)
1861	0.0	4.2	Unknown SH (No large eruption recorded)
1883	11.2	10.7	Krakatau (August 27^{th}, 6°S)
1886	0.0	1.9	Tarawera (June 10th, 38°S)
1902	0.0	3.8	Santa Maria (October 24^{th}, 14°N)
1912	11.0	0.0	Katmai (June 6^{th}, 68°N)
1925	11.2	0.0	Unknown NH (No large eruption recorded)
1943	6.6	0.0	Unknown NH (No large eruption recorded)
1963	7.6	13.3	Agung (March 17^{th}, 8°S)
1976	4.7	0.0	Fuego (October 10^{th} 1974, 14°N)
1982	7.0	7.0	El Chichón (March 29^{th} 1982, 17.2°N)
1991	15.0	15.0	Pinatubo (June 15^{th}, 15°N). Not derived from ice cores

Table 3.1: Stratospheric aerosol data from *Gao et al.* (2008) after ice core calibrations for northern and southern hemispheres. Attribution of the aerosol peaks to specific volcanic eruptions in this study. Tg amounts correspond to the total aerosol mass (H_2SO_4+H_2O) assuming a 75wt% of H_2SO_4.

3.4 Technical description of the dataset

3.4.1 Injection data

Table 3.1 shows the sulfate aerosol mass estimates from *Gao et al.* (2008) for northern and southern hemispheres for each eruption recorded. From this data, the Laki 1783 eruption was not used for our final dataset as the SO_2 release was mainly tropospheric (*Highwood and Stevenson*, 2003), while the eruptions in 1925 and 1943 were removed as they are not appearing in any available observations and no known large eruption were recorded around these periods. The Pinatubo eruption is not derived from ice core measurements as no ice core data is available from Greenland and was added in *Gao et al.* (2008) based on satellite data. In the same manner, we added the El Chichón eruption of 1982 and displaced the 1976 northern hemisphere eruption to the large tropical eruption of Mt.Fuego of October 1974.

3.4.2 Preprocessing of model input

3.4.2.1 Calculation of SO_2 amount

First, the aerosol mass is converted to a SO_2 injection mass for each volcanic eruption:

$$m_{SO_2} = m_{aero} * wt\%_{H_2SO_4} * \frac{M_{SO_2}}{M_{H_2SO_4}} \tag{3.1}$$

With m the mass of the compounds, M their molecular weight and $wt\%$ the percentage in mass of H_2SO_4 in the aerosols.

Sulfuric aerosol total amount (NH+SH) is used to calculate SO_2 initial release assuming a 100% conversion efficacity and a H_2SO_4 average composition of 75wt%. This is used for consistency with the average composition asssumed for the ice core parametrisation in *Gao et al.* (2008). For the optical properties calculations, the H_2SO_4 wt% is set to match high temperatures after a strong volcanic eruption, in order to minimize the absolute error arising from not using the actual composition (which depends on the temperature).

3.4.2.2 Attribution to specific eruptions

Some tentative attributions of sulfate peaks in ice cores to specific historical eruptions were made in this study when large historical eruptions (data from the Global Volcanism Program of the Smithsonian Institution) have a consistent location and timing of eruption compared to the loadings given by *Gao et al.* (2008). This is the case for the Parker (Jan 1641, Philippines), Gamkonora (May 1673, Indonesia), Serua (Apr 1693, Indonesia), Katla (Oct 1755, Iceland), Makian (Sep 1761, Indonesia) and Babuyan Claro (1831, Philippines) eruptions.

3.4.2.3 Timing and latitude of injection

The latitudinal distribution of the injection is given by the location of the volcanoes. For tropical eruptions, it was observed that a few weeks after the eruption, SO_2 spread quickly inside the tropical pipe region. Injection in AER-2D was made depending on the exact latitude of the volcanoes inside one or two bands in the 15°S-15°N region. The latitudinal position of the tropical pipe given the time of year then affects the transport inside the tropics. When unknown, eruptions recorded only in the northern/southern hemisphere are set respectively to high northern latitudes (55°-65°N) and southern hemisphere mid-latitudes (40°S). As in *Gao et al.* (2008), the location of an eruption is set to tropical if unknown but recorded in both hemispheres. This is the case only for the Unknown 1809 eruption.In the same way as in *Gao et al.* (2008), the timing of an eruption is set to April if the eruption is unknown, except for the eruption date of the 1809 eruption which was set to February (*Cole-Dai et al.*, 2009). As only high latitudes eruptions in our dataset have unknown dates of eruptions, no tropical eruption was artificially set to an April eruption, hence no bias towards a specific hemispheric partitioning is introduced in the dataset.

Eruptions	Prev. work : Max	Plumeria: Max	NBH	Sources
Huaynaputina	33-37	33.5-35	24.5-25	*Thouret et al.* (1999)
Tambora	23-44	30.5-36.5	23-26.5	*Sigurdsson and Carey* (1989)
Cosiguina	25-28	26	20	*Self et al.* (1989)
Krakatau	25	33-33.5	24	*Self and King* (1996)
Tarawera	27.8	28-28.5	20-21	*Self and Rampino* (1981)
Santa Maria	35	38	27-27.5	*Williams and Self* (1983)
Katmai	17-26	20.5-25	15.5-18.5	*Sigurdsson et al.* (1984)
Agung	23-28	27	21-22	*Self and King* (1996)
El Chichón	27.3-31.6	29-32.5	18-25	*Sigurdsson et al.* (1984)
Pinatubo	34-40	33.5-34	24-24.5	(*)

Table 3.2: Altitude (km) of Maximum injections for previous studies and Plumeria simulations, as well as altitudes of neutral buyancy in Plumeria.
(*) : (*Fero et al.*, 2009; *Kayzar et al.*, 2009; *Koyagushi and Tokuno*, 1993; *Pallister et al.*, 1992; *Baker and Rutherford*, 1996; *Newhall et al.*, 1996; *Self et al.*, 2004; *Stix and Kobayashi*, 2008)

3.4.2.4 Altitude of injection

In the tropical reservoir region where most of the SO_2 mass from large eruptions is released, even a small altitude difference can theoretically affect the timing of the transport to the extra-tropics. The altitude of injection is taken from the Plumeria model (*Mastin et al.*, 2009) when enough eruption parameters are known. Otherwise, same as Pinatubo is taken. Results summarized in Table 3.2 indicate for instance that the neutral buoyancy height of the SO_2 release by the Agung 1963 eruption was significantly lower than the one of the Pinatubo eruption. Results are subject to caution as dynamical parameters used to infer the mass flux of the eruptions are uncertains. An additional difficulty in estimating the SO_2 altitude

distribution arises from the fact that some eruptions involve distinct plinian phases as well as a co-ignimbrite phase (Herzog and Graf., 2010).This was the case for Mt.Tambora 1815 eruption. Ejecta mass released for each of the phases are then difficult to infer and an additional difficulty is that their specific SO_2 contents depend on its partitioning in the subvolcanic magma reservoir.

3.4.3 AER model

The two-dimensional sulfate aerosol model developed at AER (Atmospheric and Environmental Research Incorporation, Lexington, USA) was used to model 26 volcanic eruptions in the 1600-2011 period. For validation of the model against observations see *Weisenstein et al.* (1997); *SPARC* (2006); *Weisenstein et al.* (2007). The model includes the following species: SO_2 , OCS, DMS, H_2S, and CS_2. For the volcanic eruption the sulfur is put into the stratosphere in form of SO_2. The model uses pre-calculated photolysis rates, derived from a model calculation with standard stratospheric chemistry (*Weisenstein et al.*, 1997). Reaction rates are according to *Sander et al.* (2000). Sulfuric acid aerosols (H_2SO_4 /H_2O) are calculated from the surface to 60 km with 1.2 km vertical resolution. The horizontal resolution is 9.5°. The model accounts for significant recycling of gaseous H_2SO_4 into SO_x in the upper stratosphere via photolysis. The sulfate aerosols are treated as liquid binary solution droplets (or ternary solution droplets in polar regions). The size distribution (with 40 size bins spanning the range 0.4 nm - 3.2 m) of aerosol particles is defined by micro-physical processes as nucleation, condensation, evaporation, coagulation, sedimentation and (tropospheric) washout.

Transport parameters are based on *Fleming et al.* (1999) and are calculated from observed O_3, water vapour, zonal wind, and temperature for climatological conditions (transient for Pinatubo eruption). Wave driving by planetary and gravity waves is included as well.

3.5 Results

3.5.1 Size distributions

The influence of the various injection masses on the effective radii of the aerosols and subsequently on the evolution of the AOD is discussed here. Figure 3.1(a) shows the increase in effective radius with increasing eruption size due to intensification in the coagulation process from small to large eruptions because of increased aerosol concentrations in the stratosphere. We can note that northern hemisphere extratropical eruptions tend to exhibit smaller effective radii than tropical eruptions for a given SO_2 erupted mass. This could be due to a faster and more important mixing of the injected SO_2 and fresh aerosols.

The peak AOD (global average, Figure 3.1(b)) ratio between two eruptions follows very closely the relation:

$$\frac{AOD_2}{AOD_1} = (\frac{M_2}{M_1})^{2/3} \tag{3.2}$$

With M representing the mass of stratospheric aerosols and AOD the peak of the optical depth at 500 nm. This idealized relationship is a consequence of the total aerosol mass being proportional to the volume of the aerosols while the optical depth at 500 nm is proportional to their surfaces. The actual equation linking our calculated global mean peak AOD to the aerosol masses given in *Gao et al.* (2008) is:

$$AOD_{peak} = 0.02 * M^{0.658} \tag{3.3}$$

The AOD values for each individual eruption can differ from the retrieved relationship between aerosol mass and AOD by 20%-30% due to differences in the latitude and altitude of the injections. Also, the extinctions of the 26 volcanic eruptions simulated for the 1600-2011 period have large variations in terms of latitudinal and time distribution.

Following *Toohey et al.* (2011), the cumulated optical depths for the two years after each eruptions are computed. Figure 3.2 (a) shows the relation:

$$AOD_{cumul2yrs} = 0.45 * M^{0.514} \tag{3.4}$$

The diminished power law compared to Equation 3.3 shows the effect of the faster sedimentation for increasing SO_2 mass as aerosols get larger. Using the Equation 3.4 to calculate the cumulative AOD for 17 Mt and 700 Mt SO_2 eruptions as simulated in *Toohey et al.* (2011) using MAECHAM5-HAM, we get optical depth of 2.76 and 18.63 respectively, which is in good agreement with the results from *Toohey et al.* (2011) for the 17 Mt eruption and lower than their calculation for the 700 Mt case (global mean 2 years cumulative AOD of approximately 20-24 depending on season of eruptions in *Toohey et al.* (2011)). A tendency of winter eruptions to lead to smaller southern extratropical mean AOD than spring and summer eruptions is seen in Figure 3.2 (c). In the same way, winter hemisphere produce larger AOD in the northern hemisphere extratropics compared to other season (Figure 3.2 (b)). This agrees well with the results of *Toohey et al.* (2011).

3.5.2 Altitudinal distributions

For each eruption, our approach provides altitudinally resolved extinction values. Figure 3.3(a,c) shows the distribution of extinctions at 0.5 μm with altitude and time in the equatorial region for the Pinatubo (top) and Tambora eruptions (bottom). At this latitude, high extinctions values span approximately between 90 hPa and 15 hPa. One interesting behavior to point out is the fastest sedimentation of the aerosols in the case of the Tambora eruption compared to Pinatubo due to a more intense coagulation forming larger particles. In Figure 3.3(b,d), the cumulative monthly extinctions for the first two years after the eruptions are shown. The transport to the extra-tropics and polar regions follows the Brewer-Dobson circulation and is influenced by the gravitational settling of the particles. The region of

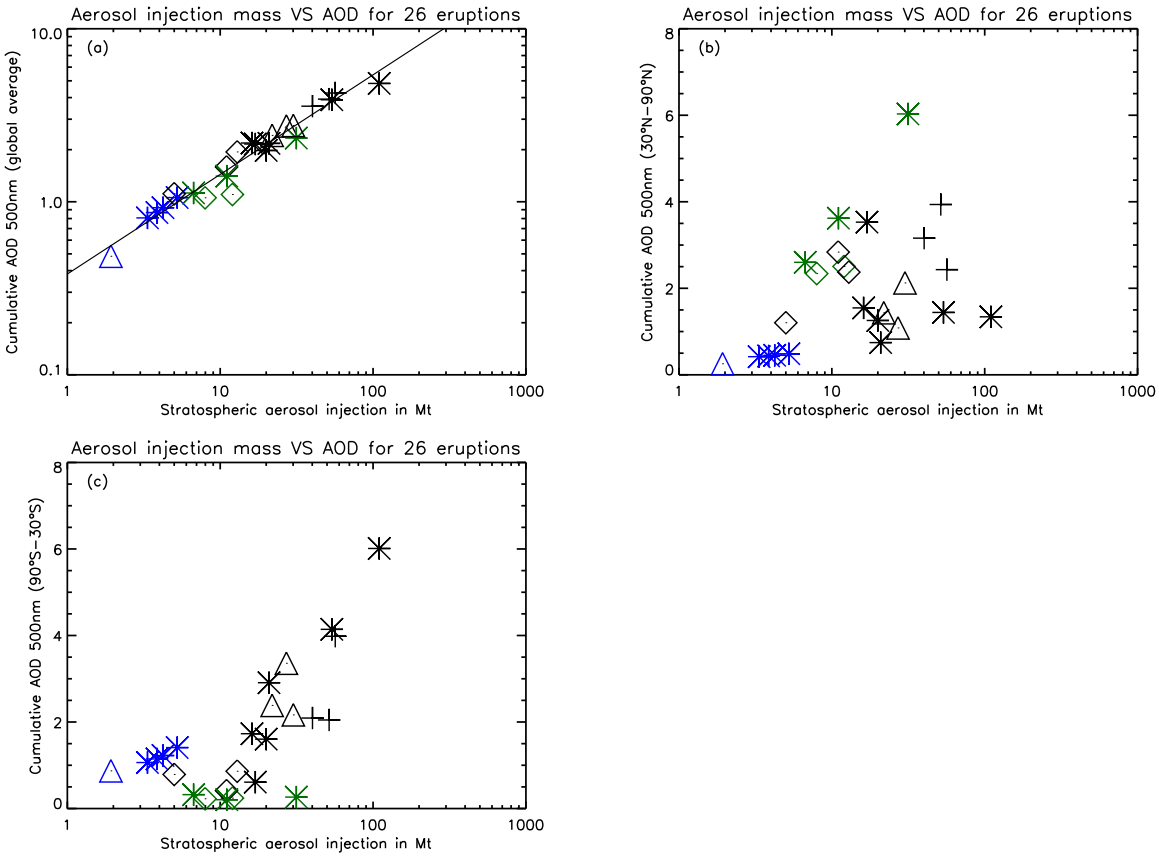

Fig. 3.2: Total mass of aerosol (H_2SO_4+H_20) in Mt versus 2 years cumulated AOD at 500nm for global average (a) , 30°N-90°N (b) and 90°S-30°S (c). Black line shows the logarithmic fit to the tropical eruptions. Stars indicate spring eruptions, triangles summer eruptions, diamonds fall eruptions and crosses winter eruptions. Black color indicates tropical eruptions, while blue and green colors indicate extratropical eruptions in the southern and northern hemispheres respectively.

high extinctions in the extra-tropics is in the 150-40 hPa range. The tropical pipe region is visible with strong extinction gradients at its limits.

The exact influence of the initial altitude distribution on the aerosol transport is still unclear. Using different SO_2 altitude injection does not change the aerosol distribution to a large extent, however some variations in the altitude distribution of the aerosol cloud in the first months following the eruption are observed. Also, while small differences of 1-2 km can theoretically influence the temporal and latitudinal evolution of the aerosols in the tropical reservoir, limitations in the model prevent a precise testing and analysis of this influence. Sensitivity studies made for the Tambora eruption with initial injection at 23-25 km and 27-29 km tend to indicate a small but non-negligible impact on the aerosol distribution, with shorter time residence in the tropical region for the 27-29 km simulation and stronger extra-tropical transport. Increasing the altitude injection from 24 km to 28 km hence decreases the mass peak loading by 10-15% in the tropics and increases it by 13% and 8% at 50°S and 50°N respectively (Arfeuille et al.,in prep).

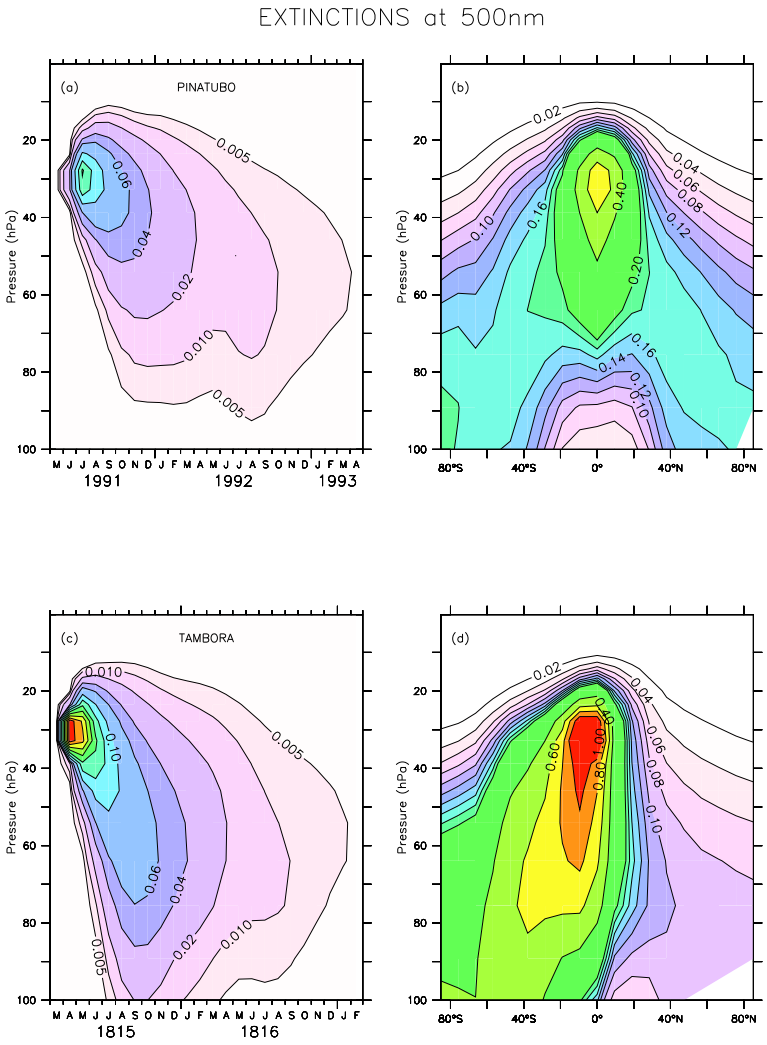

Fig. 3.3: Altitude distribution of the extinctions (1/km) in visible (550 nm) for the Pinatubo and Tambora eruptions for this study. Left panel shows equatorial (5°S-5°N) mean values, right panels show 2 years cumulative monthly extinctions.

3.5.3 Latitudinal distributions

The season and latitude of volcanic eruptions highly impact the latitudinal distribution of the volcanic aerosols especially through the hemispheric partitioning of tropical eruptions. In the tropics, aerosols first spread in the tropical pipe region (*Plumb*, 1996) where exchange to the extra-tropics is limited and varies seasonally. The transport to the extratropics is made preferentially towards the winter hemisphere as the increased meridional gradient leads to increased planetary wave propagation into the stratosphere (*Holton et al.*, 1995). Hence, in a first approximation, a spring-summer tropical eruption tends to produce high aerosol concentrations in the southern hemisphere. Additionally, the latitudinal position of the tropical pipe in the first weeks after the eruptions is also of strong importance as it influences the early latitudinal distribution of the aerosols inside the tropics. The latitudinal evolution of the most important eruptions are shown in Figure 3.4-3.7.

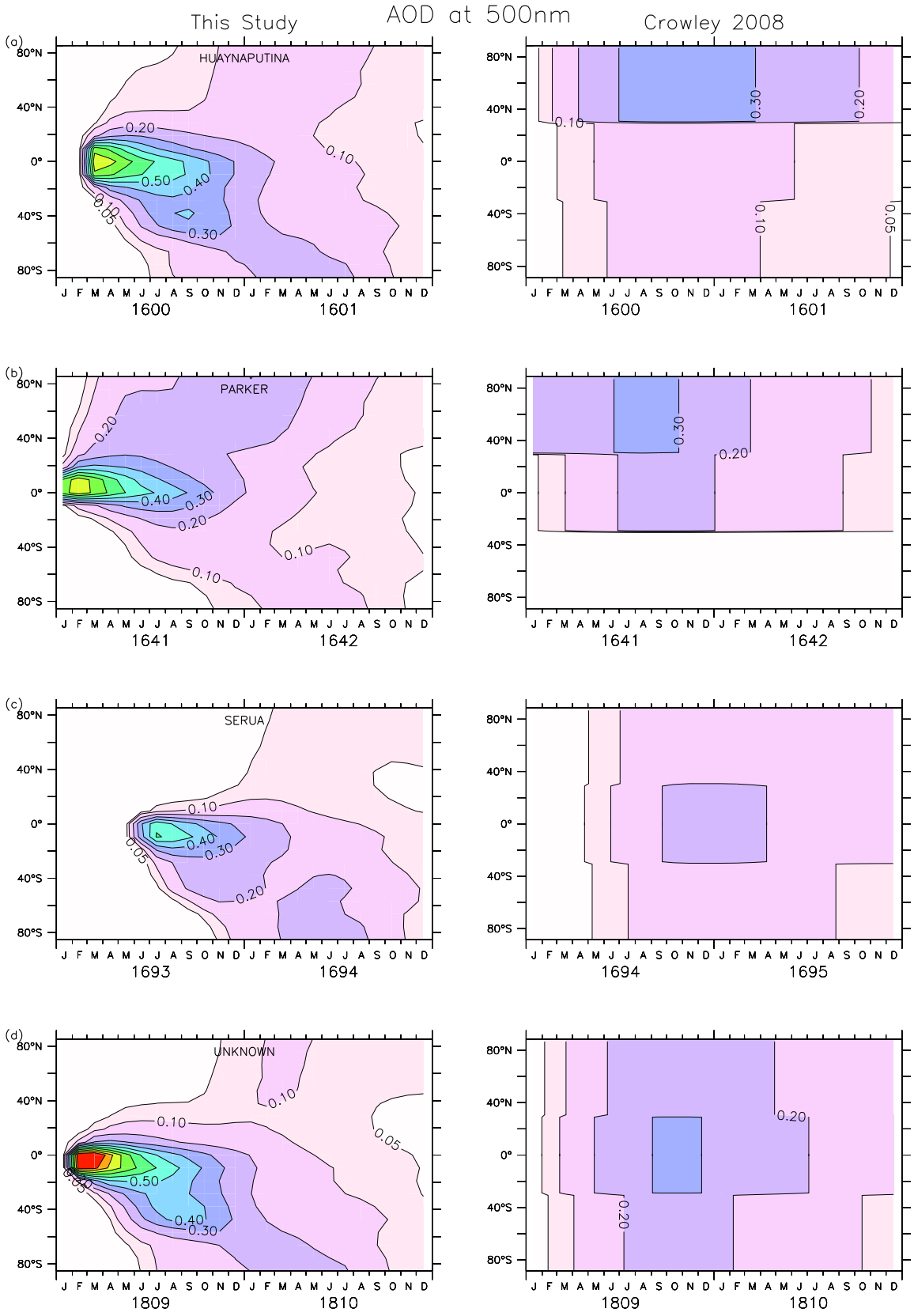

Fig. 3.4: Latitudinal distribution of the optical depth in VIS (550 nm) for several large eruptions for this study (left column) and *Crowley et al.* (2008) (right column)

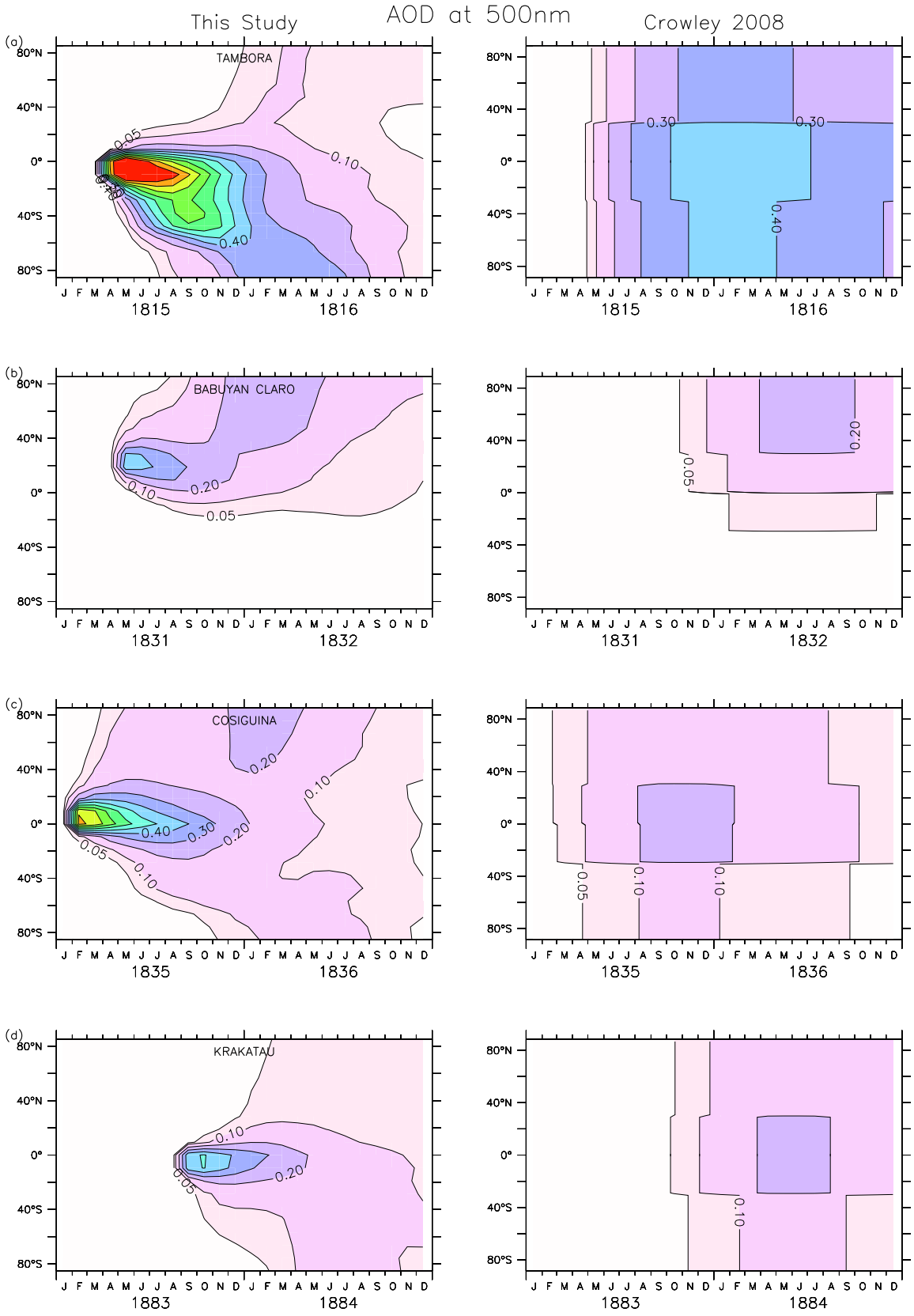

Fig. 3.5: Latitudinal distribution of the optical depth in VIS (550 nm) for several large eruptions for this study (left column) and *Crowley et al.* (2008) (right column)

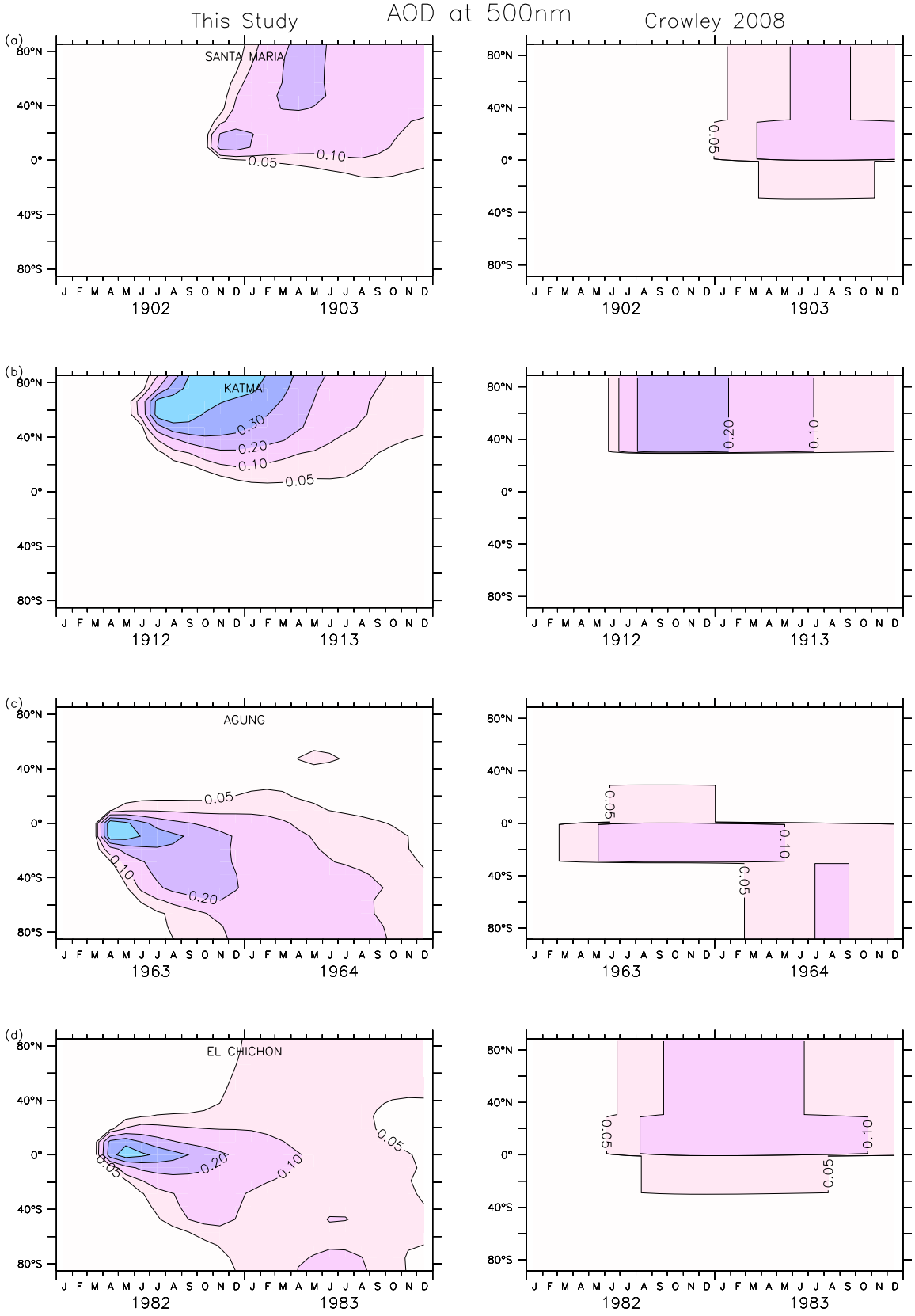

Fig. 3.6: Latitudinal distribution of the optical depth in VIS (550 nm) for several large eruptions for this study (left column) and *Crowley et al.* (2008) (right column).

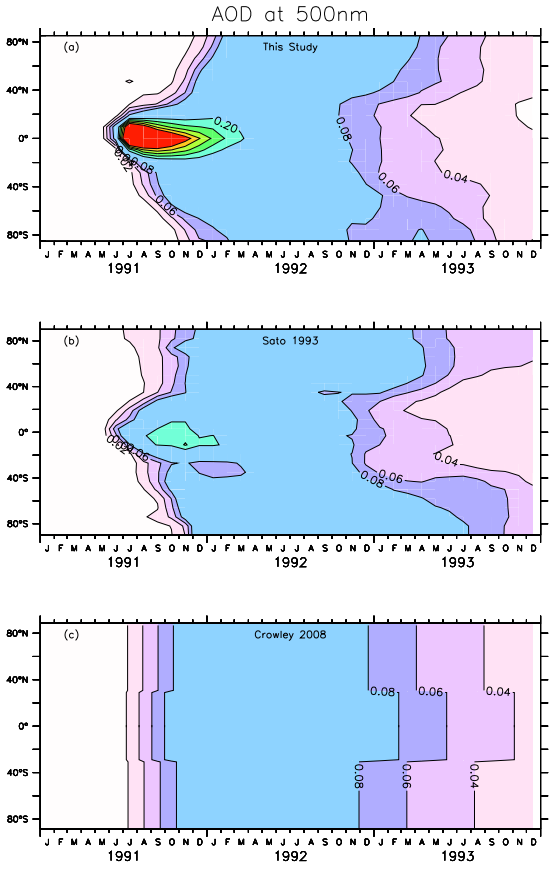

Fig. 3.7: Latitudinal distribution of the optical depth in VIS (550 nm) for the Pinatubo eruption for this study (top panel), *Sato et al.* (1993) (middle panel) and *Crowley et al.* (2008) (lower panel)

The specific hemispheric partitioning of the Tambora eruption is for instance illustrated in Figure 3.5, where the eruption which occurred in April 1815 produced an asymmetrical aerosol cloud in our model, with most of the mass in the southern hemisphere. The dataset from *Crowley et al.* (2008) also depict this behaviour for this eruption. The AOD distribution for the largest volcanic eruptions in the last 400 years present are shown in Figure 3.4 (Huaynaputina 1600, Parker 1641, Serua 1693, Unknown 1809),Figure 3.5 (Tambora 1815, Babuyan Claro 1831, Cosiguina 1835, Krakatau 1883), and Figure 3.6 (Santa Maria 1902, Katmai 1912, Agung 1963, El Chichón 1982) for our reconstruction and *Crowley et al.* (2008). From these 12 large volcanic eruptions, the El Chichón eruption, Krakatau, Unknown 1809, Serua and Huaynaputina eruptions show sizably different latitudinal evolution in the two datasets while the others eruptions show similar developments. It can also be noted that the different ice core parametrisations in *Gao et al.* (2008) lead to a different hemispheric partitioning than in *Crowley et al.* (2008) for Santa Maria, Serua and Tambora (Table 3.1).

A strong asymmetry was observed for the Agung March 1963 eruption by solar extinction measurements by *Stothers* (2001) as shown in Figure 3.10. The extent of the asymmetry is only captured in our dataset while *Ammann et al.* (2003) overestimates the northern hemisphere loading and *Sato et al.* (1993) and *Crowley et al.*

(2008) underestimate the southern hemisphere value.

The latitudinal evolution of the Pinatubo 1991 eruption is also well captured by our method. For this eruption, transient winds instead of a climatology was used. This reduces the equatorial optical depth after the eruption but does not sizably impact the hemispheric partitioning of the aerosols. Figure 3.7 shows a comparison of the time evolution of Mt. Pinatubo optical depth for this study and *Crowley et al.* (2008) compared to *Sato et al.* (1993) data derived from satellite observations. The hemispheric partitioning is reproduced correctly in both datasets. *Crowley et al.* (2008) tends to underestimate the peak optical depth in the tropics compared to *Sato et al.* (1993) while we overestimate it. However, *Sato et al.* (1993) underestimates the optical depth compared to AVHRR measurements in the equatorial region by up to a factor 2 (Figure 3.11). Our reconstruction still probably overestimate the AOD close to the equator. At northern mid-latitudes, our reconstruction, *Crowley et al.* (2008) and *Sato et al.* (1993) all show similar time evolutions, with only a limited underestimation of the AOD in early 1992 compared to AVHRR (Figure 3.11). Conversely, *Ammann et al.* (2003) tends to overestimate it, especially in the first six months after the eruption. Another feature well reproduced for Mt,Pinatubo eruption is the temporal evolution of the AOD in both tropics and extra-tropics compared to *Sato et al.* (1993) (Figure 3.7). *Crowley et al.* (2008) do not capture precisely the transport timing to extra-tropics, with too long time residence in the tropics and no time delay in the tropical to extra-tropical AOD. Their building of the AOD in the tropical region in June-August 1991 is too slow, with a time shift of approximately one month.

If the recent eruptions of Agung and Pinatubo are well reproduced, a bias towards the southern hemisphere is seen for the El Chichón eruption, where the observed higher loading in the northern hemisphere is not reproduced by the model. Figure 3.9 shows that both our reconstruction and *Ammann et al.* (2003) overestimate the southern hemisphere AOD compared to *Sato et al.* (1993).*Crowley et al.* (2008) which follows the *Sato et al.* (1993) data reproduce well the hemispheric partitioning of El Chichón (Figure 3.6).

Despite differences in the latitude and time distribution of the aerosols, global average AOD of our reconstruction show similar values as *Crowley et al.* (2008) for many past eruptions as shown in Figure 3.8. Some small eruptions in 17^{th} century and 19^{th} century are present in *Crowley et al.* (2008) but not in the *Gao et al.* (2008) ice core estimates and hence not in our dataset. Conversely, some small to medium eruptions in the 18^{th} century are not present in *Crowley et al.* (2008) or of a reduced magnitude.

From these results, we argue that the information on latitude and date of eruptions allows a satisfactory reproduction of the latitudinal evolution of the aerosols with the AER-2D model. Uncertainties due to the lack of information from the vertical wind structure in the tropics and QBO phases for historical eruptions is a limitation to get precise hemispheric partitionings in the past. However, ice core estimates do not always provide a robust partitioning between hemispheres. Peak values of AOD and its temporal evolution is generally well reproduced in our reconstruction when compared to *Sato et al.* (1993), *Stothers* (2001) and AVHRR although it overestimates the optical depth values in the equatorial region compared to AVHRR. Tropical mean AOD are generally higher than in *Sato et al.* (1993) and *Crowley et al.*

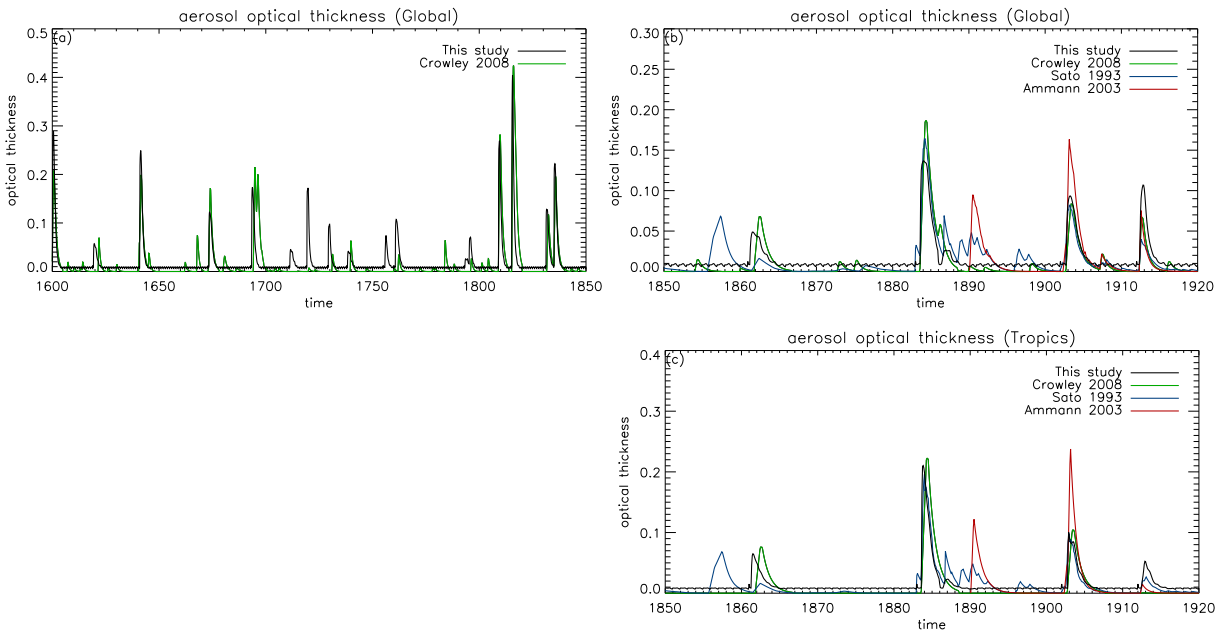

Fig. 3.8: Global mean total optical depth (AOD) in VIS (550 nm) for (a) 1600-1850 and (b) 1850-1995. Tropical mean AOD for 1850-1995 (c). Black line is the AOD from this study, green line is the AOD from *Crowley et al.* (2008), blue line is the AOD of *Sato et al.* (1993), red line is from *Ammann et al.* (2003).

(2008), and close to values from *Ammann et al.* (2003). *Ammann et al.* (2003) has the closest values to AVHRR measurements at the equator but with a too slow build up of the AOD at this latitude.

3.6 Final product

The released 1600-2011 volcanic aerosol dataset consists in monthly, two-dimensional fields of aerosol concentrations and sizes which can in turn be used to calculate exinctions, single scattering albedos and asymmetry factors for different wavelength bands. Surface area densities for heterogeneous chemistry are also made available. A volcanic aerosol spectral extinction dataset is also released for the MA-ECHAM5.4 model bands, T31L39 resolution (different radiative bands can be computed). This dataset contains surface area densities for chemical interactions and the following optical parameters for each of the 22 spectral bands: Extinction, single scattering albedo, asymmetry factor.

Eruptions:	Tambora	Agung	Krakatau	Pinatubo
HCl (Mt)	14-65	1.6	2.19-5.85	3
Strat.fract. (%)	1-10	1-10	1-10	1-10
Final HCl (Mt)	0.14-6.5	0.016-0.16	0.022-0.58	0.03-0.3

Table 3.3: Total chlorine released and potential final stratospheric loading for four large eruptions.

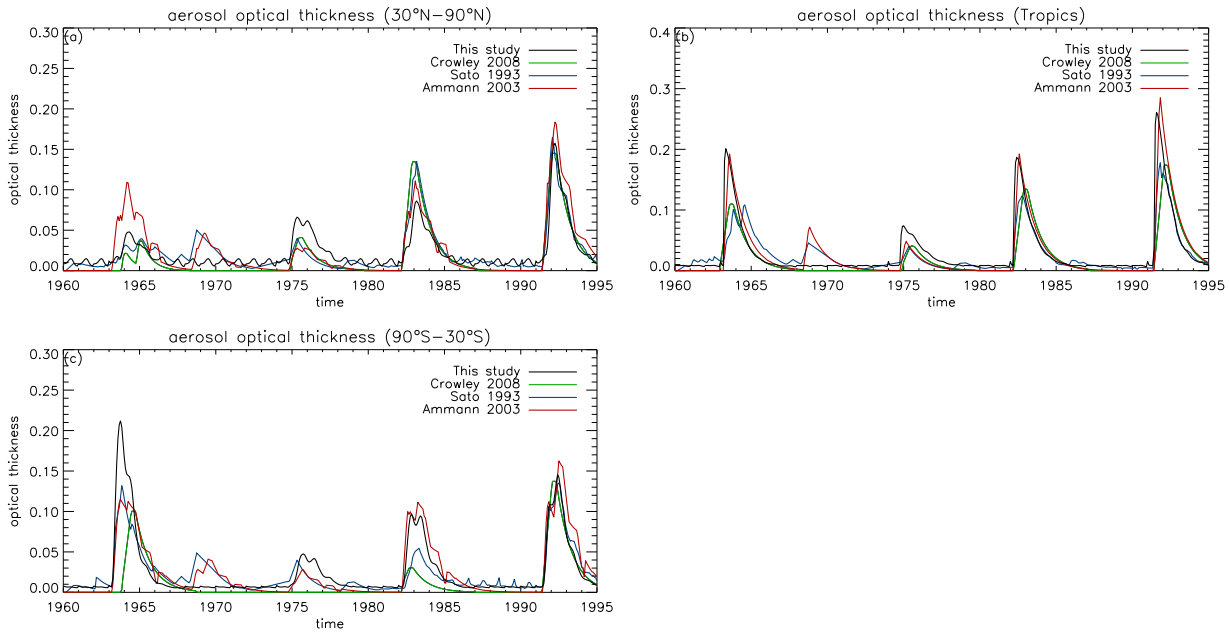

Fig. 3.9: Total optical depth (AOD) in VIS (550 nm) 1960-1995 for the northern hemisphere extra-tropics (a), tropics (b), and southern hemisphere extra-tropics (c). Black line is the AOD from this study, green line is the AOD from *Crowley et al.* (2008) , blue line is the AOD of *Sato et al.* (1993), red line is from *Ammann et al.* (2003).

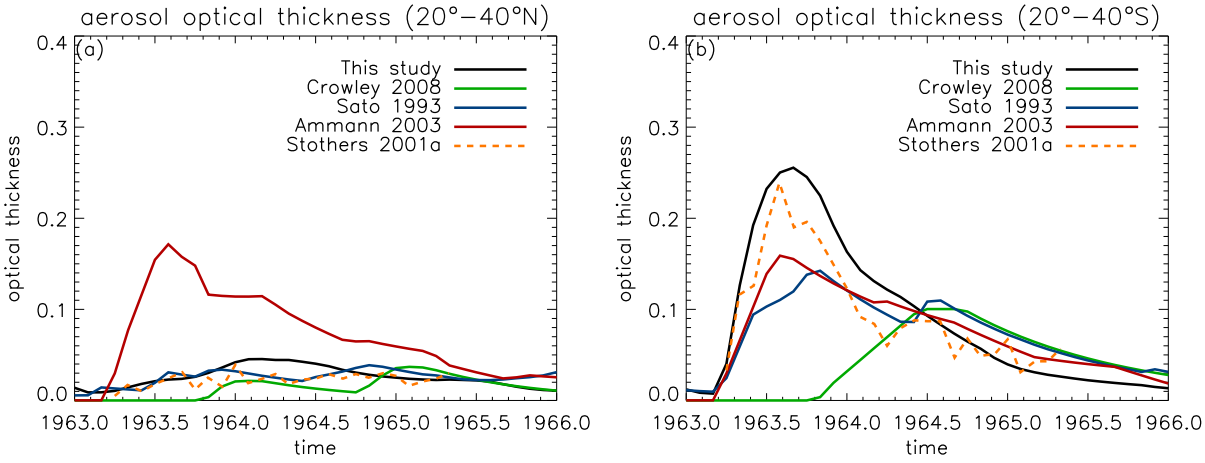

Fig. 3.10: Zonal mean total optical depth (AOD) in VIS (550 nm) for the Agung 1963 eruption for (a) 20°S–40°N and (b) 20°N–40°S.

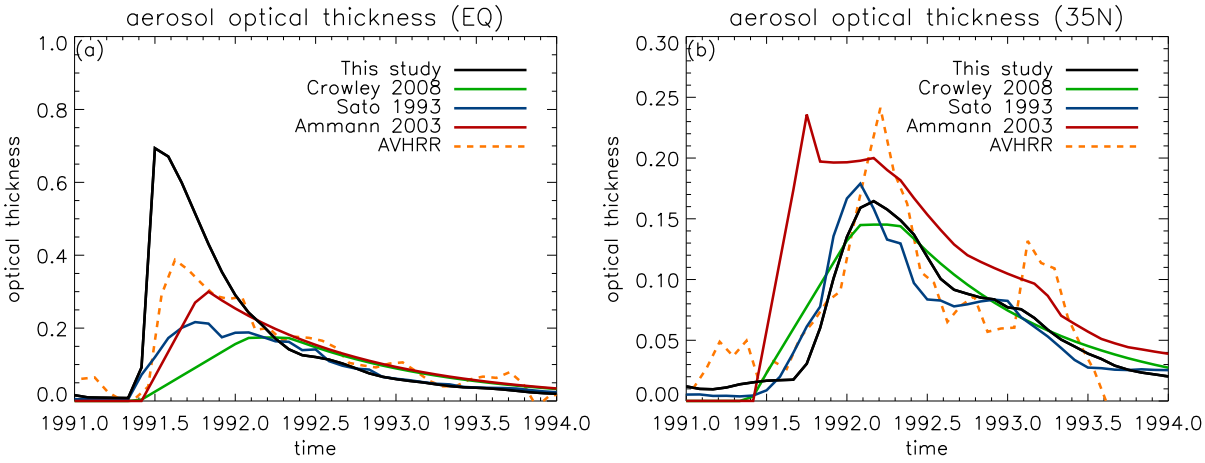

Fig. 3.11: Zonal mean total optical depth (AOD) in VIS (550 nm) for the Pinatubo 1991 eruption for (a) 5°S–5°S and (b) 30°N–40°N. AVHRR dataset is reduced from tropospheric extinctions.

3.7 Conclusions and Outlook

3.7.1 Conclusions

As emphasized by *Schmidt et al.* (2011), there is a need to account for the uncertainties in the various external forcings used in climate model simulations covering the last centuries in order to assess the extent of model deficiencies. The uncertainties in the volcanic forcing are still high due notably to lack of knowledge on the aerosol spatial and size distributions after large eruptions and this can lead to strong differences in the representation of both global and regional climatic anomalies in climate models.

In this study, the AER-2D aerosol model has been used to simulate volcanic eruptions in the 1600-2011 period. Results for the global mean 0.5 μm optical depth are in overall agreement with previous reconstructions from *Crowley et al.* (2008), *Ammann et al.* (2003) and *Sato et al.* (1993). However, large differences in hemispheric partitioning and tropical values as well as differences in detections of some historical eruptions in the different ice core datasets used are observed. AER-2D simulation of Pinatubo eruption showed an overestimation of the 0.5 μm optical depth satellite data from AVHRR in the equatorial region while previous reconstructions underestimate it. In the northern hemisphere mid-latitudes, reconstructions are in broad agreement. The Agung eruption hemispheric partitioning is better captured by our method than in previous reconstructions as shown by comparisons with solar extinction measurements from *Stothers* (1996). We argue that for known tropical eruptions, using informations on latitude and date of eruptions allows to represent the latitudinal evolution of the aerosols adequatly and provides a credible alternative approach to latitudinal parametrisation constrained by hemispheric calibration from ice cores. However errors in the hemispheric partitioning of aerosol mass for past eruptions probably remain due to the coarse resolution of the AER model and discrepancies in the climatological transport compared to actual wind fields. The latter includes a lack of the QBO and of the dynamical response to the radiative

perturbation of the aerosols.

This new volcanic forcing dataset provides extinction values as a function of latitude and altitude as simulated by the aerosol model, which accounts for climatological transport and sedimentation of the aerosols. This helps to refine the representation of the radiative, dynamical and chemical influence of the volcanic aerosols on climate compared to an optical depth forcing. The non-negligible longwave forcing of the aerosols which depend on the aerosol mass and size distribution is also described by the dataset. Similarly to 0.5 μm extinctions, comparisons with data available for the Pinatubo eruption show an overestimation of the extinction at 12 μm for the tropics for the first months after the eruption but a good agreement with ISAMS measurements later on (see Chapter 2). For the extratropics, results are in good agreement with ISAMS data.

3.7.2 Outlook

Further development could be applied to the volcanic aerosol dataset. The recent increase in the background stratospheric optical depth since 2004-2005 could be implemented. Either by increasing tropospheric SO_2 emissions or, as *Vernier et al.* (2011) and *Solomon et al.* (2011) argue that the recent increase is most likely due to small volcanic eruptions, by describing medium eruptions as Ruang (09/2002), Manam (01/2005), Montserrat (05/2006), Kasatochi (08/2008), Sarychev (06/2009) and Puyehue (06/2011). *Haywood et al.* (2010) estimate for instance that the Sarychev eruption released 1.2 MT of SO_2, *Carn et al.* (2009) estimates around 1.4 Tg SO_2 release for Kasatochi. Additionally, future scenarios of volcanic aerosols forcing can be computed using the methodology described here and following the statistical approach by *Ammann and Naveau* (2010). A preliminary analysis showed that the *Gao et al.* (2008) ice core data followed well a Pareto distribution. Another future implemention could also involve the description of stratospheric water vapor (*Joshi and Jones*, 2009), and halogens release. A modeling study on the volcanic plume dynamics and its implications for stratospheric release of halogens showed that up to 25% of the initial release may cross the tropopause (*Textor et al.*, 2003). However large uncertainties arise from the percentage of halogens reaching the stratosphere, which itself depends strongly on the humidity profile above the volcano and the dynamics of the plume. Table 3.3 shows illustrative stratospheric chlorine amounts for different large eruptions assuming a 1-10% stratospheric ratio from the initial volcanic release for these Indonesian and Philipinian volcanoes.

Acknowledgments. *The study was supported by the Cogito foundation, the Department of Environmental Science of ETH Zurich, EU-FP7 project "ERA-CLIM" and Swiss National Science Foundation project "FUPSOL".*

Chapter 4

Modelling the stratospheric response of the Tambora eruption (1815)

F. Arfeuille[1], E. Rozanov[1,2], D. Weisenstein[3], T. Peter[1], and S. Brönnimann[4]

[1] Institute for Atmospheric and Climate Science ETH Zurich, Zurich, Switzerland
[2] Physical-Meteorological Observatory/World Radiation Center, Davos, Switzerland
[3] AER, Lexington, Massachusetts, USA. (Now at Harvard University, Cambridge, MA, USA)
[4] Oeschger Center for Climate Change research and Institute of Geography, University of Bern, Bern, Switzerland

In preparation for publication in Atm. Chem. Phys.

Abstract
Strong volcanic eruptions in tropical regions have the potential to influence the Earth's climate for several years. The volcanic eruption of Mt. Tambora (Indonesia) in April 1815 is considered as the largest eruption within the past 700 years. It was likely the trigger of the famous "year without summer of 1816", but the mechanisms of the volcanic influence of this eruption are not yet fully clear. Here we analyze the stratospheric response to this large forcing. A combination of a two-dimensional aerosol model (AER-2D) and a three dimensional chemistry-climate model (SOCOL v2) was applied to assess the most important radiative, dynamical and chemical perturbations following the eruption. A number of sensitivity studies were performed addressing the roles of the amount and altitude distribution of the initial sulfure dioxide release, of interactive chemistry, and of sea-surface temperatures. The analysis confirms that the aerosol size distribution is a crucial parameter which strongly influences the radiative impact of the aerosols through the modification of their optical properties and of their residence time in the stratosphere. As the large amount of SO_2 released by the Tambora eruption in the tropical stratosphere leads to enhanced coagulation compared to the Pinatubo eruption, the larger aerosols have a weaker shortwave scattering impact and stronger longwave absorption impact than expected by a simple scaling. The shorter residence time of these large aerosols also leads to a radiative forcing comparable to a Pinatubo size eruption about 1.5 years after the eruption. Shortwave downward radiation is decreased by -9 W/m^2 at the surface in the 60°S-60°N region, while the longwave downward radiation is increased by 2.5 W/m^2. Ozone is globally increased by 17 DU as a consequence of NO_x decrease and low halogens concentration conditions. A strengthening of the northern hemisphere polar vortex in the first winter is also modelled.

4.1 Introduction

The climatic effects of a large stratospheric aerosol forcing are not yet fully understood. This would be important, however, for assessing climatic effects of past volcanic eruptions, for seasonal forecasting of climate (should an eruption occur), or as an analogue for suggested climate engineering approaches such as the artificial release of sulfur aerosols to the stratosphere to counteract greenhouse warming (*Crutzen*, 2006). The difficulty of understanding the effects of a stratospheric aerosol forcing relates to the fact that radiative, microphysical, chemical, and dynamical factors act together. Being able to accurately represent these effects in a model framework thus would contribute to a better understanding of the role of stratospheric processes in climate. Many previous studies (*Vupputuri*, 1992; *Shindell et al.*, 2004; *Stenchikov et al.*, 2009) have targeted the Tambora eruption (Sumbawa island, Indonesia) of April 1815 which led to anomalous temperatures and precipitations in many regions of the globe and led to a substantial global (*Briffa and Jones*, 1992) and regional cooling (*Trigo et al.*, 2009; *Auchmann et al.*, 2011). In this study we address the effects of this eruption on the stratosphere in a model framework.

The Tambora eruption released around 60 Mt of SO_2 into the stratosphere (*Gao et al.*, 2008). This is the largest eruption in the last 700 years together with the Kuwae (1452) eruption. The sulfur dioxide amount released corresponds to 3-4 times

the quantity of the 1991 Pinatubo eruption. After formation of sulfuric aerosols, this likely led to a strong stratospheric forcing, with important radiative, chemical and dynamical impacts. For such a large eruption, specificities in aerosol microphysics have to be taken into account to estimate the absorption of longwave radiation and the scattering of shortwave radiation quantitatively. Specifically, the aerosol size distribution strongly influences optical and chemical properties of aerosols as well as their residence time in the stratosphere and thus their radiative, dynamical, and chemical impacts.

In this study we model the stratospheric response to the Tambora eruption using a chain of numerical models capable of representing the relevant processes from the volcanic eruption to the stratospheric impacts. A combination of a two dimensional aerosol model (AER-2D) and a three dimensional Chemistry-Climate model (SOCOL v.2) is used to assess the global radiative and chemical perturbation of the eruption. This gives an opportunity to test our understanding of the mechanisms of volcanic eruption impacts on climate and our ability to reproduce them numerically.

The focus of this study is on the radiative, chemical and dynamical changes in the stratosphere induced by the Tambora volcanic aerosols. It includes a range of sensitivity experiments as well as comparisons with studies of Pinatubo and with idealized model experiments. The response of tropospheric climate and the comparison with observations, climate proxies, and reconstructions is outside the scope of this paper and will be addressed in a subsequent article.

4.2 Volcanic boundary conditions

4.2.1 SO_2 mass estimates

Gao et al. (2008) used 54 ice cores records from the Arctic and Antarctic to reconstruct the volcanic forcing of the past 1500 years through the extraction of volcanic deposition signals by applying a high-pass loess filter to the time series. 32 of the 36 new ice cores analyzed by *Gao et al.* (2008) cover the Tambora eruption. Results in terms of stratospheric aerosol loadings vary from 117 Tg to 129 Tg depending on the extraction criteria used. The conversion from aerosol loadings to released amounts of SO_2 is given by:

$$m_{SO_2} = m_{aero} \times wt\%_{H_2SO_4} \times \frac{M_{SO_2}}{M_{H_2SO_4}} \text{ , with :} \tag{4.1}$$

$$m_{aero} = F_{aero_{HN}} \times Cal_{HN} + F_{aero_{HS}} \times Cal_{HS}. \tag{4.2}$$

The individual terms of the equation are given in Table 4.1.

Assuming an average aerosol composition of 75 wt% of H_2SO_4, this leads to an estimated mass release of SO_2 of 58.5-64.5 Tg, which is around three to four times higher than the estimated amount of SO_2 released from the Pinatubo eruption in 1991 (17-20 Mt, Thomason and Peter, 2006).

Due to the strength of the eruption which released a large amount of SO_2, the ice core method gives an especially narrow error range from the choice of extraction method

due to a better signal to noise ratio. However, issues due to the separate calibration of Greenland (by nuclear bomb test deposits) and Antarctica (Pinatubo eruption) lead to large uncertainties in the estimation of the hemispheric partitioning.

Another approach to calculate the SO_2 release of volcanic eruption is the petrological method, based on the analysis of the average sulfur concentrations of the inclusion and matrix glasses. Knowing the mass of erupted magma and the mass fractions of crystals in the magma, the total amount of released sulfur can be estimated. Using estimates of the mass flux from the Mt. Tambora eruption provided by *Self et al.* (2004), the amount of released SO_2 is estimated to 53-58 Tg. These values are close to the estimates received by the ice core method described above, which gives confidence in the relative accuracy of the estimates. One limitation of this method is the potential inhomogeneity of the sulfur concentration in the magma.

To account for the uncertainties in the SO_2 mass estimates, two different scenarios were simulated with the AER-2D model: a best guess scenario with 60 Mt of SO_2 and a large emission scenario with 80 Mt of SO_2.

Table 4.1: Parameters for a 108 Tg aerosol estimate from Gao et al 2007

Parameter	Value	description
$F_{aero_{HN}}$	58 kg/km^2	sulfate concentration in Greenland ice cores
Cal_{HN}	1×10^9km^2	calibration factor for NH based on nuclear bomb tests
$F_{aero_{HS}}$	51 kg/km^2	sulfate concentration in Antarctica ice cores
Cal_{HS}	1×10^9km^2	calibration factor for NH based on Pinatubo observations
$wt\%_{H_2SO_4}$	75%	Mean H_2SO_4 weight% in aerosols
M_{SO_2}	64	SO_2 molar mass
$M_{H_2SO_4}$	98	H_2SO_4 molar mass

4.2.2 Altitude distribution

In a recent study (*Herzog and Graf*, 2010) it has been shown that 1D models are able to reproduce the maximum height of the eruptive column reasonably well, but not the actual height of the spreading of the SO_2 cloud. Differences between the maximum height of the eruption (including the overshooting above the level of neutral buoyancy due to residual velocity) and the altitude of the aerosol spreading is around 5-10 km (*Herzog and Graf*, 2010). For our study, we calculated the altitude of injection with the Plumeria model (*Mastin et al.*, 2009) using estimates of the mass release rate from (*Self et al.*, 2004). The calculated maximum height ranges between 30.5 km and 36.5 km, while the level of neutral buoyancy is estimated to range between 23 km and 26.5 km. In our study we accounted for these uncertainties by performing a sensitivity study injecting 60 Mt of SO_2 in the 27-29 km layers instead of the common volcanic altitude of 23-25 km. Both values are significantly lower than estimates of *Sigurdsson and Carey* (1989), who stated a Plinian eruption column height of 43 km. This estimate is based on a relationship between ash deposits thickness from different distances from the vent and the altitude of the cloud. Additionally, it should be noted that the Tambora eruption involved a co-ignimbrite

phase which potentially led to the release of SO_2 at lower levels (*Herzog and Graf*, 2010).

4.2.3 Chlorine

The total release of chlorine from the Mt. Tambora eruption was initially estimated by *Devine et al.* (1984) based on estimates of the magma release. However in that study, the assummed magma release was overestimated in comparison to more recent estimates by *Self et al.* (2004). This leads to an overestimation of the HCl emissions. Using the formula of *Self et al.* (2004) and applying it to chlorine, we can estimate the initial total chlorine release:

$$\mathrm{E}_{Cl} = \frac{(2M_v(1 - Wxls)(Cglass - Cmatrix))}{100}. \tag{4.3}$$

Using:

Variable	Value
Mv	7.4-8.1$\times 10^{13}$ kg
$Wxls$	0. 1 (10%)

E(cl) is the emission of chlorine (kg), Mv the mass of erupted magma (kg), W(xls) is the mass fraction of crystals in the magma, C represents the chlorine concentration. Based on the estimated magma release provided by *Self et al.* (2004) we calculate a total chlorine emission of 14 Mt, while the magma release estimates by *Devine et al.* (1984) lead to chlorine emissions of approximately 65 Mt. These two estimates are derived from different measurements in melt inclusions and matrix glass and are the only two available in the literature. This illustrates the large uncertainties associated with the total amount of chlorine released from the Mt. Tambora eruption. The stratospheric injection is estimated to range between 1% to more than 25% of the total emissions (*Textor et al.*, 2003), resulting in a high uncertainty range for the chlorine burden of 0.1-15 Mt. In comparison, in the 1980s approximately 1 Mt of chlorine from chlorofluorocarbon emissions reached the stratosphere per year. The percentage of chlorine reaching the stratosphere mainly depends on the humidity of the atmosphere above the volcano and on the amount of water vapor released by the volcanic eruption.

Since relative humidity over Indonesia in April is always high and Tambora itself released a large amount of water vapor (*Joshi and Jones*, 2009), it is unlikely that very large amounts of chlorine reached the stratosphere. Hence we use pre-industrial background values of stratospheric chlorine in this study.

4.3 Model description and experimental set-up

4.3.1 The sulfate aerosol model AER

The two-dimensional sulfate aerosol model developed at AER (Atmospheric and Environmental Research Incorporation, Lexington, USA) is used to model the strato-

spheric aerosol distribution following the eruption of Mt. Tambora. For general validation of the AER-2D model against observations see e.g. *Weisenstein et al.* (1997, 2007). The model includes the following sulfur species: SO_2, OCS, DMS, H_2S, and CS_2. Thereby SO_2 and OCS are the major gas species in terms of sulfur input into the stratosphere. For the Mt. Tambora eruption the sulfur is brought into the stratosphere in the form of SO_2. The model uses pre-calculated photolysis rates, derived from a model calculation with standard stratospheric chemistry (Weisenstein et al., 1997). Reaction rates are according to Sander et al. (2000). In the present study OH climatologies are adapted from von Kuhlmann et al. (2003). Sulfuric acid aerosols (H_2SO_4/H_2O) are calculated on the global domain from the surface up to 60 km with a vertical resolution of 1.2 km. The horizontal resolution is 9.5°. The model accounts for significant recycling of gaseous H_2SO_4 into SO_x in the upper stratosphere via photolysis. The sulfate aerosols are treated as liquid binary solution droplets (or ternary solution droplets in polar regions). Their exact composition is directly derived from the surrounding temperature and humidity. The AER 2D-model considers 40 size bins covering the range from 0.4 nm up to 3.2 μm. The size distribution of the aerosol particles is determined by micro-physical processes as nucleation, condensation, evaporation, coagulation, sedimentation and tropospheric washout.

Resolving the size distribution of aerosol particles is crucial for predicting the correct sedimentation rate and hence the lifetime of stratospheric particles. In the AER model aerosol particles are formed via homogeneous nucleation. Nucleation theories and experimental observations often differ by several orders of magnitude, but the resulting uncertainty does generally not represent a problem because coagulation readily adjusts number densities when nucleation rates are large (*Weisenstein et al.*, 2007). Transport parameters are based on *Fleming et al.* (1999) and are calculated from observed ozone, water vapor, zonal wind, and temperature distributions for climatological as well as transient conditions. Wave driving by planetary and gravity waves is also included.

4.3.2 The Chemistry-Climate Model SOCOL

The chemistry-climate model (CCM) SOCOL (SOlar Climate Ozone Links) was developed within a collaboration of ETH Zurich, PMOD/WRC (Physical and Meteorological Observatory / World Radiation Center) Davos and MPI Hamburg. The dynamical and radiative part of the model consists of the spectral general circulation model (GCM) MA-ECHAM4 (Middle Atmosphere version of the European Center/Hamburg Model 4) (*Manzini and McFarlane*, 1998). The chemistry is based on a modified version of the UIUC (University of Illinois at Urbana-Champaign) chemistry-transport model (CTM) MEZON (Model for the Evaluation of oZONe trends) (*Rozanov et al.*, 1999, 2001; *Egorova et al.*, 2001, 2003).

The present study is based on the second generation of the SOCOL model. A detailed model description can be found in *Schraner et al.* (2008). SOCOL is used in a spectral horizontal resolution of T30, resulting in a corresponding Gaussian transform grid size of approximately 3.75°x3.75°. Chemistry, radiation and all physical parameterizations are calculated in grid space. In the vertical the atmosphere is

represented by 39 model levels up to the top layer at 0.01 hPa (about 80 km), resulting in a vertical resolution of 0.1-1.5 km in the troposphere, 1.5-2.5 km in the stratosphere and 3-9 km in the mesosphere. For dynamical processes and physical parameterizations a time step of 15 min is used. Radiative transfer and chemistry calculations are performed every two hours.

The radiation scheme of MA-ECHAM4 is originally based on ECMWF radiation code (*Fouquart and Bonnel*, 1980; *Morcrette*, 1991). The radiation code considers 8 spectral bands: one band in the shortwave and visible, one band in NIR and 6 bands in the longwave part of the spectrum. The chemical part of SOCOL considers 41 chemical species, 118 gas-phase reactions, 33 photolysis reactions and 16 heterogeneous reactions on/in aerosol and polar stratospheric cloud (PSC) particles. The delta eddington approximation is not suitable in the case of a large volcanic eruption such as the one of Tambora in 1815 and hence was not applied.

4.3.3 Experimental set-up

Using the above-described model tools, simulations (Table 4.2) have been performed with the AER-2D model taking into account different amounts of SO_2 released into the atmosphere, (60 Mt and 80 Mt), different altitudes of the volcanic SO_2 injection, and an initial latitudinal distribution shifted to the north for the Pinatubo eruption simulation. Additionally a simulation with interactive chemistry was carried out for the 80 Mt scenario to examine the impact of the OH distribution on the formation of H_2SO_4 within the Stockwell-Calvert reaction cycle (80_int):

$$SO_2 + OH + M \rightarrow HSO_3 + M \tag{4.4}$$

$$HSO_3 + O_2 \rightarrow SO_3 + HO_2 \tag{4.5}$$

$$SO_3 + H_2O + M \rightarrow H_2SO_4 + M \tag{4.6}$$

In each model experiment the date of the volcanic eruption was set to the 10^{th} of April 1815, except for the Pinatubo simulation where it was set to June 15^{th}. The released amount of SO_2 was evenly spread over the latitudinal bands 9.5°S-9.5°N assuming a rapid zonal transport of the released volcanic SO_2 from the eruption within the tropics.

SOCOL simulations (Table 4.3) have then been performed using the different AER-2D results and boundary conditions for the 1815 period (Low solar irradiance, pre-anthropogenic greenhouse gases concentrations, low CFC conditions). Results here are shown for the SOCOL simulations using the 60M2325 and the Pin scenario. Two sets of sea surface temperature data, which are prescribed in SOCOLv2, were used. The first set used is a climatological mean of the 1886-1915 period, excluding strong ENSO years and years following large eruptions (Scenario Tamb.clim.SST), the second, a reconstruction by *Mann et al.* (2009) (Scenario Tamb.Rec.SST). Two control scenarios using the two SST boundary conditions were also performed with background aerosol concentration. Simulations were launched after a spin-up of 5 years and are here analyzed for the period of the strong stratospheric perturbation during the 1815-1816 period. Each scenario consists of three ensemble members.

Table 4.2: Sensitivity simulations (AER)

Experiment	SO_2 (Mt)	Latitude	Altitude (km)	AER interactive chem
60M2325	60	9.5°S-9.5°N	23-25	No
60M2729	60	9.5°S-9.5°N	27-29	No
80M	80	9.5°S-9.5°N	23-25	No
$80M_{int}$	80	9.5°S-9.5°N	23-25	Yes
Pin	20	5°S-15°N	23-25	No
CTRL	0	/	/	/
Idealized-5MT	5	9.5°S-9.5°N	23-25	No
Idealized-10MT	10	9.5°S-9.5°N	23-25	No
Idealized-20MT	20	9.5°S-9.5°N	23-25	No
Idealized-60MT	60	9.5°S-9.5°N	23-25	No
Idealized-200MT	200	9.5°S-9.5°N	23-25	No

Table 4.3: Sensitivity simulations (SOCOL)

Experiment	AER forcing	SST	Start-end	Ensemble
Tamb.clim.SST	60M2325	Clim.1886-1915	1814-1817	3 members
Tamb.rec.SST	60M2325	Mann et al.,(2009)	1814-1817	3 members
Pin	Pin	HadCRUT3	1990-1993	3 members
$CTRL_{clim}$	CTRL	Clim.1886-1915	1814-1817	3 members
$CTRL_{rec}$	CTRL	*Mann et al.* (2009)	1814-1817	3 members
Idealized-5MT	Idealized-5MT	Clim.1886-1915	1814-1817	No
Idealized-10MT	Idealized-5MT	Clim.1886-1915	1814-1817	No
Idealized-20MT	Idealized-5MT	Clim.1886-1915	1814-1817	No
Idealized-60MT	Idealized-5MT	Clim.1886-1915	1814-1817	No
Idealized-200MT	Idealized-5MT	Clim.1886-1915	1814-1817	No

4.4 Results

4.4.1 AER simulations

4.4.1.1 Transport

Figure 4.1(a) exhibits the amount of sulfur in the condensed phase for three different experiments. As a first approximation, the altitude of the initial SO_2 cloud does not highly influence this amount as evidences by the small differences between the 60M2325 and 60M2729 experiments.

As mentioned in section 4.2.1, the calibration of the sulfate deposits in ice cores in *Gao et al.* (2008) was made independently for Greenland and Antarctic. They found an almost equal distribution of aerosol mass to both hemispheres. However, in model experiments with the GCM ModelE they found that 65% of the transport is made to the SH for the Tambora eruption, which is close to our results. In our experiments, the maximum in sulfur contained in the aerosol reaches 19.5 MT in the southern

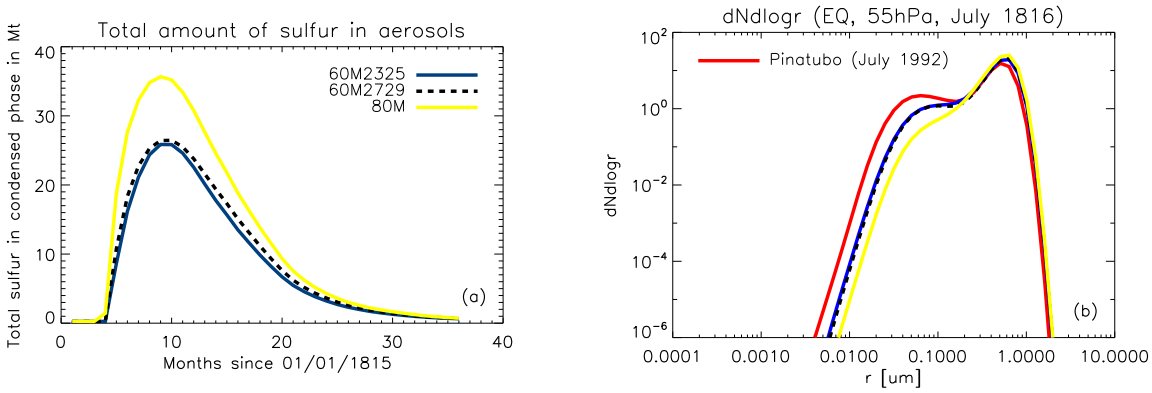

Fig. 4.1: Evolution of the total amount of sulfur in the condensed phase in Mt for three scenarios (a), and size distribution of stratospheric aerosols at the equator 55 hPa altitude for July 1816 (Pinatubo simulation result in July 1992 shown for comparison) (b).

hemisphere and 8.2 MT in the northern hemisphere for the 60M2325 experiments. This corresponds to a 70% to 30% ratio towards the southern hemisphere.

This asymmetry arises from the specific timing of the eruption in mid-April. Indeed the strong Brewer Dobson circulation to the winter hemisphere in the first few months transport quickly the SO_2 and recently formed aerosols to the SH. Observations from the Agung eruption of March 1963 also indicate a 2/3 transport to the SH.

4.4.1.2 Size distributions

The size distribution in volcanically perturbed periods can be described by two juxtaposed log-normal distributions (*Deshler et al.*, 2003) A lognormal size distribution is described by the total number of particles (N_0), the mode radius (r_m) and the width of the distribution (standard deviation σ):

$$\frac{\mathrm{d}N(r)}{\mathrm{d}r} = N_0 \frac{e^{-\frac{1}{2}\left[\frac{\ln^2(r/r_m)}{\ln^2\sigma}\right]}}{\sqrt{2\pi} r \ln^2\sigma}, \tag{4.7}$$

With $N(r)$ representing the number concentration of particles with the radius r.

In Figure 4.1(b) the size distributions of the volcanic aerosols 15 months after the Tambora and Pinatubo eruptions are shown at the Equator (55 hPa) as calculated by the AER-2D model. A shift to larger radiuses is observed after the Tambora eruption compared to the simulated aerosol distribution of Pinatubo. This can be explained by an higher concentration of SO_2 in the stratosphere leading to stronger coagulation of the aerosols.

4.4.1.3 Extinctions

Figure 4.2 shows the evolution of the extinction at 1.02 μm for the equatorial region at 20 km. A Pinatubo 20 Mt scenario is compared with the two Tambora simulations 80M and 80M_int. The extinction peak for the Tambora simulation

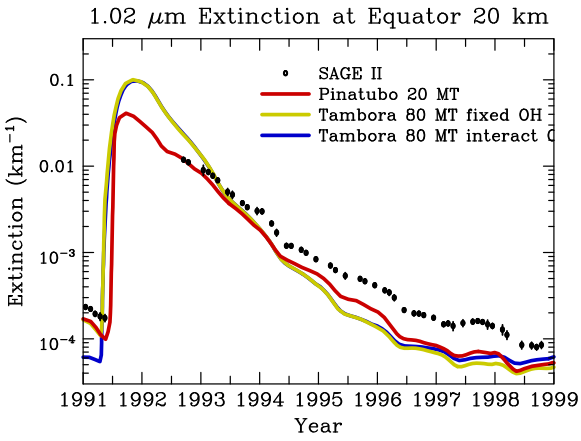

Fig. 4.2: Extinction at 1.02um at Equator / 20km altitude for two Tambora 80 Mt scenarios with and without interactive chemistry, and for a Pinatubo 20 Mt scenario. SAGE II 1991-1999 extinction is given for comparison.

reaches 0.1/km^{-1} while the Pinatubo extinction peaks at 0.04/km^{-1}. However, the extinction decrease is much faster in the Tambora simulations, illustrating the fast sedimentation of large aerosols. Two years after the eruption, extinctions are comparable in the equatorial lower stratosphere, but underestimate SAGE observations.

4.4.1.4 OH limitation

The 80M_int experiment allows addressing the impacts of an interactive depletion of OH while H_2SO_4 forms. Indeed, with intense formation of aerosols, the possibility of a OH limitation arises. However our simulation suggest that even for the high SO_2 release estimate of Mt.Tambora eruption, this has not an important impact, with no delay in the aerosol formation due to a limitation in OH availability (Figure 4.2).

4.4.1.5 Surface area density

The surface area density parameter is important to assess the chemical response to the eruption as heterogeneous reactions occur on stratospheric aerosols surfaces. Figure 4.3 show the SAD distribution for different scenarios. The surface area density of the 60M2325 experiment reaches about 100 $\mu m^2/cm^3$ in the tropical lower stratosphere in October 1815. The 60M2729 simulation leads to a decrease of up to 20 $\mu m^2/cm^3$ around 20 km, and increases the surface area density above 25 km. Using a 80 Mt emission, the SAD increase in the 15-25 km altitude range by up to 20 $\mu m^2/cm^3$.

4.4.2 SOCOL simulations

4.4.2.1 Radiative perturbation

The shortwave radiation decrease following the Tambora eruption reaches -9 W/m^2 globally (60°S-60°N) and -20 W/m^2 in the tropics (20°S-20°N) at the surface (Figure 4.4). The influence of the sea surface temperature difference between the re-

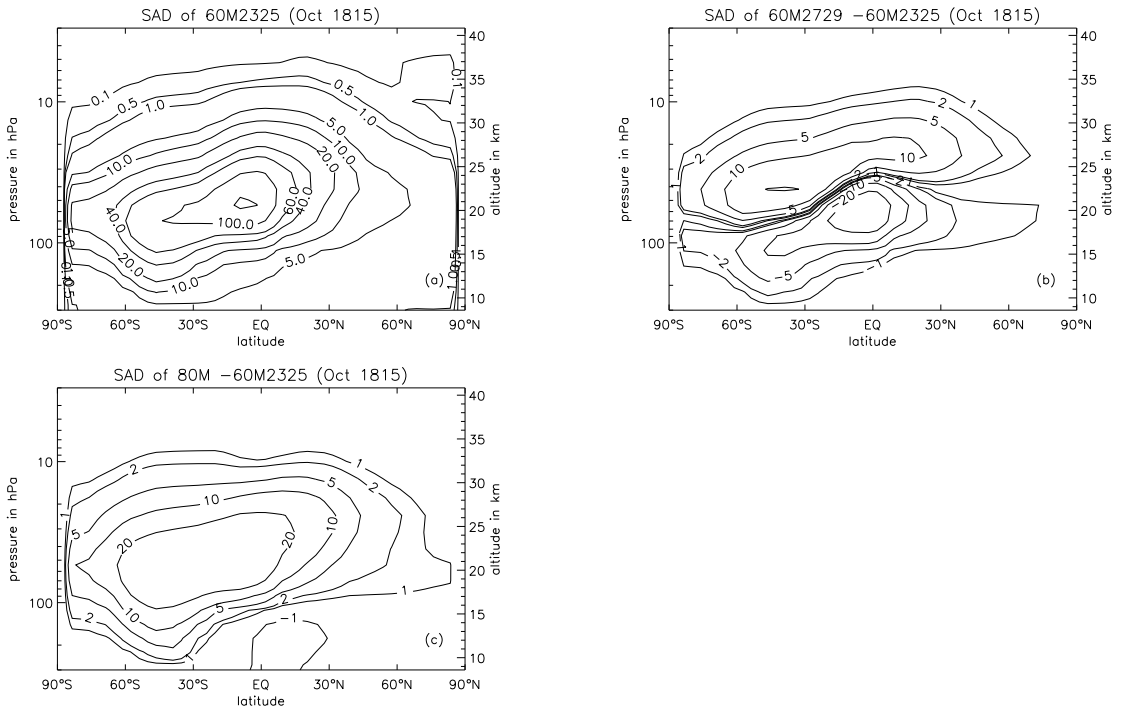

Fig. 4.3: Surface area densities in $\mu m^2/cm^3$ for scenario with 60M2325 (a), and anomalies from the 80M and 60M2729 scnarios to the 60M2325 experiment (b,c).

constructed values from *Mann et al.* (2009) (Tamb.Rec.) and a 1886-1905 climatology (Tamb.clim.) is negligible. In comparison, the simulation carried out for the Pinatubo eruption exhibits values of -4 W/m^2 and -10 W/m^2 for the 60°S-60°N and tropical averages respectively. A simple scaling of the Pinatubo (20 Mt) simulation by a factor 3 to account for the smaller SO_2 mass released compared to the Tambora eruption (60 Mt) hence shows the non-linearity of the shortwave forcing due to larger particles (see Figure 4.1(b)). Conversely, the longwave forcing from the Tambora eruption corresponds approximately to 3 times the one of our Pinatubo simulation (Figure 4.4), as absorption in the infrared by stratospheric aerosols is a function of the aerosol volume. In the tropics, the longwave forcing for the Tambora aerosols reaches 5 W/m^2 in late 1815 (Figure 4.4(b)). The radiation perturbation after the Tambora eruption fades quicker than for Pinatubo because of the faster sedimentation of the larger, heavier, stratospheric aerosols. On a global average, forcings from the Tambora and Pinatubo eruptions are comparable 1.5 year after the eruptions (Figure 4.4(a)), and less than a year after for the tropics (Figure 4.4(b)). The latitudinal distributions of the shortwave and longwave net anomalies in clear sky conditions (Figure 4.5) show the asymmetrical forcing at the surface by the stratospheric aerosols. The distributions of the total (shortwave+longwave) net radiation in clear sky conditions for the 1815 and 1816 annual means (Figure 4.5) exhibits the net decrease in energy at the surface after the eruption and the spatial dispersion of it.

As a consequence of the absorption of the infrared radiation by the volcanic aerosols, the stratospheric temperatures increase after the eruption. In the tropics at 40 hPa, the Tambora simulations exhibit a large warming of up to 14 K after the eruption (Figure 4.6(a)). This is twice the impact of the Pinatubo eruption in our simulation,

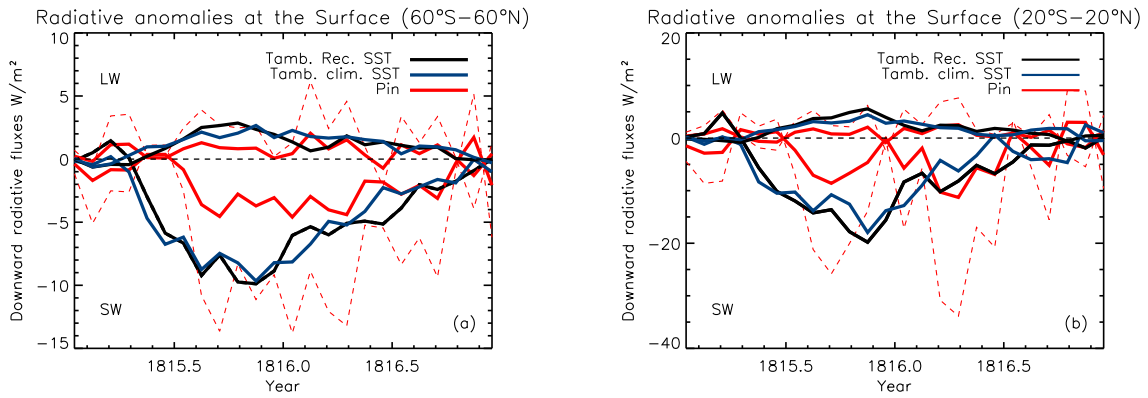

Fig. 4.4: Globally (60°S-60°N) averaged SW and LW radiative flux anomaly at the surface for three different scenarios. Pin corresponds to a Pinatubo simulation of 20 Mt SO_2 release. Anomalies are computed compared to a reference simulation. Ensemble means are displayed. Dashed red lines correspond to the Pin scenario scaled by a factor 3.

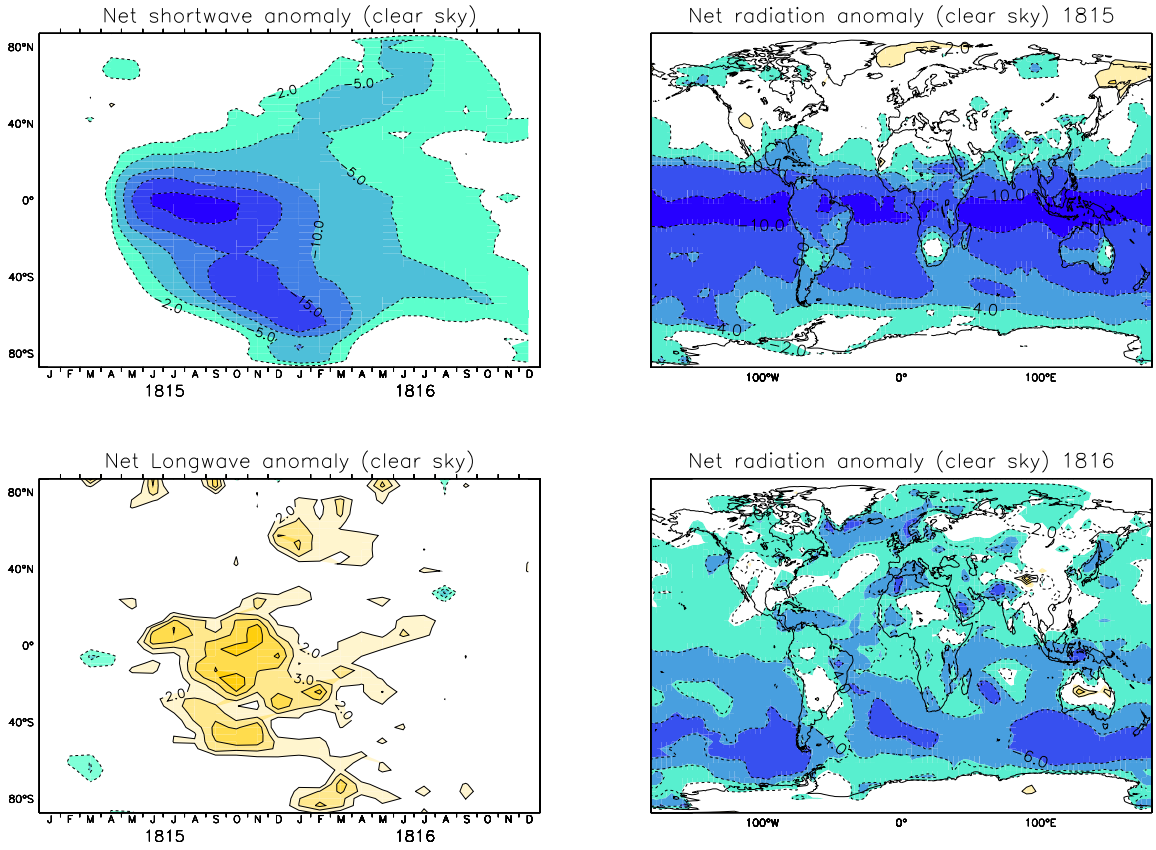

Fig. 4.5: Zonally averaged SW and LW radiative flux anomaly at the surface, clear sky conditions (left panels). Total radiative flux anomaly at the surface for 1815 and 1816 annual means (right panels). Anomalies are computed compared to a reference simulation. Ensemble means from the Tamb.rec.SST scenario are diplayed.

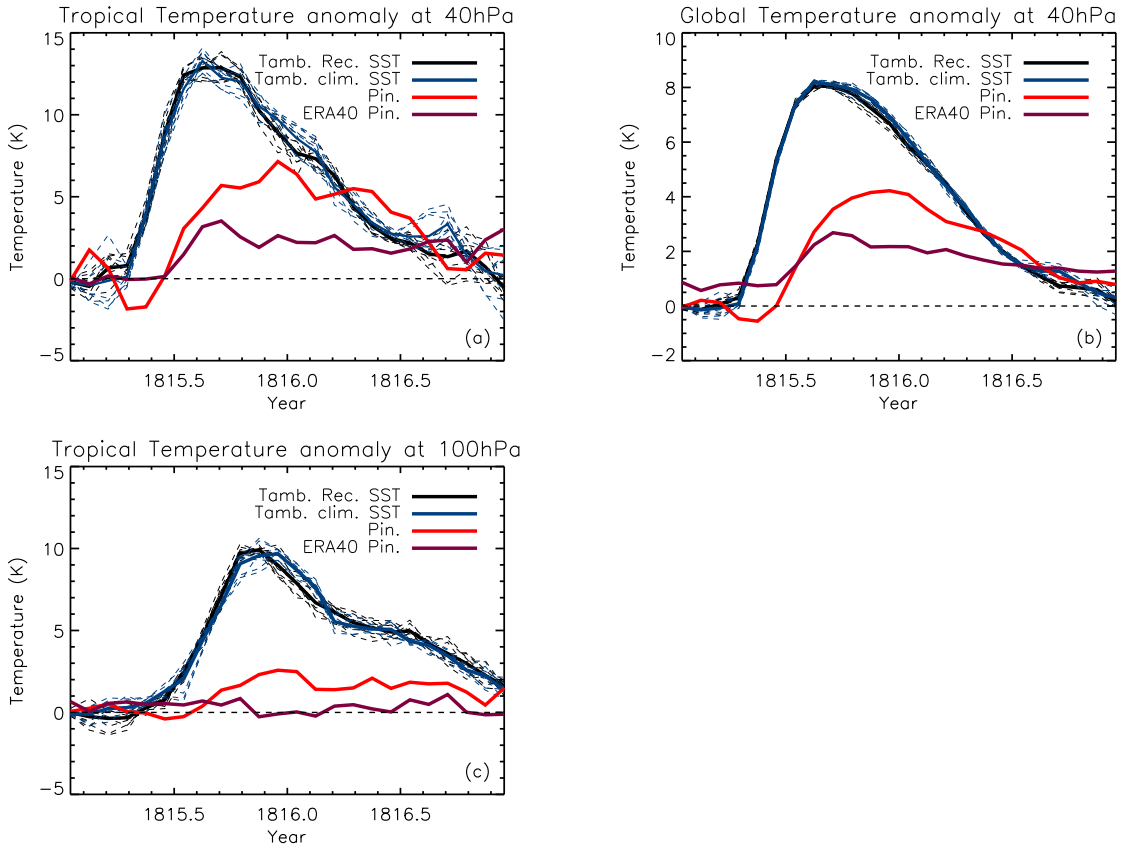

Fig. 4.6: Zonal mean temperature anomalies for tropics (20°S–20°N) at 40 hPa (a) and 100 hPa (c) as well as global mean anomalies at 40 hPa (b). Scenarios anomalies are with respect to a control simulation. Black line is ERA40 temperature data anomalies with respect to 1995-1999. Ensemble means anomalies are displayed in the solid lines, individual members members anomalies in the dashed lines.

which reaches 7 K. Similarly, the global perturbation at 40 hPa shows a 8 K warming in late 1815 while the Pinatubo simulation shows a 4 K increase in temperature in this region (Figure 4.6(b)). However, SOCOL tends to produce a too large warming compared to observations from ERA-40 for the Pinatubo eruption and the stratospheric warming after Tambora is hence likely to be overestimated as well. At the tropical tropopause (Figure 4.6(c)), the warming reaches 10 K. Compared to our Pinatubo simulation (2-3 K), this strong increase can be explained by an important amount of large aerosols in this region after sedimentation of the largest particles which formed after the eruption. The larger aerosols formed after the Tambora eruption compared to Pinatubo hence leads to more warming than expected at the tropical tropopause. This large warming leads in turn to an increase in stratospheric water vapor after the eruption (Figure 4.9). The effect of the intense sedimentation of the volcanic aerosols can be seen in Figure 4.6(a,b) as the warming at 40 hPa following the Tambora eruption becomes smaller than after the Pinatubo eruption after 12-14 months.

Fig. 4.7: Global ozone anomalie in Dobson Units in global average and for a 20°S-20°N average for two Tambora experiments compared to reference runs. Ensemble means are displayed.

4.4.2.2 Chemical perturbation

Stratospheric sulfate aerosols impact ozone through the enhancement of heterogeneous chemistry reactions. N_2O_5 hydrolysis on the surface of the sulfate aerosols leads to the formation of HNO_3, a relatively inert NO_x "reservoir" compound (lifetime of a few days):

$$N_2O_5(g) + H_2O(l,s) \overset{HET}{\rightarrow} 2HNO_3(l,s), \tag{4.8}$$

where (l,s) indicates that the water in the condensed phase, either liquid (as in the case for all non-polar regions) or solid (e.g. as ice in the polar winter vortex or in the tropopause region). The generated nitric acid may stay in the liquid or solid phase under extremely cold conditions, but will eventually be released to the gas phase. Consequently, the NO_x/NO_y ratio decreases and the ozone destruction cycle catalyzed by NO_x becomes less important. Under extremely cold conditions HCl may be taken up by the aerosols and the stratospheric aerosols may then provide surfaces for the direct heterogeneous activation of chlorine (*Solomon*, 1999), through heterogeneous reactions such as:

$$ClONO_2(g) + HCl(l,s) \overset{HET}{\rightarrow} Cl_2(g) + HNO_3(l,s). \tag{4.9}$$

However, the low chlorine concentration in the 19^{th} century prevents a large increase in the ozone destruction cycle catalyzed by ClO_x and the common ozone global decrease after volcanic eruption observed for recent eruptions is not observed here, in accordance with the study from *Tie and Brasseur* (1995). The changes in the NO_x cycle predominate and ozone globally increases. Figure 4.7 shows the global mean and tropical mean total ozone column anomalies as a function of time for the Tambora simulations compared with background aerosol conditions. In the tropics, the total ozone column decreases by 8 DU while it increases globally by up to 17 DU in the beginning of 1816. In the tropics, the important stratospheric warming leads to ozone depletion as the H_2O concentration rises (see Figure 4.9). The high H_2O concentrations leads to a enhancement of the ozone destruction cycle catalyzed by HO_x. Interestingly, even though the tropical stratosphere warms considerably, the HO_x enhanced ozone destruction cycle does not compensate the decrease in the NO_x cycle, contrary to the results from *Dameris et al.* (2005) for the Agung 1963 eruption. However it limits its impact and ozone does not increase dramatically after the eruption. Our results can be compared to the findings from the Agung eruption by *Austin and Wilson* (2006), with a the global average increase of ozone of about 5%, as we find for the Tambora eruption. The increase in H_2O in the stratosphere in turn impacts the radiation, leading to an increase in longwave radiation at the surface additionally to the direct aerosol effect (*Joshi and Jones*, 2009; *Solomon et al.*, 2010). Insights on the ozone responses from a Agung size eruption compared to a larger eruption like Tambora are shown in section 4.4.3.

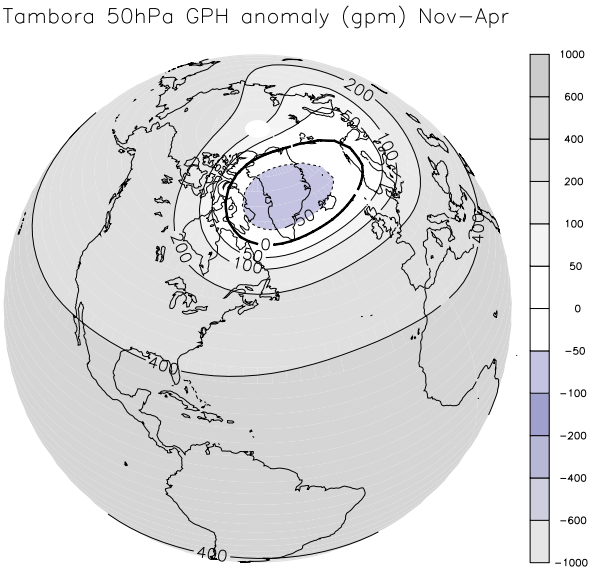

Fig. 4.8: Geopotential heigth anomalies at 50 hPa for the Tambora eruption 60 Mt 23-25 km experiment compared to a reference run. Ensemble means are displayed.

4.4.2.3 Dynamical perturbation

The large radiative heating in the tropics after the eruption increases the equator to pole temperature gradient in the lower stratosphere accelerating the polar vortex (*Stenchikov et al.*, 2006). This important dynamical impact is well reproduced in our simulation. Figure 4.8 shows the geopotential height anomaly for the November 1815-April 1816 period for the 60M2325 experiment compared to a control simulation.

4.4.3 Idealized simulations/Synthesis

'Idealized' volcanic simulations were performed injecting 5, 10, 20, 60 and 200 Mt on April 10^{th} at 23-25 km altitude in the equatorial region.

The impact of coagulation leading to a non-linearity in the SW/LW ratio with increasing mass loading is clearly visible in Figure 4.9a which exhibits the maximum in the radiative anomalies after the different scenarios. The global average downward shortwave radiation flux to the surface doubles from the 60 Mt simulation to the 200 Mt one (-11.1 W/m^2 to -21.8 W/m^2), while the longwave flux increases by more than 3 times (2.66 W/m^2 to 8.4 W/m^2). This effect is already observed between the 20 Mt to 60 Mt simulations, where the anomalies are multiplied by 1.5 and 1.8 for the shortwave and longwave respectively. The influence of the fast sedimentation of large aerosols is clearly seen in Figure 4.9(b,c): The radiative anomalies 18 months after the eruptions decrease between the 60 Mt and 200 Mt scenarios. Similarly, the global temperature at 50 hPa drops for eruptions larger than 20 Mt, as the large aerosols sedimented and warm the lower levels, cooling therefore higher up compared

to a background aerosol case. Six months after the eruption, the stratospheric warming at 50 hPa of the 200 Mt experiment is already fading. Another interesting characteristic is the response of the H_2O at the tropical tropopause and of the ozone. The peak anomalies (Figure 4.9a) show a strong increase in H_2O for large eruptions, with an increase of water vapor of 6.6 ppmv and 33.3 ppmv for the 60 Mt and 200 Mt experiments respectively. The ozone responses show a "spike"for the 5 Mt scenario for its peak anomaly, with an increase of 9.8 DU, while the 10 Mt scenario anomaly only reaches 5.4 DU. This could be a consequence of the smaller tropical tropopause warming and H_2O transport to the stratosphere in the 5 Mt scenario, leading to less ozone destruction through the HO_x cycle. This effect can be seen in Figure 4.9c: The ozone anomaly after the eruptions is much more limited for the 200 Mt scenario than for the 60 Mt as a consequence of large quantity of H_2O in the mid-latitudes stratosphere 18 months after the eruption in the 200 Mt case. A year and a half after the eruption, the 60 Mt and 5 Mt experiments show the largest ozone increase. As described, the radiative and chemical perturbations show strong non-linearities in these simulations. Additionally, the strenghtening of the polar vortex also vary in magnitude with the different size of eruptions. Figure 4.9b shows the anomalies in the gradients of the geopotential height at 50 hPa between 55°N and 75°N in the first winter after the eruptions. From these simulations we see that these anomalies tend to slowly reach a threshold value as eruption sizes increase. For the 10 Mt scenario the anomaly is 200 gpm. This value is multiplied by 5 for the 20 Mt eruption and by 12 for the 60 Mt eruption. The extreme 200 Mt case shows twice the response of the 60 Mt eruption. The reasons for this are unclear as many factors are in play. The influences of the variations in the tropical warming and of the polar ozone responses with different eruption sizes should be further examined. The spatial distributions of the geopotential height anomalies at 50 hPa are shown in Figure 4.10.

4.5 Conclusions

Simulations of the Tambora eruption with the Chemistry-Climate model SOCOL were carried out and key parameters for the analysis of the stratospheric response to this large volcanic eruption were recognized. Important boundary conditions and stratospheric responses were highlighted:

1. Hemispheric estimates from ice core calibration can be challenged. Our approach does not restrict the aerosol distribution to a chosen hemispheric partitioning. In the simulations, the date and latitude of the eruption influence highly the hemispheric partitioning of the volcanic aerosols. For the Tambora eruption, the AER-2D model produce an asymmetrical aerosol cloud with 70% of the aerosol mass transported to the southern hemisphere. This has subsequently a large impact on the latitudinal distribution of the radiative forcing.
2. The very high altitudes for the inital eruption column estimates found in the litterature (43 km, *Sigurdsson and Carey* (1989)) seem unrealistic and do not represent the relevant altitude of the SO_2 injection. However, a smaller (5-10 km) increase in altitude distribution of the aerosol compared to Pinatubo is indicated by Plumeria and ash deposits. Accounting for a higher injection in our experiments, we see a an increase in surface area density above 100 hPa.

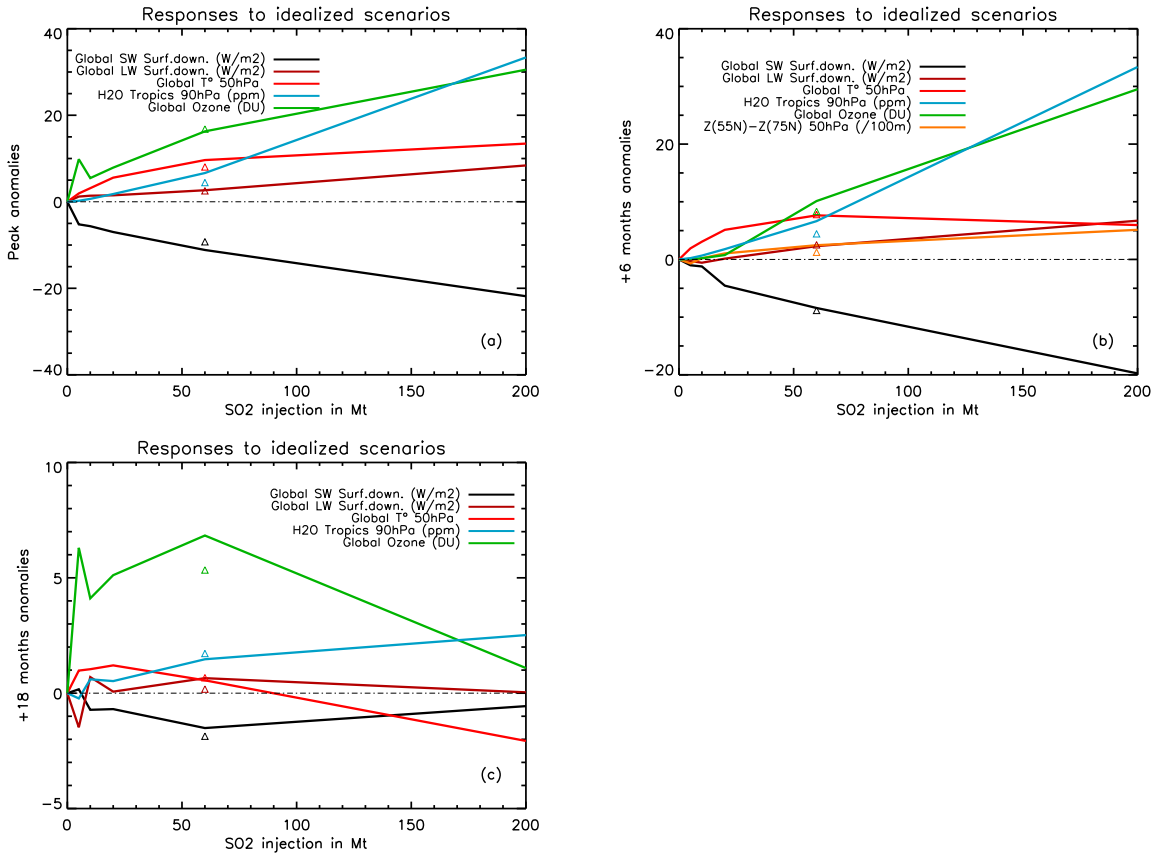

Fig. 4.9: Different stratospheric responses to idealized volcanic simulations carried for 5, 10, 20, 60 and 200 Mt SO_2 injections. Anomalies are computed from a background control simulation. Stratospheric anomalies of shortwave and longwave downward radiations are given at the surface. Global temperature at 50hPa is given in K, tropical water vapor at 90 hPa in ppmv and global ozone column in Dobson units. Anomalies are computed at their peak (a) as well as 6 months (b) and 18 months (c) after the eruptions. Additionally, the geopotential height gradient at 50 hPa between 55°N and 75°N for the first winter after the eruption (Nov-Apr) is given in (b). Triangles show values for the Tambora eruption from the Tamb.Rec.SST ensemble mean.

3. For a Tambora size eruption of 80 Mt, no OH limitation effect has been observed using the AER-2D model with interactive chemistry.

4. The size distribution of the Tambora aerosols is shifted towards larger aerosols compared to Pinatubo aerosols. This is due to a more intense coagulation as the aerosol concentration in the stratosphere is larger. This has two important consequences. First, the absorption to scattering ratio of the aerosols increase as their radii get larger. This leads a smaller shortwave surface decrease than expected from a simple scaling from the Pinatubo eruption, and conversely a stronger longwave perturbation. Second, the larger aerosols fall down faster. This leads to a radiative forcing from the Tambora eruption comparable to Pinatubo 1.5 year after the eruptions.

5. The stratospheric warming induced by the aerosol absorption in the near infrared and terrestrial longwave radiation after Tambora reaches 14 K in the tropics and 8 K globally at 40 hPa in our model. However, a comparison of a Pinatubo simulation with ERA-40 data suggests that the warming tends to

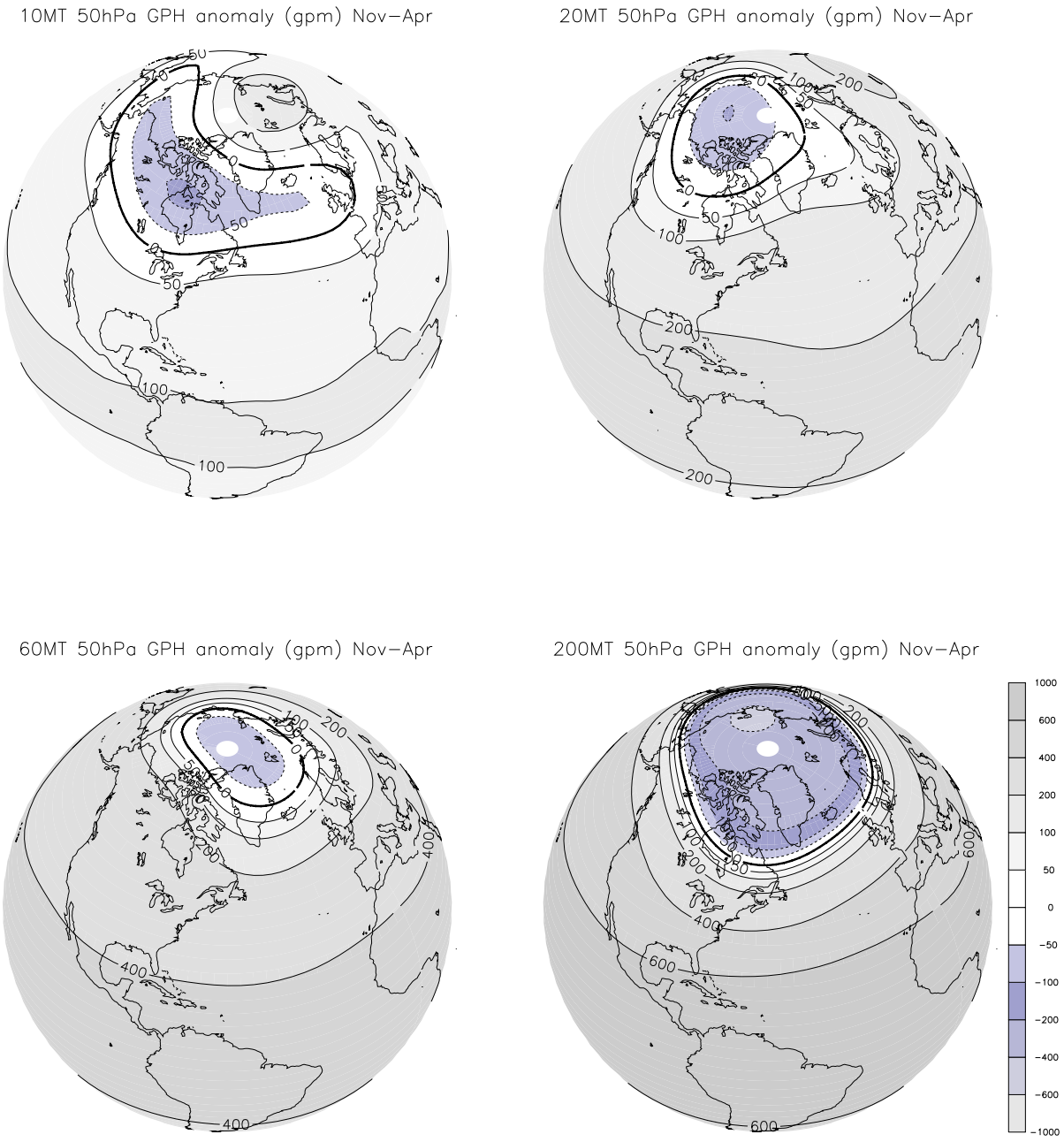

Fig. 4.10: Winter (Nov-Apr) geopotential heigth anomalies (m) at 50 hPa for idealized simulations carried with 10, 20, 60 and 200 Mt SO2 injections. Anomalies are computed from a reference background simulation.

be overestimated in our approach. At the tropical tropopause, a large temperature increase of 10 K is simulated, leading to a stratospheric water vapor increase.

6. The pre-industrial concentration of stratospheric chlorine at the time of the Tambora eruption leads to a global ozone increase after the eruption due to the predominance of the N_2O_5 hydrolysis on sulfate aerosols which leads to denoxification. Conversely, ozone decreases in the tropics as a consequence of the increase in stratospheric H_2O.
7. The dynamical response in the first winter after the Tambora eruption involves a strenghtening of the polar vortex, as observed for large volcanic eruptions (*Stenchikov et al.*, 2006). This behaviour is well reproduced in this study.
8. Using alternatively a reconstruction from *Mann et al.* (2009) and a (1886-1915) climatology, we observed that the influence of sea surface temperature on stratospheric warming and general radiative anomalies is small. Impacts on troposheric circulation will be discussed in a subsequent article.
9. Idealized volcanic simulations were carried out for SO_2 releases of 5, 10, 20, 60 and 200 Mt. The relative decrease in the shortwave effect with increasing aerosol loading due to diminished scattering efficiency of larger aerosols is observed. The influence of the increse in the sedimentation speed is also seen in our simulations, with a maximum shortwave reduction of around -1.5 W/m^2 for the idealized simulations 18 months after the eruption. Strong non-linearities in the ozone responses are also visible, notably due to variations in surface area densities and stratospheric water vapor contents.

Acknowledgments. *This work was supported by the cogito foundation, the Department of Environmental sciences of ETH Zurich, as well as through the Swiss National Science Foundation (NCCR Climate and FUPSOL).*

Chapter 5

Conclusions and Outlook

5.1 Conclusions

This thesis has focused on the modeling of microphysical and atmospheric responses to stratospheric aerosols from large volcanic eruptions. The representation of volcanic eruptions in climate models is subject to uncertainties, from the observational basis used to calculate the aerosol forcing to the radiative, chemical and dynamical responses in climate models.

Within this work we first analyzed the uncertainties present in volcanic aerosol forcings by investigating their contribution in the common overestimation of the stratospheric warming following the Pinatubo eruption in climate models. This large tropical eruption is the best characterized eruption on record and is used as a reference to test the climate responses to volcanic eruptions in numerical models. However, due notably to opacity saturation of the satellite measurements and scarcity of ground lidar measurements in the tropics, the reconstruction of the aerosol size distributions is complicated. Information about the size distribution of the particles is however important in order to reconstruct accurately the aerosol absorptions in the infrared after the eruption and hence provide a correct volcanic forcing for climate models. We have used different aerosol size distribution calculations derived from a state-of-the-art version of the SAGE II observations and from a microphysical model (AER-2D). We analyzed their validity by comparing their optical results with observations of shortwave and infrared extinctions. The impacts on stratospheric temperature perturbations, as calculated with the chemistry-climate model SOCOL, were then analyzed for the different forcing aerosol datasets calculated.

The method generating aerosol size distributions calculated to match the extinctions in the four wavelengths of SAGE II gave the best results for the calculation of the extinctions in the infrared when compared to observations from ISAMS. Results from this approach are in close agreement with both the shortwave and the infrared measurements. We used this method to calculate the extinctions, single scattering albedos and asymmetry factors as inputs for the CCM SOCOL. Stratospheric temperatures are globally overestimated in SOCOL when using this forcing. Climate models using forcings based on outdated SAGE II datasets (as in *Stenchikov et al.* (1998) which provides too low values of infrared extinctions above

20 km and too large values below) would simulate a larger tropical stratospheric temperature increase in the lower stratosphere and a smaller increase at the tropical tropopause if they would use this forcing, which is closer to 12 μm extinctions observations. Models using heating rates derived from *SPARC* (2006) SAD data or the *Sato et al.* (1993) "GISS" dataset likely cannot resolve accurately the aerosol optical properties in the whole spectrum using these datasets and a fixed distribution width, as exhibited in Chapter 2 of this thesis. From these results we conclude that the common overestimation of the stratospheric warming after the Pinatubo eruption by climate models is likely to come from internal radiative deficiencies for the models using heating rates derived from *Stenchikov et al.* (1998) extinction data while climate models using *Sato et al.* (1993) optical depths associated with a fixed distribution width may conversely generate too large infrared extinctions. At the tropical tropopause, the overheating of the models could be reduced by using our dataset (which lies in the low limit of the ISAMS uncertainty range). The satellite observations give valuable information which can be used for the Pinatubo eruption, however there is a need to test our understanding of microphysical processes by using a model-based approach to simulate all processes from the volcanic SO_2 injection to the atmospheric perturbations. Indeed, studies on the sulfate geoengineering proposal by *Crutzen* (2006), or on the climate impacts of large historical eruptions cannot rely on atmospheric measurements. We therefore tested the accuracy of an approach using the AER-2D sulfate aerosol model to simulate the Pinatubo eruption. A simulation with an injection of 7 Mt of sulfur in the stratosphere was carried out. Extinction results from this simulation are in general good agreement with observations in the extra-tropics but overestimate the shortwave and infrared extinctions in the equatorial region in the first months after the eruption. Sensitivity studies with different injection masses, location of injections, microphysical parametrization in the model, or different atmospheric transport did not provide better results in the tropics (see Appendix A). Despite the overestimation of the extinctions at the equator in the first months after the eruption, the AER-2D model ranks among the best aerosol models available (*SPARC*, 2006) and can provide useful information for geoengineering studies (*Heckendorn et al.*, 2009) and for simulations of historical eruption as shown in the Chapters 3 and 4 of this manuscript.

In the Chapter 3, the AER-2D model was used as part of a new approach to generate a volcanic aerosol forcing for the last 400 years. Different uncertainties arise when historical volcanic eruptions which occured prior to the development of extensive atmospheric extinction measurements have to be modeled, and information needed by climate models in order to simulate accurately the response to the eruptions require precise aerosol data. In the last centuries, several large eruptions occured and influenced the climate. However, the level of understanding of their influences is limited by the large uncertainties in the volcanic aerosol information, as the knowledge on the amount of aerosols and their sizes and spatial distribution have to be derived from limited data sources. Before the satellite era (1979), only isolated solar extinction data is available, and before 1883 the only source of information is the sulfate deposition in polar ice cores. These restrictive materials have to be supplemented by assumptions and parametrisations, notably on the size, latitudinal and altitudinal evolutions of the aerosols. This leads to

large uncertainties in the external forcing used in climate simulations of the last centuries. In this work, we used the volcanic plume model Plumeria (*Mastin*, 2007) and the AER-2D aerosol model to generate a volcanic aerosol forcing for climate models. Twenty-six eruptions were simulated using state-of-the-art ice core data and information on the initial altitude, latitude and date of the SO_2 release for each eruption. The results for the global mean 0.5 μm optical depth are in overall agreement with previous reconstructions, but important differences in hemispheric partioning and tropical values are observed. The asymmetry in the Agung 1963 aerosol hemispheric partitioning is for instance better captured by our method compared to previous reconstructions, and in general the spatial distributions from the historical eruptions are consistent with our knowledge of the stratospheric transports. As expected and observed in recent eruptions, large extinctions are modeled in the tropical reservoir region just after the eruptions (although overestimated in our approach), and the hemispheric partitionings of the aerosols follow the seasonality of the tropical pipe latitudinal extent and of the Brewer-Dobson circulation. From these findings, we recommend the use of this volcanic forcing as a credible alternative approach to latitudinal parametrisations constrained by hemispheric calibration from ice cores. Using this volcanic dataset together with previous reconstructions will help to account for the full range of uncertainties in the volcanic forcing for climate modelisations covering the last centuries. This could in turn favor the assessment of the magnitude of other external forcing and of internal climate variability.

The last step of this thesis was to analyze the Tambora 1815 eruption, the largest present in the 1600-2011 volcanic forcing. The eruption released around 60 Mt of SO_2 into the stratosphere, which corresponds to 3-4 times the quantity released by the Pinatubo eruption. The large forcing arising from the stratospheric aerosols from the Tambora eruption is valuable as it provides a test for the models used to assess its climate response. The strong radiative, dynamical and chemical perturbations due to the Tambora aerosols offer a large signal to noise ratio and can be well identified. In the same way as for the Pinatubo eruption, we used the CCM SOCOL to simulate the climatic response to the Tambora stratospheric aerosols. We focused on the stratospheric responses and analyzed the radiative, chemical and dynamical impacts of the eruption. The first important result is the transport of 70 % of the aerosol mass to the southern hemisphere after the eruption, following the strong Brewer-Dobson circulation to the south in austral winter. This has evidently large effects on the latitudinal distribution of the radiative perturbations. Another characteristics of the eruption as simulated in this study is the aerosol size distribution which is shifted to larger radii than for the Pinatubo due to more intense coagulation right after the eruption. This leads to a more limited shortwave surface decrease and conversely a stronger longwave perturbation than expected. Also, due to more intense sedimentation, the radiative forcing from the Tambora eruption is comparable to Pinatubo 1.5 year after the eruption. For these two reasons, the stratospheric warming is then particularly important at the tropical tropopause (10 K warming). Chemically, the low concentration of stratospheric chlorine at the time of the eruption leads indirectly to an ozone global increase after the eruption and a decrease in the tropical region due to large amounts of stratospheric H_2O. This does not affect much the latitudinal distribution of the

stratospheric warming and a strengthening of the polar vortex is still observed in our simulations. Finally, we performed idealized simulations of volcanic eruptions releasing 5, 10, 20, 60 and 200 Mt of SO_2 to investigate further the non linearities in the radiative, chemical and dynamical responses. The relative decrease in the shortwave effect with increasing aerosol loading due to diminished scattering efficiency of larger aerosols is clearly visible in our simulations for eruptions larger than 20 Mt. The influence of the increase in the sedimentation speed is observed as well. Strong nonlinearities in the ozone responses are also highlighted.

5.2 Outlook

5.2.1 Next large eruption

The probability that a climatically relevant eruption will happen in the next decades, from a Pinatubo to a Tambora size eruption is far from being negligible. Moreover, large caldera-forming volcanoes which can create extremely important eruptions can awake in a very short timescale of months to decades (*Druitt et al.*, 2012) and lead to even larger climate impacts. Testing the ability of climate models to reproduce spatial patterns in the reponses to large eruptions could be done by making use of the diversity in volcanic eruptions over the last centuries. The influence of the specifities in forcings (mass, radius, latitude distribution) and climatic states (ENSO, NAO) at the time of eruptions should be investigated in depth. Being ready for the next large volcanic eruption should also involve having a better observational network. As noted in *Robock and Antuna* (2001) and confirmed in this thesis, data from tropical lidars are crucial to observe the volcanic aerosol clouds. To capture accuratly the size distribution of the aerosol, both satellite longwave and shortwave measurements and tropical ground lidars are needed. Measurements from OPC are also extremely valuable for comparisons.

5.2.2 Volcanic eruptions and climate sensitivity

In simulations covering the last centuries, the study of large historical volcanic eruptions is very valuable and can help to infer the climate sensitivity. In the context of the recent climate change, estimating the climate sensitivity is an important task to test climate models and better constrain climate scenarios. There has been recently a lot of debate over the possibility to infer climate sensitivity from volcanic eruptions responses. *Boer et al.* (2007) states that although it may be possible to derive the equilibrium climate sensitivity from large volcanic eruptions responses, high accuracy in the oceanic heat storage, temperature response and volcanic forcing is needed. *Wigley et al.* (2005) looked at volcanic climate responses in 16 climate models and concluded that useful information on climate sensitivity can be obtained from the short-timescale responses to volcanic eruptions, however issues due notably to poor signal to noise ratio in observations and low accuracy in the volcanic forcing (even for the Pinatubo eruption) limit the use of this method. Following these studies, *Bender et al.* (2010) noted that differences in aerosols implemention among models is a clear issue. Studies linking climate sensitivity and volcanic eruptions

would benefit from using datasets closer to state of the art SAGE II data and ISAMS observations, as now a majority of the models base their volcanic aerosol parameterization on the zonal mean vertically resolved optical depths at 550 nm, and the column average effective radii given by *Sato et al.* (1993) or on *Stenchikov et al.* (1998) dataset which were shown to be outdated.

5.2.3 Tambora eruption: Impacts on the troposphere

An important next step would be the analysis of the Tambora eruption impacts on the tropospheric climate. As shown in chapter 4, large stratospheric perturbations arise from this eruption. The strong magnitude of the forcing allows to separate it clearly from the internal variability and from other external forcing in the stratosphere. At the surface, strong anomalies in temperature and precipitation were observed, and comparison of model simulation results to climate proxies and observations would be very valuable to test the validity of the stratospheric impacts and the representation of stratospheric-tropospheric coupling in climate models.

5.2.4 Geoengineering

As today volcanic eruptions are sometimes seen as natural experiments for geoengineering, it is crucial to understand and reproduce better this climate forcing to provide accurate results on global temperatures, precipitation and ozone anomalies, but also on regional changes. Counter-acting the rise in global temperature is indeed not the only issue when one tries to limit climate change impacts, as relevant climatic parameters are not primarily linked to global temperatures: Local temperature and precipitation anomalies over the seasonal cycle associated to recent climate change cannot be easily neutralized by a geoengineered solar reduction technique and important damaging precipitations can for instance occur. Accounting for the various drawbacks in injecting sulfate aerosols in the stratosphere and acknowledging the important effectiveness of using stratospheric aerosols to offset the rise in global temperature, as well as the rapidity of deployment of such a technique; it could be useful to simulate geoengineering scenarios with the AER-SOCOL approach at a time of a sudden climate warming, when the necessity to avoid large irreversible global changes may outweigh the potential drawbacks.

Appendix A

Modelling Mt. Pinatubo eruption: Additional material

This material is issued from a long version of an article draft on the Pinatubo eruption. It completes the results seen in Chapter 2.

A.0.5 Motivation

As noted by *Morgenstern et al.* (2010), different approaches have been followed to represent the volcanic forcing among the CCMs taking part in the CCMVal-2 intercomparison project. Some models (CAM3.5, GEOSCCM, LMDZrepro UMSLIMCATT and UMUKCA-UCAM) do not describe the heating from the aerosol, while ULAQ uses direct sulfur dioxide injections and then models its own sulfur chemistry and aerosol microphysics. The other models derive heating rates consistent with prescribed SAD data (CMAM and WACCM), the *Sato et al.* (1993) GISS data (AMTRAC3, CCSRNIES, MRI, UMETRAC,UMUKCAMETO), the precalculated heating rates from *Stenchikov et al.* (1998) (E39CA, EMAC), or the state-of-the-art SAGE gap-filled dataset (SOCOL). All these methods depend on the quality of the underlying volcanic dataset used. A wrong parametrization of the volcanic aerosol forcing can lead to a false error attribution to the radiation scheme of a specific model or it can hide a model bias by compensating errors in both the external forcing and the radiation scheme. Temperature overestimation in the stratosphere after major volcanic eruption is a problem common to many GCMs and CCMs (*Eyring et al.*, 2010). However this problem can also partly be due to defficiencies in the representation of other mechanisms such as ozone depletion, the Quasi biennal oscillation, or stratospheric water vapor increase through the tropical tropopause. In a similar context, *Kravitz et al.* (2011) point to the differences in chemical response to geoengineering scenarios, when aerosol are prescribed in different ways in the CMIP5 models.

A.1 Methods

A.1.1 Observations

Optical properties as extinction, single scattering albedo and asymmetry factor of stratospheric aerosols as well as Surface area density (SAD) are essential to model the climate impact of large volcanic eruptions. Optical parameters have to be computed for the different spectral bands of the climate models. The different types of measurements capture various features of the aerosol properties, as extinction or SAD for instance, but the temporal and spatial coverage differ for most of the measurements and it is therefore difficult to compare those measurements between each other and to produce a consistent long term record of stratospheric aerosol properties. The most relevant observational systems of the Pinatubo eruption are shortly described here. For a more complete review on stratospheric aerosol measurements see for example *SPARC* (2006).

A.1.1.1 Satellite observations

Stratospheric aerosol measurements by satellite give important information on the spatial distribution of the aerosols. The spatial coverage of satellite measurements cannot be reached by any other type of measurements, making it their biggest advantage. The extinction measurements of the Stratospheric Aerosol and Gas Experiment (SAGE) using solar occultation technic provide one of the most valuable

data sets in the sense of longterm observations on stratospheric aerosols. **SAGE II** measured from 1984 to 2005 aerosol extinctions at wavelength from 386 to 1020 nm, of which the channel at 1020 nm shows the best signal-to-noise ratio. The satellite measurements cover nearly the whole globe (80°S-80°N). Above ∼35 km the temperature becomes so high that the aerosols completely evaporate and the extinction becomes too low to be measured. During background conditions termination is frequently reached in the troposphere due to clouds whereas during large volcanic eruptions termination can occur due to ash and stratospheric aerosols. For instance after Mt. Pinatubo eruption SAGE II could not measure below 23 km for several months. The processing procedure of SAGE data using a four channel algorithm (*Chu and McCormick*, 1979) has been improved (*Thomason et al.*, 2001). Compared to older processing algorithms of SAGE II this more recent data set shows higher extinctions at 1020 nm. Data from SAGE instruments were used in many studies to examine stratospheric aerosol trends (e.g. *Thomason et al.*, 1997a; *Bingen et al.*, 2004a,b) or for the creation of surface area density data set (e.g. *Thomason et al.*, 1997b).

Additional satellite measurements are available from the Halogen Occultation Experiment (HALOE), the Advanced Very High Resolution Radiometer (AVHRR), the Improved Stratospheric and Mesospheric Sounder (ISAMS), and the Cryogenic Limb Array Etalon Spectrometer (CLAES). A short description of these data sets is given in Table A.2.

It should ne noted that June 1991- December 1992 AVHRR optical depth at 0.5 μm is about 36% larger than sunphotometer at Mauna Loa (MLO) (LongStowe et al, 1994). AVHRR underestimates the optical depth at 0.5 μm after 1992 in comparison with a sunphotometer (*Russell et al.*, 1996). This is possibly due to a decreased sensitivity of the AVHRR visible channel, drifts in NOAA 11 equator crossing time and/or differences in size distribution and refractive index assumed for AVHRR (LongStowe et al, 1994). SAGE II optical depth at 0.5 μm compares fairly well to MLO sunphotometer. Hence AVHRR should be multiplied with 0.84 during the period June to December 1991.

A.1.1.2 Lidar measurements

A Lidar (Light Detection And Ranging) is a remote sensing instrument using optical wavelengths to measure the backscattering signal from airparticles. The conversion from the backscattering signal to the aerosol properties needs a-priori assumptions such as particle shape, chemical composition and the atmospheric density profile. Theoretically the refractive index, the phase (liquid/solid) and the size distribution can be retrieved through lidar signal inversion. However, the results must be considered with caution, as many a priori assumptions that go into the inversion tend to simplify the aerosol properties. Most operational lidar measurements are located in the northern hemisphere. The nearest stations to the equator are Mauna Loa in Hawaii (19.54°N, 155.58°W), Camagüey in Cuba (21.40°N, 77.92°E) and Saõ José dos Campos in Brazil (23.2°S, 45.9°W). In this study we use a composite of the lidar measurements in Mauna Loa and Camagüey, as these stations are often located under the main stratospheric aerosol cloud after Mt. Pinatubo eruption (*Antuña et al.*, 2002; *Antuna et al.*, 2003). Additionally we use lidar measurements from a NASA

DC-8 airborne lidar mission during 21^{st}, 24^{th}, 26^{th} of May 1992 under the coordination of D. M. Winker as a follow-on to the mission reported in *Winker and Osborn* (1992).

A.1.1.3 Optical particle counter

Balloon borne optical particle counter (OPC) measurements are performed in Laramie, Wyoming [41°N, 106°W] since 1971 (*Rosen*, 1964; *Deshler et al.*, 1992). By measuring forward scattering and using Mie theory (*Mie*, 1908) the size distribution of the aerosol can be deduced. The instrument was improved during the last decades and today condensation nuclei (CN) with radius r $>$ 0.01 μm and aerosol with radii r from 0.15 μm to 10 μm in 12 size ranges from the surface to 30 km altitude are detectable. Measurement uncertainty is mainly due to the pulse width broadening of the photo multiplier tube response for a constant optical input (about $\pm$ 10% at 0.15 and 0.25 μm).

A.2 Uncertainties in SAGE II based aerosol data sets

SAM II and SAGE I-II are the satellite instruments with the highest temporal coverage (1978–today), hence this data has often been used to generate a consistent data set over the whole satellite period (e.g. *Bingen et al.*, 2004a,b; *Thomason*, 1991; *Thomason et al.*, 1997a; *Sato et al.*, 1993; *SPARC*, 2006). However, there are some temporal and spatial gaps in these measurements, for instance after Mt. Pinatubo eruption due to saturation. Satellite measurements at longer wavelength and lidar measurements are used to fill data gaps and improve the formation of global stratospheric aerosol data sets.

A.2.1 Gap-filled SAGE II data sets

The most elaborated gap-filled SAGE II 1020 nm extinction time series is described in *SPARC* (2006) (hereafter referred to SAGE_ASAP). The measurement gaps in the SAGE II measurements, mainly caused by saturation directly after the Mt. Pinatubo eruption, were filled with lidar measurements at Mauna Loa in Hawaii, at Camagüey in Cuba, at Hampton, Virgina in USA and with backscatter sonde measurements form Lauder, New Zealand. The lidar measurements have been converted to 1020 nm (SAGE II wavelength) (*Antuna et al.*, 2003). Mauna Loa (19.54°N) and Camagüey (21.4°N) were frequently below the main aerosol cloud and these values are taken for the tropical region. However, due to the fact that the main aerosol cloud was not always located above the two lidar stations an erroneous seasonality of the aerosol amount could be present in the data set compiled by (*SPARC*, 2006).

A.2.2 Generation of spectrally resolved aerosol optical properties

The particle size distribution has to be known to retrieve extinctions in the whole spectral range. During quiescent times the size distribution of stratospheric aerosol is well captured by a simple unimodal lognormal distribution (Wurl et al., 2010). However after volcanic eruptions a second or third mode is observed, consequently a bimodal (or trimodal) lognormal distribution fits better (*Deshler et al.*, 1992). For simplicity and because of the patchy measurement data many studies nevertheless use unimodal lognormal distributions (e.g. *Kinnison et al.*, 1994; *Russell et al.*, 1996; *Stenchikov et al.*, 1998; *SPARC*, 2006).

In this study we compare three methods to retrieve spectral resolved optical properties, first a method described in *Schraner et al.* (2008) (hereafter referred to SA) using SAGE_ASAP , second a method with varying effective radiuses and distribution widths (called S_free hereafter) to find the best fit with the three wavelengths of SAGE_ASAP extinction measurements, and finally the method by *Stenchikov et al.* (1998) (called ST98 hereafter) using an older version of the SAGE II data set. All these methods assume a unimodal lognormal distribution.

The lognormal size distribution is described by the total number of particles (N_0), the width of the distribution (standard deviation σ) and the mode radius (r_m):

$$\frac{\mathrm{d}N(r)}{\mathrm{d}r} = N_0 \frac{e^{-\frac{1}{2}\left[\frac{\ln^2(r/r_m)}{\ln^2\sigma}\right]}}{\sqrt{2\pi} r \ln^2\sigma}, \tag{A.1}$$

where $N(r)$ is the number concentration of particles with the radius r.

The SAGE based methods are described in Chapter 2 of this manuscript. Note that in this article draft, the SAGE_1.2 and SAGE_1.8 are named SA1.2 and SA1.8, and the SAGE_4λ method is named S_free.

A.2.3 Results

Extinctions in the shortwave and longwave bands are compared to measurements from SAGE II, HALOE and ISAMS. For SA and S_free, extinctions were calculated according to Mie theory (*Mie*, 1908) using refractive indices from *Biermann et al.* (2000), and satellite temperature data to infer the aerosol H_2SO_4 wt %.

A.2.3.1 Visible and near infrared extinctions

Calculated extinctions using the SAGE derived approaches SA and S_free as well as from ST98 are compared to SAGE II extinction measurements at 525 nm and 1020 nm. The S_free approach shows close to perfect agreement with the SAGE observation at both 525 nm and 1020 nm (figure A.1). This illustrates the precision of the S_free method in matching the various wavelengths of SAGE_ASAP by adjusting the number density and distribution width of the aerosols. The large peak around September 1991 could only be captured at 69 hPa (figure A.1 (a)) by allowing small aerosol radii in S_free. The SA approach does not capture the specific 0.5 μm to

1 μm ratio at this period (Figure A.6). Figure A.1 shows that the SA1.2 calculation highly overestimate the extinctions at SAGE wavelengths at 40 hPa around the equator, while SA1.8 gives in comparison better results at 1 μm. The retrieval by ST98 based on outdated data is less than half as SAGE_ASAP 1 μm measurements at 40 hPa in 1991. At 69 hPa its extinction is on the other hand overestimated.

Extinction profiles for December 1991 in Figure A.5 illustrate that the fit to the four wavelengths of SAGE of the S_free method works well for capturing the 1 μm extinction at every altitude. At this wavelength, SA1.8 and especially SA1.2 are overestimating the observations. The retrieval by ST98, which follow the Russell et al. (1996) 1.02 μm data overestimates the SAGE_ASAP data above 27 km and below 20 km at the equator and misses the peak around 22-23 km. At 35°N, its extinction peak is 3 km too low, leading to a large overestimation below 70 hPa. At 35°N, 69 hPa, all approaches except SA1.2 are close to the measurements at 1 μm, ranging inside the uncertainties (figure A.2).

ST98 captures well the 0.5 μm to 1 μm ratio just after the eruption but then shift towards overestimating shorter wavelengths (Figure A.6). This can be seen in Figure A.2 as ST98 overestimate the 0.5 μm from 1992 on.

In Figure A.8 the time evolution of stratospheric optical thickness at 0.55 μm is shown for the Equator (5°S-5°N). The thin black line in Figure A.8 shows the area of 0.84 times the AVHRR values as proposed by *Russell et al.* (1996). According to AVHRR measurements ST98 underestimate the total optical thickness in the shortwave in the tropics during the first half year. For the same region SA slighty underestimates it according to AVHRR and S_free exhibits lower values than AVHRR after the initial peak. The *Sato et al.* (1993) optical depth shows a similar shape as ST98, with a shifted peak earlier in time and a subsequent decrease closer to AVHRR data.

A.2.3.2 Infrared extinctions

The 5.26 μm and 12.1 μm extinctions give some information about the aerosol absorption in the longwave which is relevant for the stratospheric warming after the eruption. At 40 hPa (Figure A.1), where the largest extinctions are seen, the SA approach overestimates the extinction compared to ISAMS measurements. The S_free calculation show a much closer agreement with the data, while ST98 results are less than half the measurements. At 35°N, 69hPa (Figure A.2) the 12.1 μm SA1.8 results exhibits a too large extinction, while SA1.2 and S_free are close to ISAMS data. ST98 is again on the lower side. At 5.26 μm, equator, all methods fall into the lower estimates of the ISAMS measurements which exhibit large error bars (Figure A.5). At 35°N the ST98 extinctions profile exhibit a too wide shape in altitudes compared to HALOE measurements, underestimating the HALOE extinction peak by 50% and strongly overestimating these observations below 17km. At 12.6 μm, the S_free calculation is in good agreement with ISAMS observations, especially above 20 km. The SA1.8 and SA1.2 results are too high. In the high extinction region, ST98 calculations values are less than half the ISAMS measurements.

The extinction ratios shown in Figure A.6 are a direct measure of particle size. Before the eruption, the extinction ratio of 0.55 μm to 1 μm is larger than 1, as

very small particles ($< 0.1\mu$m) dominate the scattering. Directly after the eruption these ratios may initially even increase because of freshly nucleated very small particles., however just a few weeks after the eruption these ratios drop significantly below the background value because large particles produced by coagulation start dominating the scene. In contrast, the ratio of 1 μm to 5.1 μm extinctions increases after the eruption because of the increased efficiency of scattering at 1 μm while the extinction at 5.1 μm is mainly due to absorption and hence only proportional to the stratospheric increase in mass density.

We can see in the extinction ratios of 1 μm to 5.1 μm that after Pinatubo SA1.2 has a bias towards the short wavelengths at the equator. On the other hand at low altitudes SA1.8 tends to overestimate longer wavelength due to its wide size distribution containing very large particles. ST98 during volcanic time overestimates the 1 μm to 5.1 μm ratio by almost a factor two at the equator, while ranging on the high side of observations for 35°N. S_free is notably in good agreement with observations for the 1 μm to 5.1 μm ratio at 40 hPa.

A.3 Uncertainties in AER modelling

A.3.1 Uncertainties in boundary conditions for the aerosol model AER

Several boundary conditions were used for the AER 2D aerosol runs. Their characteristics is summarized in Table A.1. Differences consist in :

1. Source magnitude
   Measurements for the sulfur amount injected into the stratosphere are subject to uncertainties. Total uncertainty in the amounts range from 7 to 13 Mt S (Lambert et al., 1993, Guo et al., 2004, Thomason and Peter., 2006) . Different scenarios accounting for these sulfur amounts were hence chosen in our AER simulations to account for this uncertainty. Injections of 7 to 11 Mt of sulfur were computed with AER.
2. Vertical source distribution
   Another important parameter is the vertical distribution of the SO_2. No accurate measurements are unfortunately available for this. Different estimates were chosen to cover the possible range of the initial vertical spread of the SO_2 cloud. 23-25 km distributions and a broader 16-29 km distribution (P10_v) were computed. The altitudinal spread of the injection will influence the size distribution of the aerosol, an higher concentration leading to the formation of larger particles. Moreover due to the long residence time in the tropical pipe, differences in SO2 altitude distribution can lead to disparities in the timing of the transport to the extra-tropics through the tropical transition layer and above the tropical reservoir.
3. Transport parameters
   P10_ASAP correspond to P10_v but with climatological transport instead of a transcient 1991-1996 one. The transport is of course an essential parameter

to capture the correct latitudinal evolution of the aerosol.

Another scenarios was also tried where the injection was spread in time over several days. This scenario didn't lead to noticeable change in the results and isn't shown here.

Figure A.5 shows that 6 months after the eruption, AER simulations generally show too large values for 1 μm and 12.6 μm extinctions at the Equator. The altitudinal shapes of Pin7 and Pin9 simulations are consistent with observations, while the climatological transport used for Pin10_ASAP leads to a too low distribution and far too large values. At 35°N, Pin7 and Pin9 do not overestimate largely the extinctions but exhibit a peak 1-2km too high. Pin10_ASAP is always showing too strong values, except compared to ISAMS observations at 5.26 μm as well as 12.1 μm for 35°N.

As shown in Figure A.7 (a), results indicate that changing the injection amount doesn't allow to get close to extinction measurements at 1 μm one year after the eruption at 18°N, 20 km. Here a composite of the Lidars at Mauna Loa and Camaguey is shown for comparison. Peak extinctions are too large by a factor 2 (Pin7) to 3 (Pin11). Pin10_v captures better the early increase in the extinction as well as the rate of the decay. Pin10_ASAP is again the outlier.

In Figure A.7 (c), profiles of the backscattering ratios at 0.532 μm of the AER runs are compared to airborne Lidar measurements in May 1992. Modifying the injection amount doesn't change much the altitudinal distribution at this location. Using climatological winds (Pin10_ASAP) and a wider altitude distribution leads to shifted and widened distribution of the backscattering ratio one year after the eruption at the equator. Using a wider altitudinal injection only leads to more overestimation at high altitudes due to the larger distribution.

A.3.2 Uncertainties within aerosol model AER

Following parametrized processes in the AER-2D aerosol model were modified:

1. Aerosol growth (coagulation)
   Reducing the coagulation rate of the 9 Mt simulation by half leads to a longer residence time of the aerosols, the peak extinction is slightly reduced but after mid 1992, extinction becomes larger than in the reference run Figure A.7 (b). The peak backscattering ratio on may 1992 at the equator gets closer to the lidar observation but increase the overestimation above 25 km Figure A.7 (d)
2. Aerosol transport
   Figure A.7 (b) shows an overestimated and slightly delayed peak extinction at 18°N, 20 km, for the simulation Pin9_Kyy01 where the horizontal eddy diffusivity was divided by 10 in the model. We can also observe a too large backscattering ratio at 0.5μm in may 1992 at the equator in Figure A.7 (d) for Pin9_Kyy compared to observations.

3. Aerosol sedimentation
   Altering the sedimentation rate of the aerosol, using 80 % of its original value leads to only small modification of the peak extinction value as shown in experiment Pin9_sed08 in Figure A.7 (b) but increase the lifetime of the aerosol leading to a decay rate closer to observations. Figure A.7 (d) show the altitude distribution of the Pin9_sed08 simulation, where the diminished sedimentation leads to a profile shifted towards higher altitudes. This reduces the positive bias below 20 km, but misses the correct altitude of the peak backcattering ratio and aggravates the overestimation above 25 km.

Pin9_box is a scenario where the injection was confined to a box over specific longitudes. It shows a closer to observation extinction peak but a too fast decrease (Figure A.7(b)). Its backscattering ratio at 0.5μm at the equator reaches less than half the observational value at 22 km and overestimate it below 18 km (Figure A.7 (d))

A.4 Uncertainties in climate modelling process

Simulations with the CCM SOCOL.v2 were carried to test the stratospheric response to the SA, S_free and Pin7 scenarios. Anomalies in shortwave (SW) at the top-of-atmosphere (TOA) radiation and stratospheric temperature at 40 hPa and 100 hPa are computed in reference to a background aerosol simulation. For the radiative transfer calculation spectral extinctions, single scattering albedos, asymmetry factors as well as the surface area densities directly derived from our approaches were provided as boundary conditions to SOCOL.

Figure A.9 show the TOA net shortwave radiative flux change after Pinatubo. The peak values for the SW anomalies at 60°S-60°N range inside 2.5 W/m^2 (S_free) to 6 W/m^2 (SA1.2) in the first months after the eruption (Figure A.9 (a)) . In the tropics, S1.2 and Pin7 are in broad agreement with ERBE data (Wong et al., 2006) while SA1.8 and S_free tend to underestimate the anomaly (Figure A.9 (b)).

The stratospheric warming after the eruption is in general overestimated, from a 1 K bias in fall 1991 up to 3 K in spring 1992 in the tropics at 40 hPa in S_free compared to ERA40 data (Figure A.10). In the same way ,the global average temperature increase at 40 hPa from the S_free experiment is too high by 1.5 K in spring 1992. The AER results are higher than the S_free calculations for the end of 1991. In the tropical lower stratosphere (100 hPa), our results diverge from ERA40 anomalies in late 1991 for the S_free simulation. While data show little to no warming, SA experiments results in persistent warming of 2-3 K. The warming in the S_free simulation reaches 1.5 K in winter 1992 and is closer to observations. The Pin7 simulation reaches a 2.5 K temperature increase.

Table A.1: Pinatubo eruption scenarios with different annual stratospheric SO_2 emissions, source locations and specific model features

scenario	S input (Mt)	source location	special feature
Pin7	7	5°S-15°N, 23-25 km	
Pin8	8	" "	
Pin9	9	" "	
Pin10	10	" "	
Pin11	11	" "	
Pin9_coag05	9	" "	coagulation rate divided by 2
Pin9_sed08	9	" "	sedimentation rate multiplied by 0.8
Pin9_Kyy01	9	" "	K_{yy} multiplied by 0.1
Pin9_time	9	" "	S injections on several days
Pin9_box	9	restricted to plume	source confined to few longitudes
Pin10_ASAP	10	5°S-15°N, 16-29 km	old transport climatology
Pin10_v	10	5°S-15°N, 16-29 km	new transient transport parameters

Table A.2: Satellite measurements of stratospheric aerosol extinction

Instrument (satellite)	Time coverage	Geographic coverage	Wave length	references
SAGE II (ERBS)	10.1984–10.2005	80°S–80°N	386, 448, 452, 600, 935, 1020 nm	*Chu and McCormick* (1979); *Thomason et al.* (2001)
HALOE (UARS)	10.1991–12.2005	80°S–80°N	2.45, 3.40, 3.46, 5.26 μm	*Russell et al.* (1993); *Hervig et al.* (1995)
CLAES (UARS)	10.1991-5.1993	34°N–80°S/ 34°S–80°N	7 channels from 5.3–12.8 μm	*Roche et al.* (1993)
ISAMS (UARS)	10.1991–7.1992	80°S–80°N	4.51, 5.28, 6.23, 6.76, 7.43, 7.81, 8.09, 10.00, 11.40, 12.10, 16.30 μm	*Grainger et al.* (1993); *Lambert et al.* (1993); *Taylor et al.* (1993)
AVHRR (POES/ NOAA-11)	6.1987-now/ 11.1988–6.2004	90°S–90°N	0.58-0.68, 0.724-1.10, 3.55-3.93, 10.3-11.3 and 11.5-12.5 μm	*Geogdzhayev et al.* (2004)
ERBE (ERBS/ NOAA-9, NOAA-10)	10.1984-now	67.5°S–67.5°N/ global	global albedo, fluxes, and solar incidence	*Wielicki et al.* (2002); *Wong et al.* (2006)

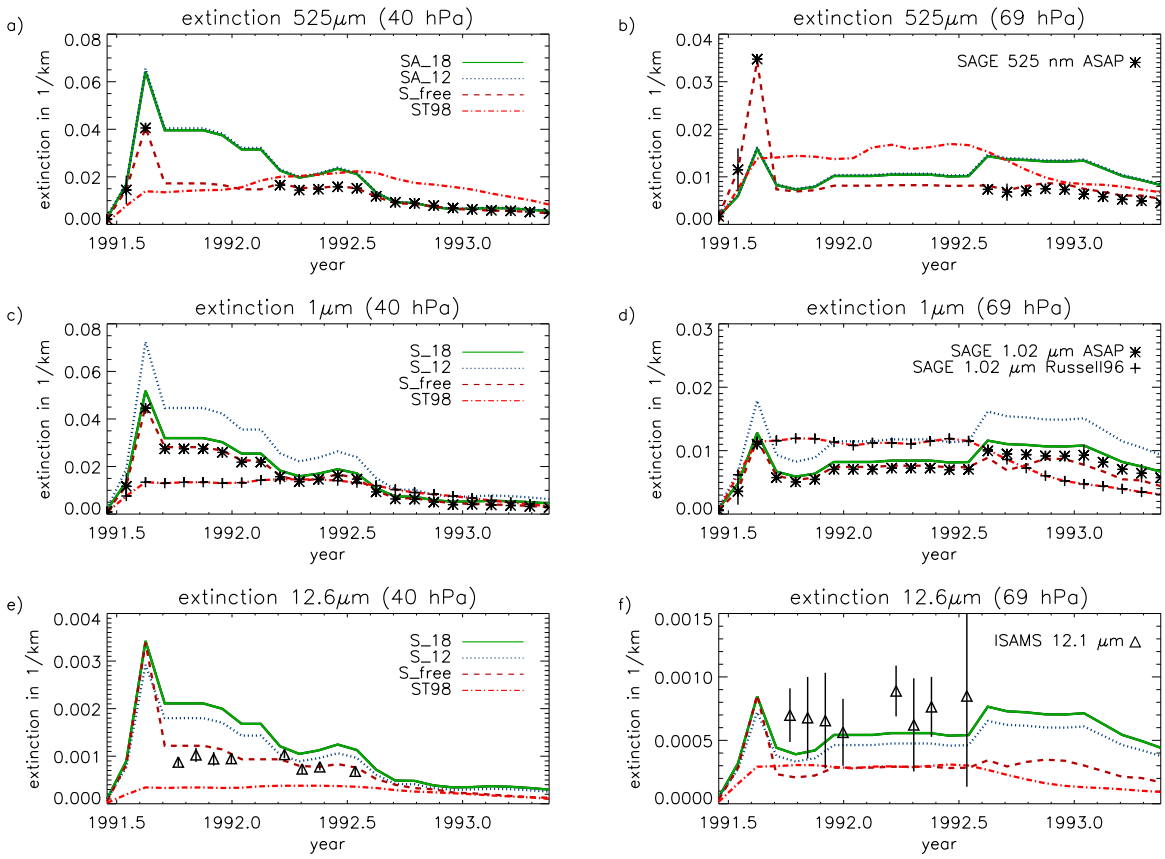

Fig. A.1: Zonal mean extinction from June 1991 to June 1993 for 0.5 μm, 1 μm and 12.6 μm. Left column at the equator (5°S–5°N) at 40 hPa, right column at 69 hPa. Vertical lines show error bars of measurements when available.

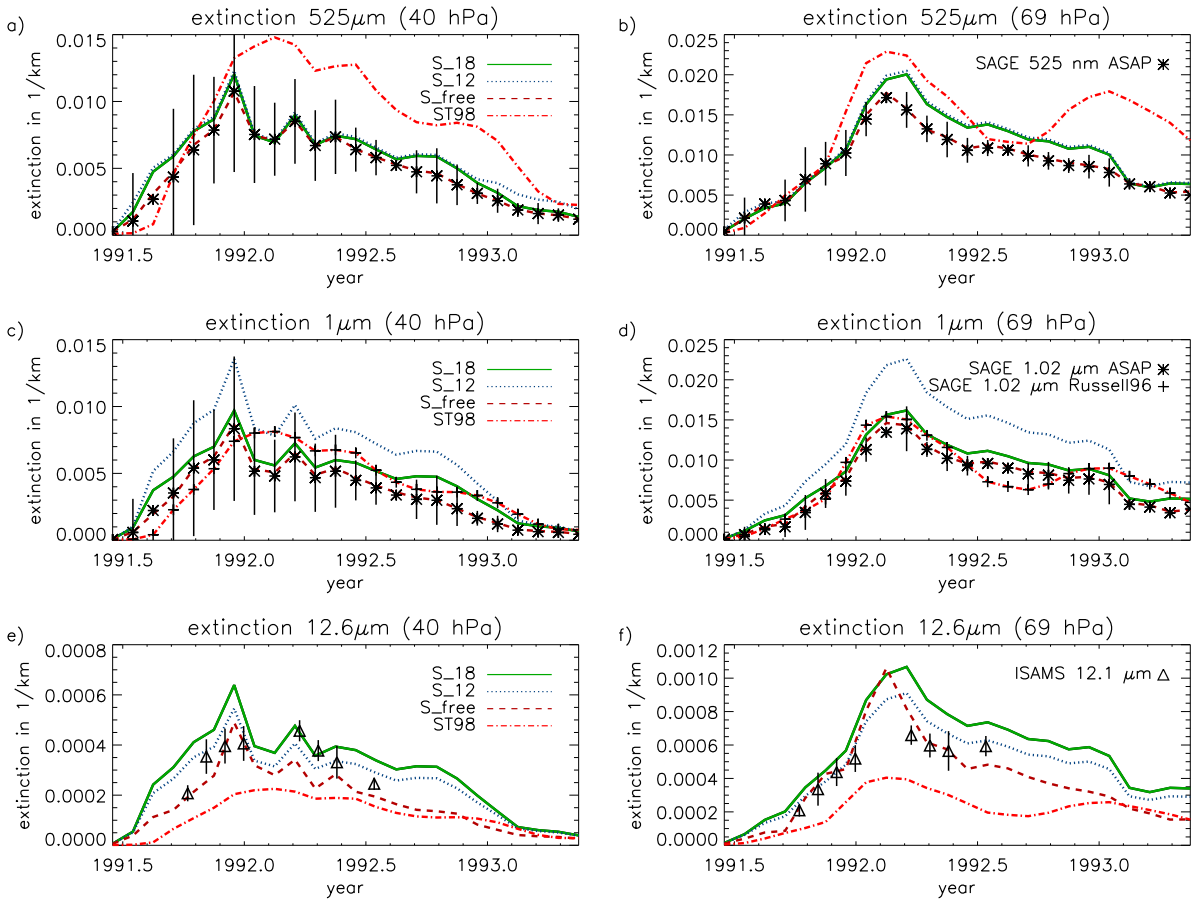

Fig. A.2: Zonal mean extinction from June 1991 to June 1993 for 0.5 μm, 1 μm and 12.6 μm. Left column at northern midlatitudes (30°N–40°N) at 40 hPa, right column at 69 hPa. Vertical lines show error bars of measurements when available.

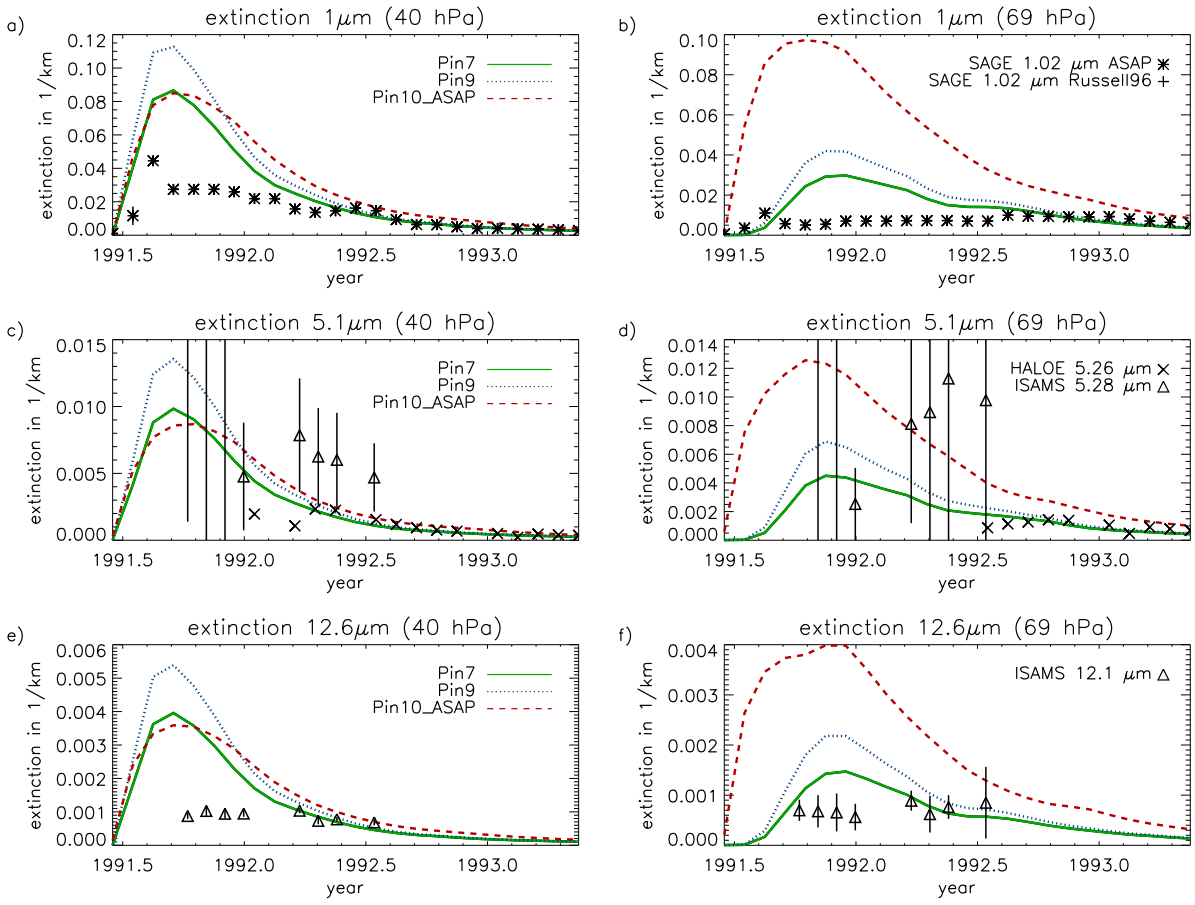

Fig. A.3: Zonal mean extinction from June 1991 to June 1993 for 1 μm, 5.1 μm and 12.6 μm. Left column at the equator (5°S–5°N) at 40 hPa, right column at 69 hPa. Vertical lines show error bars of measurements when available.

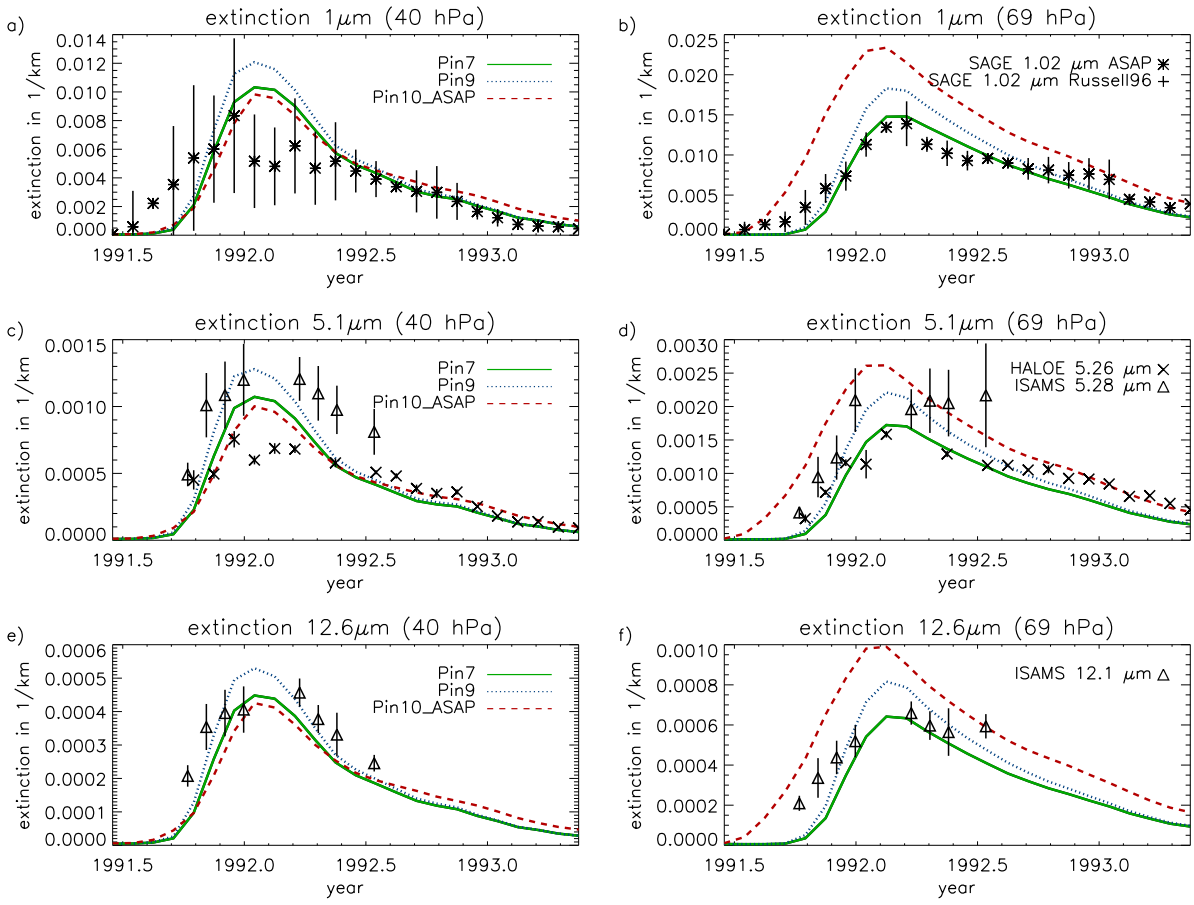

Fig. A.4: Zonal mean extinction from June 1991 to June 1993 for 1 μm, 5.1 μm and 12.6 μm. Left column at mid-latitudes (30°N–40°N) at 40 hPa, right column at 69 hPa. Vertical lines show error bars of measurements when available.

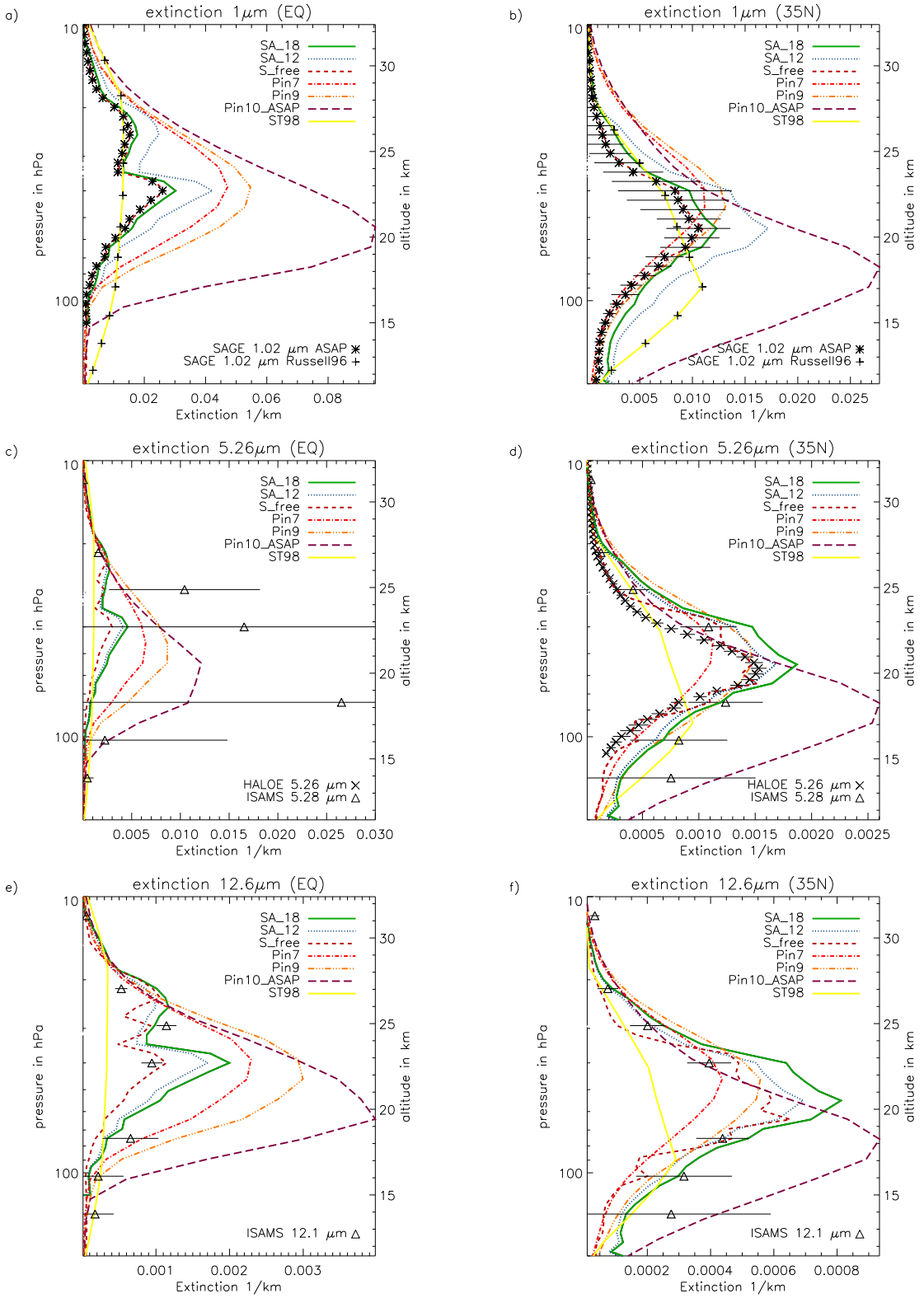

Fig. A.5: Zonal mean extinction profiles in Dec 1991 at 1 μm, 5.26 μm and 12.6 μm. Left column at the equator (5°S-5°N) and right column at northern midlatitudes (30-40°N). Horizontal lines show error bars of measurements.

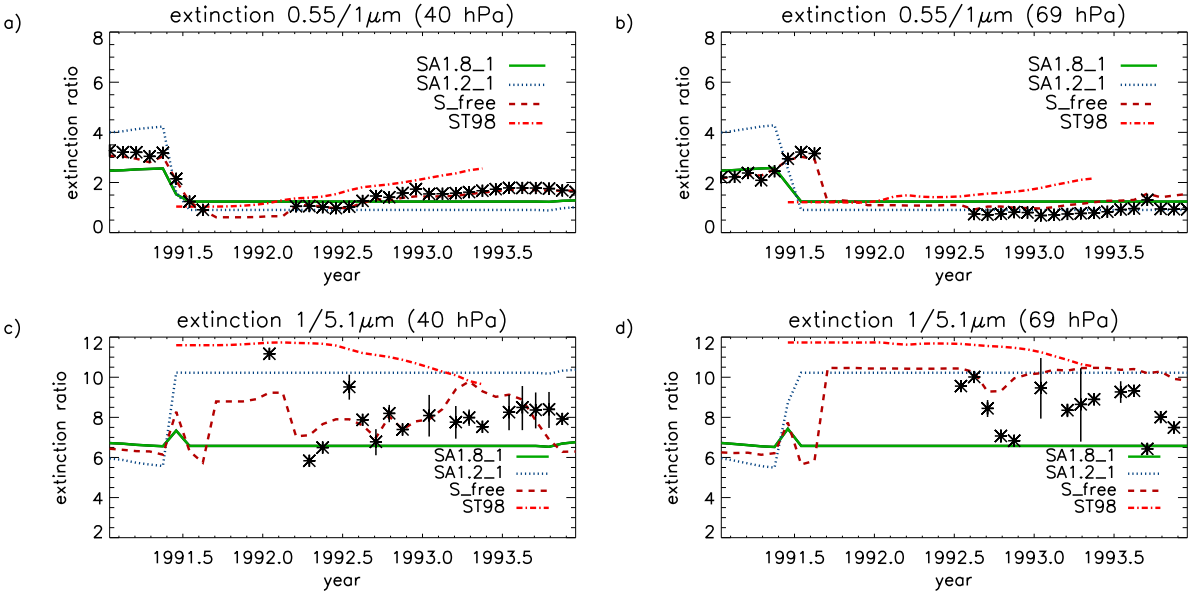

Fig. A.6: Extinction ratio of 0.55 μm/1 μm (a,b) and 1 μm/5.1 μm (c,d). At the equator at 40 hPa altitude (a,c) and at 69 hPa altitude (b,d). Asteriks in (a,b) show ratio of SAGE II 0.55 μm/1 μm (*SPARC*, 2006) and asteriks in (c,d) show ratio of SAGE II 1 μm and HALOE 5.1 μm.

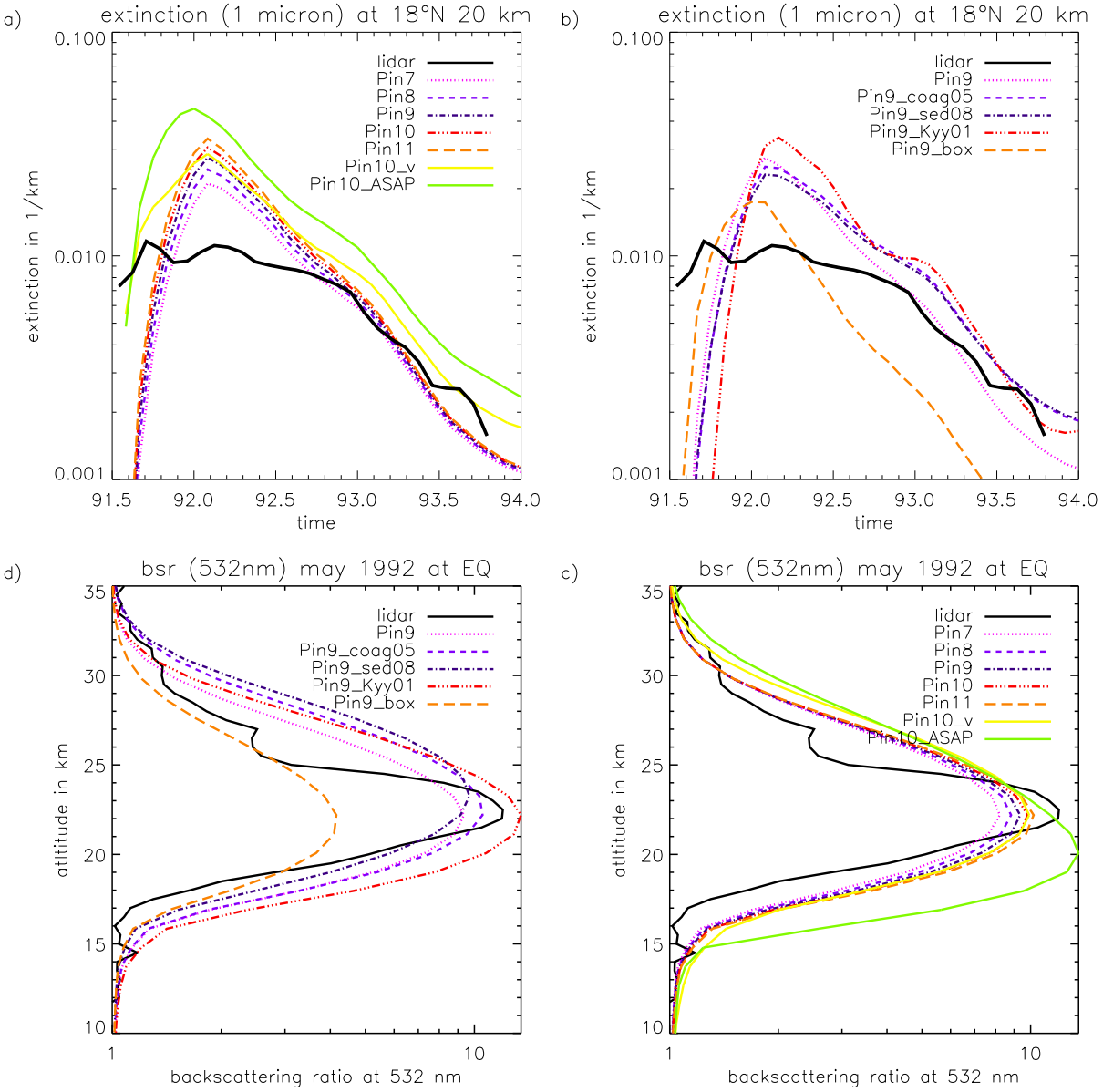

Fig. A.7: (a,b) Extinction at 1 μm from June 1991 to end of 1993 around 20°N measurement composite of lidar in Mauna Loa and Camaguey and derived from AER scenarios and (c,d) backscattering ratio at 532 nm in May 1992 measured by lidar on an airplane and calculated with Mie theory from AER scenarios.

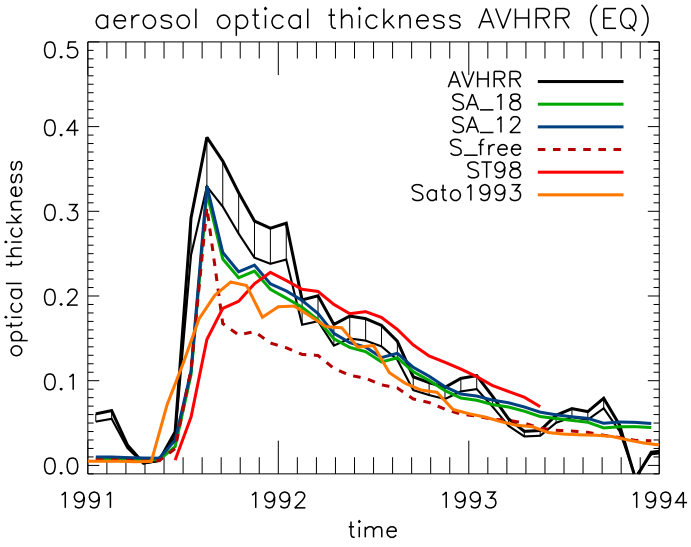

Fig. A.8: Zonal mean stratospheric optical thickness in VIS (550 nm) from January 1991 to December 1993 at the equator (5°S–5°N). Black solid line is a composite of total optical thickness measured by channel 1 (0.58-0.68 μm) and channel 2 (0.724-1.10 μm) of AVHRR, reduced by the tropospheric extinction (average from 1995 to 2000).

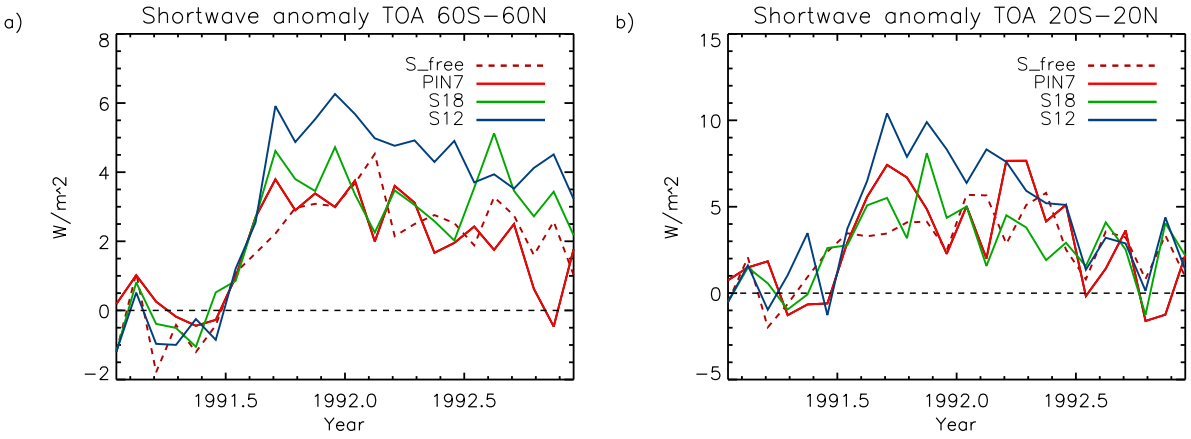

Fig. A.9: Anomalies in net shortwave fluxes at the top-of-the-atmosphere at the equator (20°S–20°N). Anomalies are computed with respect to a control simulation.

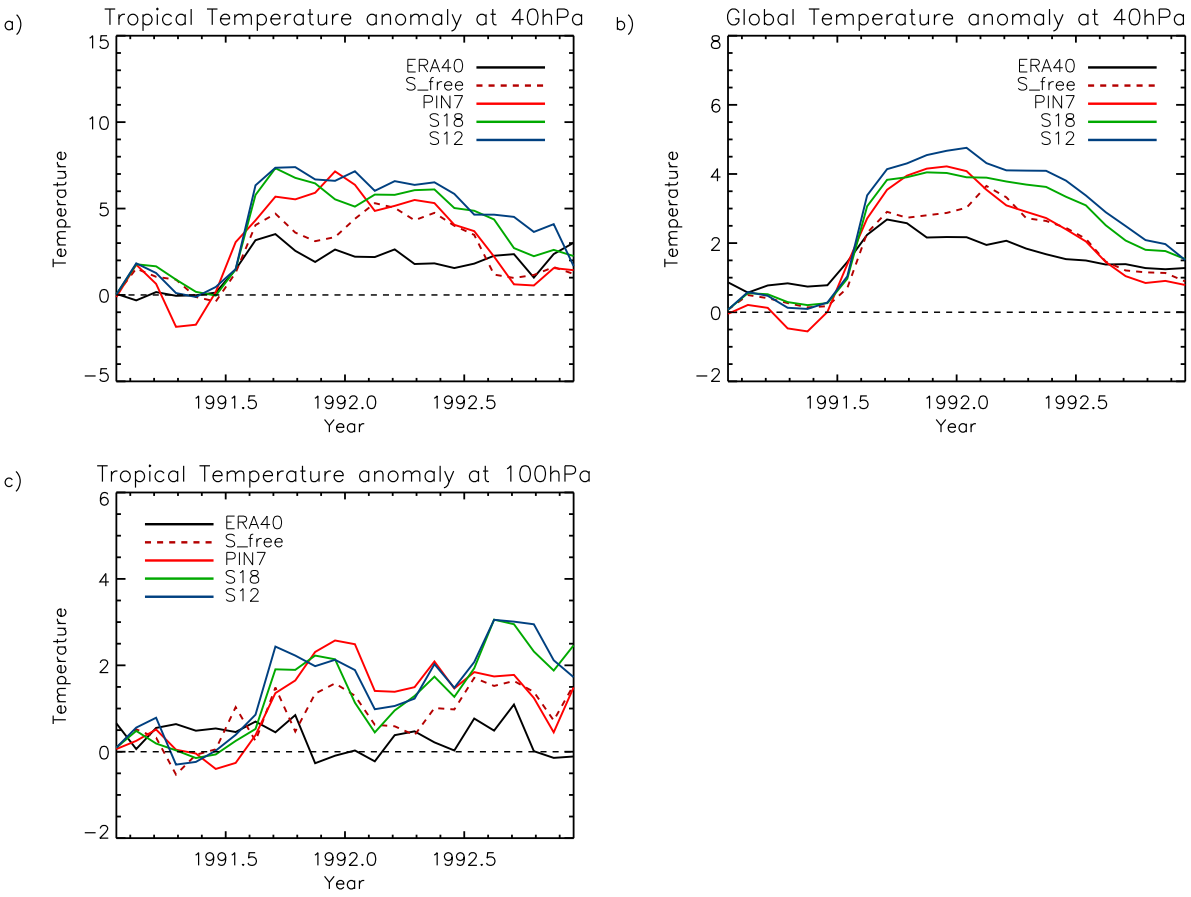

Fig. A.10: Zonal mean temperature anomalies for tropics (20°S–20°N) at 40 hPa (a) and 100hPa (c) as well as global mean anomalies at 40 hPa (b). Scenarios anomalies are wit respect to a control simulation. Black line is ERA40 temperature data anomalies with respect to 1995-1999.

Literature

Ammann, C. M., and P. Naveau (2010), A statistical volcanic forcing scenario generator for climate simulations, *Journal of Geophysical Research*, *115*, D05,107, doi:10.1029/2009JD012550.

Ammann, C. M., G. A. Meehl, W. M. Washington, and C. S. Zender (2003), A monthly and latitudinally varying volcanic forcing dataset in simulations of 20th century climate, *Geophys. Res. Lett*, *30(12)*, 1657, doi:10.1029/2003GL016875.

Antuña, J. C., A. Robock, G. L. Stenchikov, L. W. Thomason, and J. E. Barnes (2002), Lidar validation of SAGE II aerosol measurements after the 1991 Mount Pinatubo eruption, *107*(D14), 4194.

Antuna, J. C., A. Robock, G. Stenchikov, J. Zhou, C. David, J. Barnes, and L. Thomason (2003), Spatial and temporal variability of the stratospheric aerosol cloud produced by the 1991 Mount Pinatubo eruption, *108*(D20), 4624, doi: {10.1029/2003JD003722}.

Auchmann,R., Broennimann, S., Breda, L., Buehler,M., Spadin,R., and A. Stickler (2011), The summer of 1816 in geneva, switzerland, *Clim.Past. Discussions*, *7*, 3745–3774.

Austin, J., and J. Wilson (2006), Ensemble simulations of the decline and recovery of stratospheric ozone, *J. Geophys. Res.*, *111*, D16,314.

Baker, L. L., and M. J. Rutherford (1996), Sulfur diffusion in rhyolite melts, *Contributions to Mineralogy and Petrology*, *123*, 335–344.

Bender et al., (2010), Response to the eruption of mount pinatubo in relation to climate sensitivity in the cmip3 models, *Clim. Dynam.*, *35*, 875–886, doi:,10.1007/s00382-010-0777-3.

Biermann, U. M., B. P. Luo, and T. Peter (2000), Absorption spectra and optical constants of binary and ternary solutions of H_2SO_4, HNO_3, and H_2O in the mid infrared at atmospheric temperatures, *J. Phys. Chem. A*, *104*(4), 783–793.

Bingen, C., D. Fussen, and F. Vanhellemont (2004a), A global climatology of stratospheric aerosol size distribution parameters derived from SAGE II data over the period 1984-2000: 1. Methodology and climatological observations, *109*(D6).

Bingen, C., D. Fussen, and F. Vanhellemont (2004b), A global climatology of stratospheric aerosol size distribution parameters derived from SAGE II data over the period 1984-2000: 2. Reference data, *109*(D6).

Bluth, G. J. S., S. D. Doiron, C. C. Schnetzler, A. J. Krueger, and L. S. Walter (1992), Global tracking of the SO_2 clouds from the June, 1991 Mount-Pinatubo eruptions, *Geophys. Res. Lett.*, *19*(2), 151–154.

Boer, S. M. H. K., GJ (2007), Inferring climate sensitivity from volcanic events., *Clim Dyn*, *28(5)*, 481–502.

Briffa, K., and P. D. Jones (1992), The climate of europe during the 1810s with special reference to 1816, in: The year without a summer?: world climate in 1816, *Canadian Museum of Nature*, pp. 372–391.

Calvert, J., and W. Stockwell (1983), Acid generation in the troposphere by gas phase chemistry, *Environ. Sci. Technol*, *17*, 428A.

Carn, et. al. (2009), Tracking volcanic sulfur dioxide clouds for aviation hazard mitigation, *Natural Hazards*, *51(2)*, 325–343.

Charney, J., and P. Drazin (1961), Propagation of planetary-scale disturbances from the lower into the upper atmosphere, *J.Geophys.Res*, *66*, 83–109.

Chu, W. P., and M. P. McCormick (1979), Inversion of stratospheric aerosol and gaseous constituents from spacecraft solar extinction data in the 0.38-1.0 micron wavelength region., *Appl. Opt.*, *18*, 1404–1414.

Cole-Dai, J., D. Ferris, a. S. J. Lanciki, A., M. Baroni, and M. Thiemens (2009), Cold decade (ad 1810-1819) caused by tambora (1815) and another (1809) stratospheric volcanic eruption, *Geophysical Research Letters*, *36*, L22,703, doi: 10.1029/2009GL040882.

Crowley, et al., (2003), Modeling ocean heat content changes during the last millennium, *Geophys. Res. Lett.*, *30(18)*, 1932, doi:doi:10.1029/2003GL017801.

Crowley, et al., (2008), Volcanism and the little ice age, *PAGES Newslett.*, pp. 22–23.

Crutzen, P. J. (2006), Albedo enhancement by stratospheric sulfur injections: A contribution to resolve a policy dilemma?, *77*(3-4), 211–219.

Curtius et al., (2005), Observations of meteoritic material and implications for aerosol nucleation in the winter Arctic lower stratosphere derived from in situ particle measurements, *Atmos. Chem. Phys.*, *5*, 3053-3069.

Dameris, M., V. Grewe, M. Ponater, R. Deckert, V. Eyring, F. Mager, S. Matthes, C. Schnadt, A. Stenke, B. Steil, C. Brhl, and M. A. Giorgetta (2005), Long-term changes and variability in a transient simulation with a chemistry-climate model employing realistic forcing, *5*, 2121–2145.

Deshler, et al., (2003), Thirty years of in situ stratospheric size distribution measurements from laramie, wyoming (41n), using balloon-borne instruments, *J. Geophys. Res*, *108*, 4167, doi:10.1029/2002JD002514.

Deshler, T., D. J. Hoffman, B. J. Johnson, and W. Rozier (1992), Balloon-borne measurements of the Pinatubo aerosol size-distribution and volatitily at Laramie, Wyoming, during summer of 1991, *Geophys. Res. Lett.*, *19*, 199–202.

Devine, J.D., H. S., A. N. Davis, and S.Self (1984), Estimates of sulfur and chlorine yield to the atmosphere from volcanic eruptions and potential climatic effects, *Journal of Geophysical Research*, *89, NO. B7*, 6309–6325.

Egorova, T. A., E. V. Rozanov, M. E. Schlesinger, N. G. Andronova, S. L. Malyshev, I. L. Karol, and V. A.Zubov (2001), Assessment of the effect of the Montreal Protocol on atmospheric ozone, *Geophys. Res. Lett.*, *28*, 2389–2392.

Egorova, T. A., E. V. Rozanov, V. A. Zubov, and I. L. Karol (2003), Model for investigating ozone trends (MEZON), *39 (3)*, 277–292.

Egorova, T. A., E. V. Rozanov, V. A. Zubov, E. Manzini, W. Schmutz, and T. Peter (2005), Chemistry-Climate Model SOCOL: a validation present-day climatology, *5*, 1557–1576.

Eyring, V., N. Butchart, D. W. Waugh, H. Akiyoshi, J. Austin, S. Bekki, G. E. Bodeker, B. A. Boville, C. Bruhl, M. P. Chipperfield, E. Cordero, M. Dameris, M. Deushi, V. E. Fioletov, S. M. Frith, R. R. Garcia, A. Gettelman, M. A. Giorgetta, V. Grewe, L. Jourdain, D. E. Kinnison, E. Mancini, E. Manzini, M. Marchand, D. R. Marsh, T. Nagashima, P. A. Newman, J. E. Nielsen, S. Pawson, G. Pitari, D. A. Plummer, E. Rozanov, M. Schraner, T. G. Shepherd, K. Shibata, R. S. Stolarski, H. Struthers, W. Tian, and M. Yoshiki (2006), Assessment of temperature, trace species, and ozone in chemistry-climate model simulations of the recent past, *111*, D22,308.

Eyring, V., T. G. Shepherd, and D. W. W. (Eds.) (2010), Sparc ccmval (2010), sparc report on the evaluation of chemistry-climate models, *Tech. rep.*, SPARC Report No. 5, WCRP-132, WMO/TD-No. 1526.

Fero, et al., (2009), Simulating the dispersal of tephra from the 1991 pinatubo eruption: Implications for the formation of widespread ash layers, *Journal of Volcanology and Geothermal Research*, *186*, 120–131.

Fleming, E., C. Jackman, R. Stolarski, and D. Considine (1999), Simulation of stratospheric tracers using an improved empirically based two-dimensional model transport formulation, *104* (D19), 23,911–23,934.

Forster, et al.,(2007), Changes in Atmospheric Constituents and in Radiative Forcing. In: Climate Change 2007: The Physical Science Basis. Contribution of Working Group I to the Fourth Assessment Report of the Intergovernmental Panel on Climate Change, *Cambridge University Press, Cambridge, United Kingdom and New York, NY, USA.*

Fouquart, Y., and B. Bonnel (1980), Computations of solar heating of the earth's atmosphere: A new parameterization, *Contrib. Atmos. Phys*, *53*, 35–62.

Franklin, B. (1784), Meteorological imaginations and conjectures, *Mem. Lit. Philos. Soc. Manchester*, *2*, 373–377.

Gao, C. (2008), Volcanic forcing of climate over the past 1500 years: An improved ice-core-based index for climate models, Ph.D. thesis, Graduate School - New Brunswick. Rutgers, the State University of New Jersey.

Gao, C., A. Robock, and C. Ammann (2008), Volcanic forcing of climate over the past 1500 years: An improved ice core-based index for climate models, *J. Geophys. Res*, *113*, D23,111, doi:10.1029/2008JD010239.

Gao, C. H., L. Oman, A. Robock, and G. L. Stenchikov (2007), Atmospheric volcanic loading derived from bipolar ice cores: Accounting for the spatial distribution of volcanic deposition, *112*(D9).

Geogdzhayev, I. V., M. I. Mishchenko, L. Liu, and L. Remer (2004), Global two-channel AVHRR aerosol climatology: effects of stratospheric aerosols and preliminary comparisons with MODIS and MISR retrievals, *Journal of Quantitative Spectroscopy & Radiative Transfer*, *88*(1-3), 47–59.

Gettelman, et al., (2010), Multimodel assessment of the upper troposphere and lower stratosphere: Tropics and global trends, *Journal of Geophysical Research*, *D00M08*, 115, doi:10.1029/2009JD013638.

Gleckler, P. J., K. AchutaRao, J. M. Gregory, B. D. Santer, K. E. Taylor, and T. M. L. Wigley (2006), Krakatoa lives: The effect of volcanic eruptions on ocean heat content and thermal expansion, *Geophys. Res. Lett.*, *33*(17), L17,702.

Goosse, et al., (2005), Internal and forced climate variability during the last millennium: a model-data comparison using ensemble simulations, *Quat. Sci. Rev.*, *24*, 1345?1360.

Grainger, R. G., A. Lambert, F. W. Taylor, J. J. Remedios, C. D. Rodgers, M. Corney, and B. J. Kerridge (1993), Infrared-absorption by volcanic stratospheric aerosols observed by ISAMS, *Geophys. Res. Lett.*, *20*(12), 1283–1286.

Grainger, R. G., A. Lambert, C. D. Rodgers, F. W. Taylor, and T. Deshler (1995), Stratospheric aerosol effective radius, surface-area and volume estimated from infrared measurements, *100*(D8), 16,507–16,518.

Gregory, J. M. (2010), Long-term effect of volcanic forcing on ocean heat content, *Geophys.Res. Lett.*, p. 22701, doi:10.1029/2010GL045507.

Guo, S., G. J. S. Bluth, W. I. Rose, I. M. Watson, and A. J. Prata (2004), Re-evaluation of SO_2 release of the 15 June 1991 Pinatubo eruption using ultraviolet and infrared satellite sensors, *5*(4), Q04,001.

Hamill, P., E. J. Jensen, P. B. Russell, and J. J. Bauman (1997), The life cycle of stratospheric aerosol, *Bull. Amer. Meteorol. Soc.*, *78*, 1395–1410.

Haywood, et al., J.M (2010), Observations of the eruption of the sarychev volcano and simulations using the hadgem2 climate model, *J. Geophys. Res.*, *115*, D21,212, doi:10.1029/2010JD014447.

Heald, et al., (1963), The chemistry of volcanic gases, 2, use of equilibrium calculations in the interpretation of volcanic gas samples, *J. Geophys. Res.*, *68*, 545–557.

Heckendorn, et al., (2009), The impact of geoengineering aerosols on stratospheric temperature and ozone, *Environ. Res. Lett*, *4*, 045,108 (12pp), doi: 10.1088/1748-9326/4/4/045108.

Hegerl, G., J. Luterbacher, F. Gonzalez-Rouco, S. B. Tett, T. Crowley, and E. Xoplaki (2011), Influence of human and natural forcing on european seasonal temperatures, *Nature Geoscience*, *4*, 99–103, doi:10.1038/NGEO1057.

Hegerl, et al., (2003), Detection of volcanic, solar and greenhouse gas signals in paleo-reconstructions of northern hemispheric temperature, *Geophys. Res. Lett.*, *30(5)*, 1242, doi:doi:10.1029/2002GL016635.

Hervig, M. E., J. M. Russell, L. L. Gordley, J. Daniels, S. R. Drayson, and J. H. Park (1995), Aerosol effects and corrections in the Halogen Occultation Experiment, *100*(D1), 1067–1079.

Herzog, M., and H. Graf (2010), Applying the three-dimensional model atham to volcanic plumes: Dynamic of large co-ignimbrite eruptions and associated injection heights for volcanic gases, *Geophys. Res. Lett*, *37*, 19,807.

Highwood, E., and D. Stevenson (2003), Atmospheric impact of the 1783-1784 laki eruption: Part ii climatic effect of sulphate aerosol, *Atmospheric Chemistry and Physics*, *3*, 1599–1629.

Hoffman, D. J., and J. M. Rosen (1983), Stratospheric sulfuric acid fraction and mass estimate for the 1982 volcanic eruption of El Chinchón, *Geophys. Res. Lett.*, *10*, 313–316.

Holton, J. R., P. H. Haynes, M. E. McIntyre, A. R. Douglass, R. B. Rood, and L. Pfister (1995), Stratosphere-troposphere exchange, *33*(403-440).

Joseph, R., and N. Zeng (2011), Seasonally modulated tropical drought induced by volcanic aerosol, *24(8)*, 2045–2060.

Joshi, M., and G. Jones (2009), The climatic effects of the direct injection of water vapour into the stratosphere by large volcanic eruptions, *acp*, *9*, 6109–6118.

Jungclaus, J. H., S. J. Lorenz, C. Timmreck, C. H. Reick, V. Brovkin, K. Six, J. Segschneider, M. A. Giorgetta, T. J. Crowley, J. Pongratz, N. A. Krivova, L. E. Vieira, S. K. Solanki, D. Klocke, M. Botzet, M. Esch, V. Gayler, H. Haak, T. J. Raddatz, E. Roeckner, R. Schnur, H. Widmann, M. Claussen, B. Stevens, and J. Marotzke (2010), Climate and carbon-cycle variability over the last millennium, *Climate of the Past*, *6*(5), 723–737, doi:10.5194/cp-6-723-2010.

Kayzar, et al., (2009), Gas transport model for the magmatic system at mount pinatubo, philippines: Insights from (pb-210)/(ra-226)., *Journal of Volcanology and Geothermal Research*, *181*, 124–140.

Kenzelmann, P. (2009), Global warming by increased methane release and global cooling by stratospheric sulphur injections - Consequences for the stratosphere, *Dissertation No. 18241, ETH Zurich, Switzerland*.

Kinnison, D. E., K. E. Grant, P. S. Connell, D. A. Rotman, and D. J. Wuebbles (1994), The chemical and radiative effects of the Mount-Pinatubo eruption, *99*(D12), 25,705–25,731.

Koyagushi, M., T. & Tokuno (1993), Origin of the giant eruption cloud of pinatubo, june 15, 1991, *Journal of Volcanology and Geothermal Research*, *55*, 85–96.

Kravitz, et al., B. (2011), The geoengineering model intercomparison project (geomip), *Atmospheric Science Letters*, *12(2)*, 162–167.

Labitzke, K., and M. P. McCormick (1992), Stratospheric temperature increases due to Pinatubo aerosols, *Geophys. Res. Lett.*, *19*(2), 207–210.

Lamb, H. (1970), Volcanic dust in the atmosphere, with a chronology and assessment of its meteorological significance., *Philosophical Transactions of the Royal Society London Series A*, *266*, 425–533.

Lambert, A., R. G. Grainger, J. J. Remedios, C. D. Rodgers, M. Corney, and F. W. Taylor (1993), Measurements of the evolution of the Mt-Pinatubo aerosol cloud by ISAMS, *Geophys. Res. Lett.*, *20*(12), 1287–1290.

Lambert, A., R. G. Grainger, C. D. Rodgers, F. W. Taylor, J. L. Mergenthaler, J. B. Kumer, and S. T. Massie (1997), Global evolution of the Mt Pinatubo volcanic aerosols observed by the infrared limb-sounding instruments CLAES and ISAMS on the Upper Atmosphere Research Satellite, *102*(D1), 1495–1512.

Lanzante, J. R., and M. Free (2007), Comparison of radiosonde and gcm vertical temperature trend profiles: Effects of dataset choice and data homogenization.

Manzini, E., and N. A. McFarlane (1998), The effect of varying the source spectrum of a gravity wave parameterization in the middle atmosphere general circulation model, *103*(D24), 31,523–31,539.

Mastin, L. et al. (2009), A multidisciplinary effort to assign realistic source parameters to models of volcanic ash-cloud transport and dispersion during eruptions, *Journal of Volcanology and Geothermal Research*, doi:10.1016/j.jvolgeores.2009.01.008.

Mastin, L. G. (2007), A user-friendly one-dimensional model for wet volcanic plumes, *Geochem. Geophys. Geosyst*, *8*, Q03,014, doi:10.1029/2006GC001455.[AGU].

McCormick, M. P. (1992), Initial assessment of the stratospheric and climatic impact of the 1991 Mount-Pinatubo eruption - prologue, *Geophys. Res. Lett.*, *19*(2), 149–149.

Mann, et al., (2009), Global signatures and dynamical origins of the little ice age and medieval climate anomaly, *Science*, *Vol. 326. no. 5957*, 1256 – 1260, doi: 10.1126/science.1177303.

Mie, G. (1908), Articles on the optical characteristics of turbid tubes, especially colloidal metal solutions, *Annalen der Physik*, *25*(3), 377–445.

Milham, W. (1924), The year 1816: the cause of abnormalities., *Monthly Weather Review*, *52*, 563–79.

Minnis, P., E. F. Harrison, L. L. Stowe, G. G. Gibson, F. M. Denn, D. R. Doelling, and W. L. Smith (1993), Radiative climate forcing by the Mount-Pinatubo eruption, *259*(5100), 1411–1415.

Mitchell, J., J.M. (1970), A preliminary evaluation of atmospheric pollution as a cause of the global temperature fluctuation of the past century, *Global Effects of Environmental Pollution*, pp. 145–155.

Morcrette, J. J. (1991), Radiation and cloud radiative properties in the European Center for Medium-Range Weather Forecasts forecasting system, *J. Geophys. Res.*, *96*(D5), 9121–9132.

Morgenstern, et al., (2010), Review of the formulation of present?generation stratospheric chemistry?climate models and associated external forcings, *J. Geophys. Res.*, *115*, D00M02, doi:10.1029/2009JD013728.

Newhall, et al., (1996), Fire and mud: Eruptions and lahars on mount pinatubo, philippines. quezon city, *University of Washington Press, Seattle and London*.

Oppenheimer, C. (2003), Climatic, environmental and human consequences of the largest known historic eruption: Tambora volcano (Indonesia) 1815, *Progress in Physical Geography*, *27*(2), 230–259.

Pallister, et al.,. (1992), A basalt trigger for the 1991 eruptions of pinatubo volcano, *Nature*, *356*, 426–428.

Pinto, J. P., R. P. Turco, and O. B. Toon (1989), Self?limiting physical and chemical effects in volcanic eruption clouds, *J. Geophys. Res.*, *94(D8)*, 11,165–11,174.

Plumb, R. A. (1996), A tropical pipe model of stratospheric transport., *J. Geophys. Res.*, *101*, 3957–3972.

Rasch, P. J., P. J. Crutzen, and D. B. Coleman (2008), Exploring the geoengineering of climate using stratospheric sulfate aerosols: The role of particle size, *Geophys. Res. Lett.*, *35*(2), L02,809.

Robock, A. (2010), New start, eyjafjallajkull, and nuclear winter, *Eos*, *91 (47)*, 444–445, doi:10.1029/2010ES003201.

Robock, A., and J. C. Antuna (2001), Support for a tropical lidar in latin america, *Eos Trans. AGU*, *82(26)*, 285, doi:10.1029/EO082i026p00285-03.

Robock, A., and Y. Liu (1994), The volcanic signal in goddard institute for space studies three-dimensional model simulations, *J. Climate*, *7*, 44–55.

Robock, A., and J. Mao (1992), Winter warming from large volcanic eruptions, *Geophys. Res. Lett.*, *19*, 2405–2408.

Roche, A. E., J. B. Kumer, J. L. Mergenthaler, G. A. Ely, W. G. Uplinger, J. F. Potter, T. C. James, and L. W. Sterritt (1993), The Cryogenic Limb Array Etalon Spectrometer (CLAES) on UARS - experiment description and performance, *98*(D6), 10,763–10,775.

Rosen, J. M. (1964), The vertical distribution of dust to 30 km., *J. Geophys. Res.*, *69*, 4673–4676.

Rosenlof, K. (1995), Seasonal cycle of the residual mean meridional circulation in the stratosphere, *Journal of Geophysical Research*, *100(D3)*.

Rozanov, E., M. E. Schlesinger, V. Zubov, F. Yang, and N. G. Andronova (1999), The UIUC three-dimensional stratospheric chemical transport model: Description and evaluation of the simulated source gases and ozone, *J. Geophys. Res.*, *104*, 11,755–11,781.

Rozanov, E., E. M. Schlesinger, and V. A. Zubov (2001), The University of Illinois, Urbana- Champaign three-dimensional stratosphere-troposphere general circulation model with interactive ozone photochemistry: Fifteen-year control run climatology, *J. Geophys. Res.*, *106*, 27,233–27,254.

Russell, J. M., L. L. Gordley, J. H. Park, S. R. Drayson, W. D. Hesketh, R. J. Cicerone, A. F. Tuck, J. E. Frederick, J. E. Harries, and P. J. Crutzen (1993), The Halogen Occultation Experiment, *98*(D6), 10,777–10,797.

Russell, P. B., J. M. Livingston, R. F. Pueschel, J. J. Bauman, J. B. Pollack, S. L. Brooks, P. Hamill, L. W. Thomason, L. L. Stowe, T. Deshler, E. G. Dutton, and R. W. Bergstrom (1996), Global to microscale evolution of the Pinatubo volcanic aerosol derived from diverse measurements and analyses, *101*(D13), 18,745–18,763.

Sander, S. P., R. R. Friedl, W. B. DeMore, D. M. Golden, M. J. Kurylo, R. F. Hampson, R. E. Huie, G. K. Moortgat, A. R. Ravishankara, C. E. Kolb, and M. J. Molina (2000), Chemical kinetics and photochemical data for use in stratospheric data, supplement to evaluation 12: Update of key reactions, *JPL Publication 00-3*.

Sato, M., J. E. Hansen, M. P. McCormick, and J. B. Pollack (1993), Stratospheric aerosol optical depths, 1850-1990, *98*(D12), 22,987–22,994.

Schmidt, G. A., J. H. Jungclaus, C. M. Ammann, E. Bard, P. Braconnot, T. J. Crowley, G. Delaygue, F. Joos, N. A. Krivova, R. . Muscheler, B. L. Otto-Bliesner, J. Pongratz, D. T. Shindell, S. K. Solanki, F. Steinhilber, and L. E. A. Vieira (2011), Climate forcing reconstructions for use in pmip simulations of the last millennium (v1.0), *Geosci.Model Dev.*, *4*, 33–45.

Schraner, M., E. Rozanov, C. Schnadt Poberaj, P. Kenzelmann, A. Fischer, V. Zubov, B. Luo, C. Hoyle, T. Egorova, S. Fueglistaler, S. Brönnimann, W. Schmutz, and T. Peter (2008), Technical note: Chemistry-climate model SOCOL: version 2.0 with improved transport and chemistry/microphysics schemes, *8*, 5957–5974.

Self, S., and A. J. King (1996), Petrology and sulfur and chlorine emissions of the 1963 eruption of gunung agung, bali, indonesia, *Bulletin of Volcanology*, *58*, 263–285.

Self, S., and M. R. Rampino (1981), The 1883 eruption of krakatau, *Nature*, *294*, 699–704.

Self, S., R. Gertisser, T. Thordarson, M. R. Rampino, and J. A. Wolff (2004) Magma volume, volatile emissions, and stratospheric aerosols from the 1815 eruption of Tambora, *Geophysical Research Letters*, *31*, L20,608, doi:10.1029/2004GL020925.

Self S, C. M., Rampino MR (1989), A reappraisal of the 1835 eruption of Cosiguina and its atmospheric impact., *Bull Volcanol*, *52*, 57–65.

Shindell, D. T., G. A. Schmidt, M. E. Mann, and G. Faluvegi (2004), Dynamic winter climate response to large tropical volcanic eruptions since 1600, *Journal of Geophysical Research*, *109*, D05,104, doi:10.1029/2003JD004151.

Sigurdsson, et al., (1984), The 1982 eruptions of El Chichon volcano, Mexico: Stratigraphy of pyroclastic deposits, *Journal of Volcanology and Geothermal Research*, *23*, 11–37.

Sigurdsson, H., and S. Carey (1989), Plinian and co-ignimbrite tephra fall from the 1815 eruption of tambora volcano, *Bull Volcanol*, *51*, 243–270.

Solomon, et al., (2010), Contributions of stratospheric water vapor to decadal changes in the rate of global warming, *Science*, *327(5970)*, 1219–23.

Solomon, S. (1999), Stratospheric ozone depletion: A review of concepts and history, *37*(3), 275–316.

Solomon, S., et al., (2011), The persistently variable background stratospheric aerosol layer and global climate change, *Science*, *333*, 866–870, doi:10.1126/science.1206027.

SPARC (2006), SPARC Assessment of Stratospheric Aerosol Properties, L. Thomason and T. Peter (eds.), , *SPARC Report No. 4, World Climate Research Programme WCRP- 124, WMO/TD No. 1295*.

Steele, H. M., and P. Hamill (1983), Effects of temperature and humidity on the growth and optical properties of sulphuric acid-water droplets in the stratosphere, *J. Atmos. Sci.*, *12*, 517–528.

Stenchikov, G., K. Hamilton, R. J. Stouffer, A. Robock, V. Ramaswamy, B. Santer, and H. F. Graf (2006), Arctic oscillation response to volcanic eruptions in the IPCC AR4 climate models, *111*(D7), D07,107.

Stenchikov, G., T. L. Delworth, V. Ramaswamy, R. J. Stouffer, A. Wittenberg, and F. Zeng (2009), Volcanic signals in oceans, *J. Geophys. Res.*, *114*, D16,104, doi:doi:10.1029/2008JD011673.

Stenchikov, G. L., I. Kirchner, A. Robock, H. F. Graf, J. C. Antuna, R. G. Grainger, A. Lambert, and L. Thomason (1998), Radiative forcing from the 1991 Mount Pinatubo volcanic eruption, *103*(D12), 13,837–13,857.

Stendel, I. M. Mogensen, and J. Christensen (2006), Influence of various forcings on global climate in historical times using a coupled atmosphere ocean general circulation model, *Climate Dynamics*, *26*, 1–15 1–15, doi:DOI10.1007/s00382-005-0041-4.

Stix, K., and t. Kobayashi (2008), Magma dynamics and collapse mechanisms during four historic caldera-forming events, *Journal of Geophysical Research-Solid Earth*, *113*.

Stothers, R. (2001), A chronology of annual mean effective radii of stratospheric aerosols from volcanic eruptions during the twentieth century as derived from ground-based spectral extinction measurements, *J. Geophys. Res.*, *106*, 32,043–32,049.

Stothers, R. B. (1984), The great tambora eruption in 1815 and its aftermath, *Science*, *224*.

Stothers, R. B. (1996), Major optical depth perturbations to the stratosphere from volcanic eruptions : Pyrheliometric period, 1881-1960, *J.Geophys.Res*, *101*, 3901–3920.

Stothers, R. B. (2007), Three centuries of observation of stratospheric transparency, *Climatic Change*, *83*, 515–521.

Stowe, L. L., R. M. Carey, and P. P. Pellegrino (1992), Monitoring the Mt-Pinatubo aerosol layer with NOAA-11 AVHRR data, *Geophys. Res. Lett.*, *19*(2), 159–162.

Druitt, et al., (2012), Decadal to monthly timescales of magma transfer and reservoir growth at a caldera volcano, *Nature*, *482*, 77–80, doi:10.1038/nature10706.

Taylor, F. W., C. D. Rodgers, J. G. Whitney, S. T. Werrett, J. J. Barnett, G. D. Peskett, P. Venters, J. Ballard, C. W. P. Palmer, R. J. Knight, P. Morris, T. Nightingale, and A. Dudhia (1993), Remote-sensing of atmospheric structure and composition by pressure modulator radiometry from space - the ISAMS experiment on UARS, *98*(D6), 10,799–10,814.

Tett, et. al., S.F.B. (2007), The impact of natural and anthropogenic forcings on climate and hydrology since 1550, *Clim. Dyn.*, *28(1)*, 334.

Textor, C., M. H., H. Graf, and J. M. Oberhuber (2003), Injection of gases into the stratosphere by explosive volcanic eruptions, *Journal of Geophysical Research*, *108 D19*, 4606, doi:10.1029/2002JD002987.

Thomason, L., J. M. Zawodny, S. P. Burton, and N. Iyer (2001), The SAGE II algorithm: Version 6.0 and on-going developments, *8th Scientific Assembly of International Association of Meteorology and Atmospheric Sciences, Innsbruck Austria*, *July 10-18*.

Thomason, L. W. (1991), A diagnostic stratospheric aerosol size distribution inferred from SAGE-II measurements, *96*(D12), 22,501–22,508.

Thomason, L. W. (1992), Observations of a new SAGE-II aerosol extinction mode following the eruption of Mt-Pinatubo, *Geophys. Res. Lett.*, *19*(21), 2179–2182.

Thomason, L. W., G. S. Kent, C. R. Trepte, and L. R. Poole (1997a), A comparison of the stratospheric aerosol background periods of 1979 and 1989-1991, *102*(D3), 3611–3616.

Thomason, L. W., L. R. Poole, and T. Deshler (1997b), A global climatology of stratospheric aerosol surface area density deduced from Stratospheric Aerosol and Gas Experiment II measurements: 1984-1994, *102*(D7), 8967–8976.

Thouret, D. J. E. J., J.C (1999), Largest explosive eruption in historical times in the andes at huaynaputina volcano , a.d. 1600, southern peru., *Geology*, *27*, 435–438.

Tie, X., and G. Brasseur (1995), The response of stratospheric ozone to volcanic eruptions: Sensitivity to atmospheric chlorine loading, *Geophys. Res. Lett*, *22*, 3035–3038.

Timmreck, et al., (2009), Limited temperature response to the very large ad 1258 volcanic eruption, *Geophysical Research Letters*, *36*, L21,708, doi:10.1029/2009GL040083.

Toohey, et al., (2011), The influence of eruption season on the global aerosol evolution and radiative impact of tropical volcanic eruptions, *Atmos. Chem. Phys.*, *11*, 12,351–12,367.

Toon, et al., (2007), Consequences of regional-scale nuclear conflicts, *Science*, *315*, 1224–1225, doi:10.1126/science.1137747.

Trigo,et al., (2009), Iberia in 1816, the year without a summer, *Int. J. Climatol.*, *29*, 99–115.

Turco, R. P., R. C. Whitten, and O. B. Toon (1982), Stratospheric aerosols - observation and theory, *20*(2), 233–279.

Vernier, J., L. W. Thomason, J. Pommereau, A. Bourassa, J. Pelon, A. Garnier, A. Hauchecorne, L. Blanot, C. Trepte, D. Degenstein, and V. F. (2011), Major influence of tropical volcanic eruptions on the stratospheric aerosol layer during the last decade, *Geophysical Research Letters*, *38*, L12,807, doi:10.1029/2011GL047563.

Vupputuri, R. K. R. (1992), The Tambora eruption in 1815 provides a test on possible global climatic and chemical perturbations in the past, *Natural Hazards*, *5*, 1–16.

Weisenstein, et al., (1997), A two-dimensional model of sulfur species and aerosols, *102*(11D), 13,019–13,035.

Weisenstein, D. K., J. E. Penner, M. Herzog, and X. Liu (2007), Global 2-D intercomparison of sectional and modal aerosol modules, *7*(9), 2339–2355.

Wielicki, B. A., T. M. Wong, R. P. Allan, A. Slingo, J. T. Kiehl, B. J. Soden, C. T. Gordon, A. J. Miller, S. K. Yang, D. A. Randall, F. Robertson, J. Susskind, and H. Jacobowitz (2002), Evidence for large decadal variability in the tropical mean radiative energy budget, *295*(5556), 841–844.

Wigley, T. M. L., C. M. Ammann, B. D. Santer, and S. C. B. Raper (2005), Effect of climate sensitivity on the response to volcanic forcing, *J. Geophys. Res*, *110*, D09,107, doi:10.1029/2004JD005557.

Williams, S. N., and S. Self (1983), The october 1902 plinian eruption of santa-maria volcano, guatemala, *.Journal of volcanology and geothermal research*, *16*, 33–56.

Winker, D., and M. Osborn (1992), Airborne lidar observations of the Pinatubo volcanic plume, *Geophys. Res. Lett.*, *19*(2), 167–170.

Wong, et al., (2006), Reexamination of the observed decadal variability of the earth radiation budget using altitude-corrected ERBE/ERBS nonscanner WFOV data, *19*(16), 4028–4040.

Wurl, D., R. G. Grainger, A. J. McDonald, and T. Deshler (2010), Optimal estimation retrieval of aerosol microphysical properties from SAGE II satellite observations in the volcanically unperturbed lower stratosphere, *Atmospheric Chemistry and Physics*, *10*(9), 4295–4317, doi:10.5194/acp-10-4295-2010.

Zielinski, G. (1995), Stratospheric loading and optical depth estimates of explosive volcanism over the last 2100 years derived from the Greenland Ice Sheet Project 2 ice core., *J Geophy Res*, *100*, 20,937–20,955.

curriculum vitæ

Florian Arfeuille

Email florian.arfeuille@env.ethz.ch

Born on the 16^{th} August 1984

Academic background

since 2008 — PhD student at the Institute for Atmospheric and Climate Science,
ETH Zurich.

2002-2008 — Studies in environmental science, University of Versailles /INSTN (CEA):

Major: Atmospheric physics.

Master Thesis: "Evolution of El Nino during the holocene in the IPSL-CM4 model"
Dir: Pascale Braconnot, LSCE/IPSL.

Bachelor Thesis: "Analysis of changes in mean climate and interannual variability in a sequence of late quaternary simulations using the FOAM model"
Dir: Sandy Harrison, BRIDGE/University of Bristol.

Teaching

Supervision of Bachelor Thesis:

Heather Mack : Height of stratospheric sulphur and halogen injection from major volcanic eruptions since 1600 AD. (summer 2009)

Teaching Assistant:

Numerical modeling of weather and climate (February 2011 - May 2011)

Weather systems (September 2010 - December 2010)

Sun photometry (February - May 2009 and 2010)

Presentations

- Modeling the "Year Without Summer 1816" with a Chemistry-Climate Model,EGU General Assembly, Vienna, April 19^{th}-24^{th} 2009.
- Climate impacts from large volcanic eruptions, Volcano workshop zürich July 8^{th}-9^{th} 2009.
- Stratospheric impacts of the Tambora eruption, NCCR summer school, Grindelwald, Switzerland, 2009.
- Modeling the "Year Without Summer 1816" with the CCM SOCOL, EGU General Assembly, Vienna, May 2^{nd}-7^{th} 2010.
- Climate impacts from large tropical eruptions, Extremes workshop, Diessenhofen, Switzerland, June 7^{th}-9^{th} 2010.
- Year without summer 1816: Causes and Consequences, NCCR summer school, Grindelwald, Switzerland, 2010.
- The year without summer 1816, 10th EMS Annual Meeting, 10th European Conference on Applications of Meteorology (ECAM), September 13^{th}-17^{th} 2010.
- Modeling the "Year Without Summer 1816" with the CCM SOCOL, EGU General Assembly, Vienna, April 3^{rd}-8^{th} 2011.
- Modeling of the year without summer 1816 with a chemistry-climate model, IUGG conference, Melbourne, June 28^{th}-July 7^{th} 2011.
- Uncertainties in modeling the stratospheric warming after the Pinatubo eruption, SPARC Workshop Zürich, February 6^{th}-7^{th} 2012.

Acknowledgment

First of all I would like to thank Stefan Brönnimann and Thomas Peter for their support and enthousiasm throughout my thesis. I enjoyed the discussions and highly benefited from their ideas and challenging questions.

I would also like to thank Eugene Rozanov for the SOCOL support and interesting discussions. Many thanks go to Kirstin Krüger for accepting to examine my thesis.

Further thanks go to Debra Weisenstein for the help in running the AER model and here contribution to this thesis, Beiping Luo, who provided his expertise on aerosols optical properties, and Patricia Heckendorn for her contribution in the modeling of the Pinatubo eruption. I am greatly thankful to Larry Thomason, Gera Stenchikov and Claudia Timmreck for interesting discussions at several conferences.

Many thanks go to the SOCOL family, especially Andreas Fischer, Marco Calisto, Jianxiong Sheng, Julien Anet, and my officemate Andrea Stencke. I thank all the institute members for the nice atmosphere at IAC. I thank administrative and computational staff Petra Forney, Eva Choffat, Rahel Buri, Peter Isler and Daniel Lüthi for their support

Further thanks go to my football teammates at the institute and especially our goalkeeper Sebastian Bretl who remained brave in difficult situations. Thanks to Uwe Weers for interesting (late) discussions and for having nice taste in music. Many thanks to Cédric Chou for the fruitful discussions over a beer. Many thanks to Ana Cirisan and André Welti for the nice moments we had in Australia.

Warm thanks to my family and friends who always supported me.